EXPERIMENTAL AND NUMERICAL CHARACTERIZATION OF THE THERMAL AND HYDRAULIC PERFORMANCE OF A CANNED MOTOR PUMP OPERATING WITH TWO-PHASE FLOW

A Dissertation

by

YINTAO WANG

Submitted to the Office of Graduate and Professional Studies of
Texas A&M University
in partial fulfillment of the requirements for the degree of

DOCTOR OF PHILOSOPHY

Chair of Committee,	Adolfo Delgado
Committee Members,	Karen Vierow Kirkland
	Michael Pate
	Je-Chin Han
Head of Department,	Andreas A. Polycarpou

May 2019

Major Subject: Mechanical Engineering

ABSTRACT

Canned motor pump (CMP), as one kind of sealless pump, has been utilized in industry for many years to handle hazards or toxic product and to minimize leakage to the environment. In a canned motor pump, the impeller is directly mounted on the motor shaft and the pump bearing is usually cooled and lubricated by the pump process liquid.

To be employed in oil field, CMP must have the ability to work under multiphase flow conditions, which is a common situation for artificial lift. In this study, we studied the performance and reliability of a vertical CMP from Curtiss-Wright Corporation in oil and air two-phase flow condition. Part of the process liquid in this CMP is recirculated to cool the motor and lubricate the thrust bearing. The pump went through varying flow rates and different gas volume fractions (GVFs). In the test, three important parameters, including the hydraulic performance, the pump inside temperature and the thrust bearing load were monitored, recorded and analyzed.

The CMP has a second recirculation loop inside the pump to lubricate the thrust bearing as well as to cool down the motor windings. Since the second loop will lower the pump hydraulic performance, CFD simulation was carried out to analyze the effect of different flow rates and GVFs on the heat transfer in the recirculation channel. The simulation results show that reducing the current recirculation flow rate by 50% will only increase the recirculation outer wall temperature about 1 K. When 20% GVF air is presented in the recirculation flow, the wall temperature shows a maximum of 5 K increase.

The CMP has both pump-out-vanes (POV) and ribs on pump casing to control the axial thrust. The CFD results show that the current vane and rib geometries are already optimized and the axial thrust is always controlled at a low level at different working condition. The POV increases the pump power consumption and lowers pump overall efficiency.

DEDICATION

To my wife, daughter, parents and sisters.

ACKNOWLEDGEMENTS

I would like to thank Dr. Morrison for all the support and encouragement during my PhD study. It was a great experience to work under his supervisory.

I would like to thank my committee chair Dr.Delgado for all his help and support in finishing my PhD study. Thanks also go to my committee members, Dr.Kirkland, Dr.Pate and Dr.Han for their support and advice during the course of my PhD study.
I would like to thank Dr.Struart Scott and Hector Casillas from Shell Inc for providing financial support for this project. Eirc Conaway, Rayan Mesiano and Jose Matos from Curtiss Wright provided a lot of technical support. I would like to thank them for their help.

I would like to thank my colleagues in Turbomachinery lab during my PhD study, special thanks to Dr.Abhay Patil, for your help and friendship. Thanks to Wenfei, Changrui, Yiming, Peng, Yi, Sujan, Sahand, Scott, Ke, Clayton, Wenjie, Min, Marry and Burak.

Last, I would like to thank my families. My wife Jiaoli Yang, who supports and encourages me whenever I feel upset. I thank my daughter Ruoxu Wang for bringing me the joy of being a father. I thank my parents and my sisters for their devotion and love.

CONTRIBUTORS AND FUNDING SOURCES

Contributors

This work was supervised by a dissertation committee consisting of Professor Dr.Delgado advisor and Dr.Pate, Dr.Han of the Department of Mechanical Engineering and Professor Dr.Kirkland of the Department of Nuclear Engineering.

The test rig was built by Yintao Wang and Wenfei Zhang together. Dr.Morrison supervised the test and provided advices to the thesis.

All other work conducted for the dissertation was completed by the student independently.

Funding Sources

Graduate study was supported by Royal Dutch Shell.

NOMENCLATURE

CMP	Canned Motor Pump
ESP	Electrical Submersible Pump
cSt	Centistoke
CFD	Computational Fluid Dynamics
T	Temperature
U	Axial Velocity
V	Radial Velocity
W	Tangential Velocity
ε_H	Eddy Diffusivity
ε_{Hr}	Eddy Diffusivity in Radial Direction
$\varepsilon_{H\theta}$	Eddy Diffusivity in Tangential Direction
r	Cylinder Radius
R_i	Inner Cylinder Radius
R_o	Outer Cylinder Radius
Nu	Nusselt Number
a	Radius Ratio
Pr	Prandtl Number
Re_t	Tangential Reynolds Number
Ta	Taylor Number
ω	Revolution Speed

F_g	Geometric Factor for Taylor Number
R_m	Logarithmic Average Radius
Re_a	Axial Reynolds Number
$\mathrm{Q_{motor}}$	Motor Recirculation Flow Rate
$\mathrm{Q_{statorjacket}}$	Jacket Flow Rate
$\mathrm{Q_{inlet}}$	Pump Inlet Flow Rate
D_h	Hydraulic Diameter

TABLE OF CONTENTS

Page

LIST OF FIGURES

Page

LIST OF TABLES

Page

1. INTRODUCTION

The Canned motor pump (CMP) was introduced to industry decades ago to handle hazardous and toxic fluids. It integrates the motor within the pump itself so that the torque applied to the pump is generated internally. This design eliminates the opening through which the pump shaft is engaged with the external driver. A section view of a commercial CMP is shown in Figure 1-1. Different from normal pumps, a small part of the pressurized fluid is recirculated internally through the motor to cool down the motor as well as to lubricate the motor bearings. This unique construction offers several advantages over conventional mechanical sealed pumps: lower leakage risk, eliminates leakage and emission inspections, lower maintenance expenses due to reduced failure of mechanical seals, and lower noise and vibration caused by shaft misalignment.

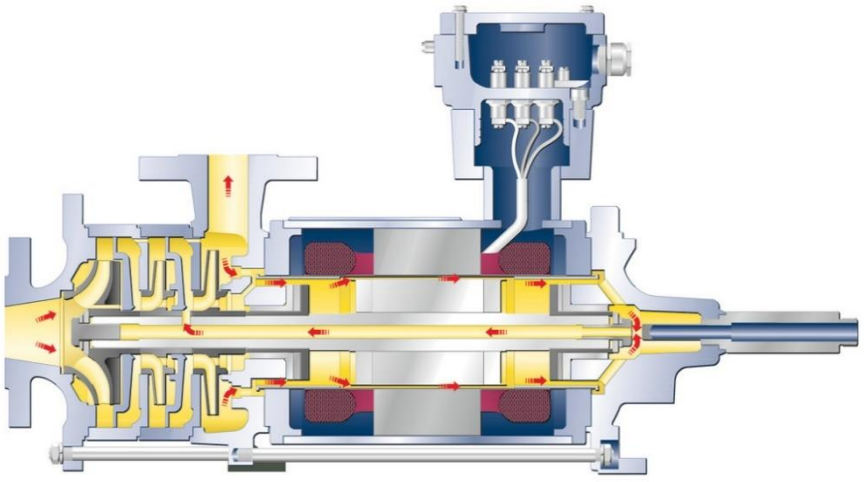

Figure 1-1 A multi-stage CMP with flow path indicated

In the oil field, the losses from suspended operation caused by the failure of downhole pumps together with the cost to retrieve and replace the failed pumps significantly reduce company profits. With the high reliability and the leak-free design, the CMP is an ideal alternative to a traditional electrical submersible pump (ESP) for artificial lift by both reducing company loss and lowering the risk of oil leakage. However, the harsh downhole working conditions, especially the multiphase flow condition, represent a challenge for a CMP, which was designed to handle single-phase liquids. To evaluate the feasibility of employing CMPs in a downhole environment, a vertical CMP with axial flow path manufactured by Curtiss-Wright Corporation was tested using an oil-air mixture multiphase flow at the Texas A&M University Turbomachinery Laboratory.

1.1. Literature review

The design principle of the CMP dates back to 1914 when Benjamin Graemiger obtained a patent titled: “the electric motor drive for a gas-tight machine enclosed in a casing [2]”. Usage was limited until the early 1950s when the expansion of nuclear technology required the development of hermetically sealed pumps for safety consideration. In the 1970s and 1980s, the industry standards and environmental considerations became increasingly important and the traditional sealed pump no longer fulfilled these requirements. In the same period of time, since CMP technology evolved and the pump design upgraded, it became widely utilized in other industries and many other fields. From the perspective of expenses, a study [3] about the cost of a standard pump ownership over 20 years shows that the initial purchase price only takes 5% of the

cost while the remaining 95% goes to maintenance, operating and installation. Among the maintenance, mechanical seal failure and bearing breakdown rank the top 2 cost. Because CMPs have fewer or even no mechanical seals, they can reduce the maintenance due to the mechanical seal failure.

1.2. Engineering of Canned Motor Pump

Guardiani [4] designed and studied a CMP specially manufactured for dealing with nuclear waste, which is actually the predecessor of the pump tested at the Turbomachinery Laboratory. Since radioactivity of the nuclear waste has a long life, the designed pump features a variable speed, submersible canned motor pump, with a long life without maintenance, zero leakage and highly flexible capacity. The pump is also required to meet other critical parameters: Operate for 10000 hours without maintenance over 10 years; Operate with a fluid viscosity between 1.0 and 30 cSt; Tolerate process fluid with up to 50 percent solids by volume and particle sizes up to 1 mm; Operate without any external cooling and lubrication system.

Figure 1-2 shows the internal circulation flow of the pump [4]. The fluid comes from the bottom suction nozzle and then is accelerated by two pumps stages as it enters the annular channel. The main stream of the fluid exits from the head junction while a small part of the fluid flows through a passage around the rotor to cool the motor and lubricate the bearings. The internal flow progresses down and rejoins the process fluid exiting from the pump stages.

Two radial bearings and one thrust bearing are employed in the pump, which are cooled and lubricated by the process fluid. A full-scale impeller and diffuser model were

tested with air to predict pump hydraulic performance with water and air mixture. Optimum impeller seal size and second stage diffuser were chosen based on the test results. The internal circulation flow rate was calculated based on the model test with a 450 ft head and 140 GPM discharge flow rate. The internal motor flow rate was found to be 66 GPM for water and 45 GPM for the process fluid with 1.5 specific gravity and 30 cSt viscosity. These results were later used for motor temperature calculations. The maximum winding temperature was found in the winding end with a maximum temperature of 205^{o}F when the ambient fluid was 200^{o}F. The prototype pump was finally tested in the field with water and process fluid. All the parameters met or exceed the given requirements.

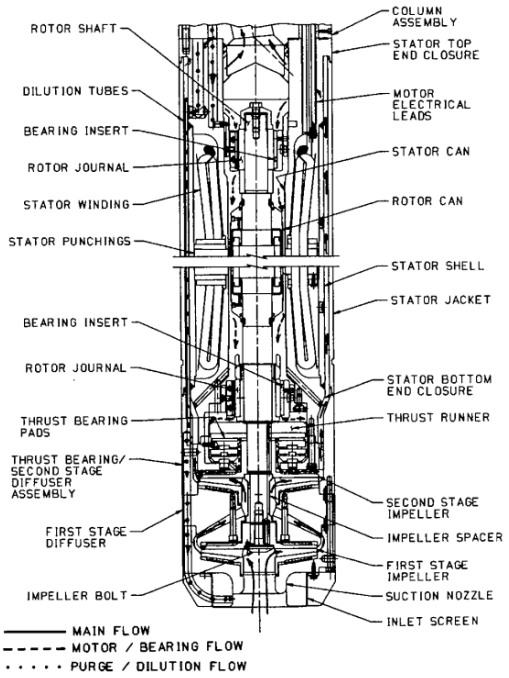

Figure 1-2 Internal circulation flow loop in the nuclear waste transfer pump

As a centrifugal pump, a CMP is by nature not immune to unbalanced thrust problems. In a study from Shell Company [5], seven CMP failures were analyzed and all of them point to increased axial thrust towards the inlet. Figure 1-3 shows the section view of the thrust bearing installed in the CMPs. It was found that in each failure, the carbon ring was heavily rubbed and damaged. In a typical failure mode as shown in Figure 1-4, the axial position moved and both power supply and winding temperature increased significantly. The failure was firstly assumed to be from the unbalanced axial thrust.

Two modifications were made to balance the axial thrust (Figure 1-5): 1. Vortex breaker strips were created on the suction end of the pump; 2. Balancing holes were enlarged to facilitate balancing action. The later test showed that the modifications improved the stability of the shaft axial position, but the pump still failed after 55 days of operation with a mode of increased power consumption and winding temperature. Exhaustive investigation and analysis showed that the root of the failure was galvanic corrosion caused by electrolytic cell between the cast iron wear ring on the impeller and other stainless-steel parts with water as electrolyte. So, when the cast iron wear ring corroded away, the wear ring clearance increased while the pressure on the suction side of the impeller dropped. The net thrust force towards the suction side forced the shaft to move and pressed the rotor thrust onto the carbon ring assembly. As the carbon ring rubbed and deteriorated, the increasing friction caused a rise in power consumption and winding temperature until the pump finally failed.

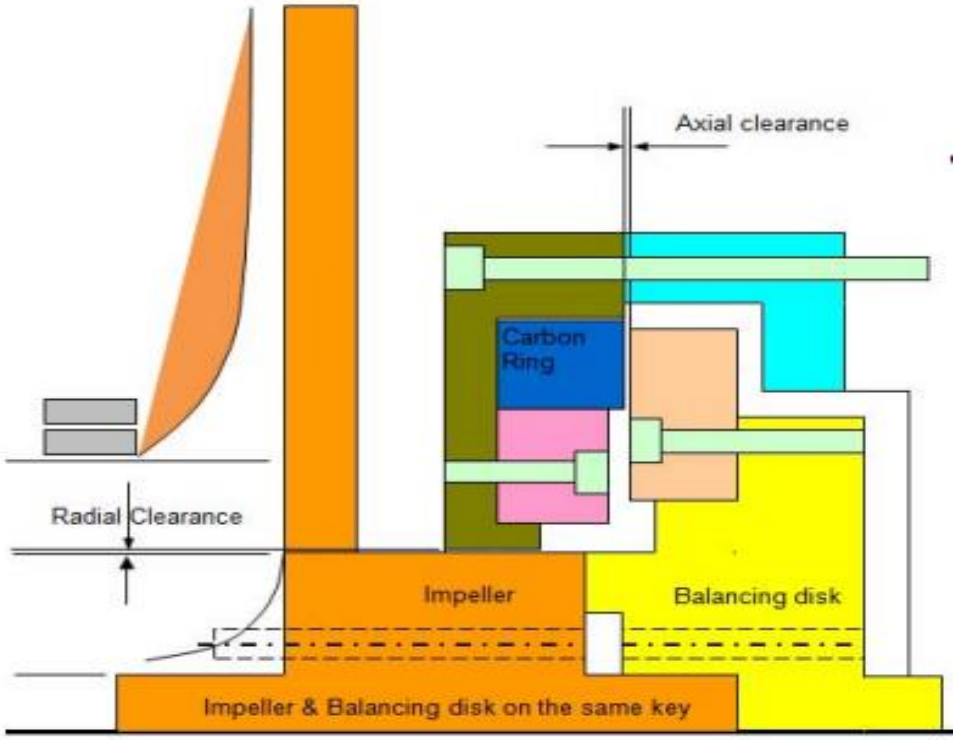

Figure 1-3 Section view of the thrust bearing installed in the CMPs

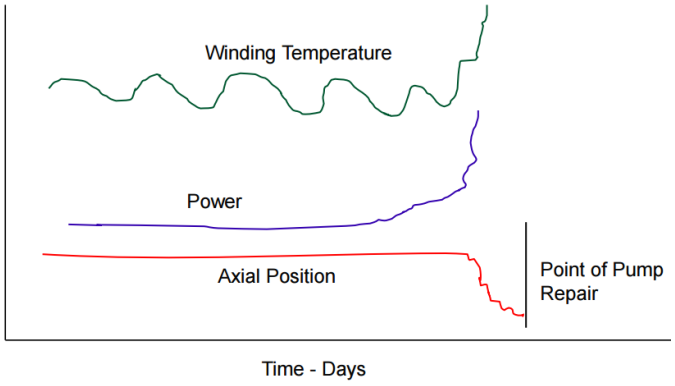

Figure 1-4 Observed typical failure mode

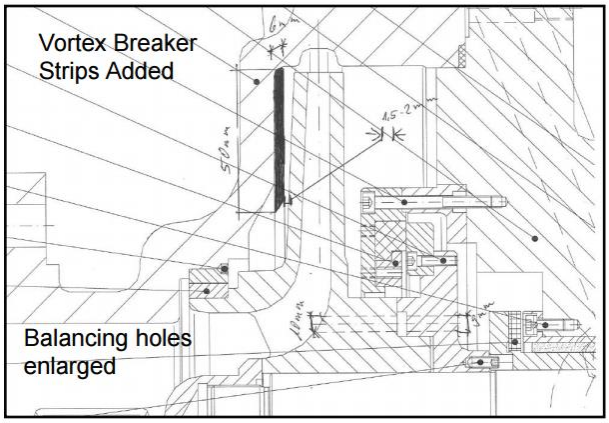

Figure 1-5 First modifications to balance the axial thrust

The unbalanced radial thrust might lead to severe consequences in CMPs. Bruckner [6] conducted a study on the failure of canned motor pump utilized in the thermal control loop in the international space station (ISS). The active thermal control system in ISS has a canned motor pump (Figure 1-6) to circulate pressurized liquid ammonia from the internal habitat to external radiator for heat rejection. The pump failed and jeopardized both the ISS' operation and the astronauts' lives. The failed pump was finally taken down to the earth and investigated. Severe wear was found on the two carbon journal bearings and the carbon thrust bearing, with the worst wear located on the rear journal bearing. A wear pattern, shown in Figure 1-7, was found to be related with an angular misalignment, which indicated a strong specific static force was acting directly on the journal bearing. Five possible bearing loads were proposed: 1. Residual unbalance of rotating assembly; 2. Residual magnetic asymmetry; 3. Annulus fluid inertia force; 4. Load alignment with respect to bearing pad; 5. Lubricant jet force on rear bearing. The last one was finally identified as the root cause of the bearing failure.

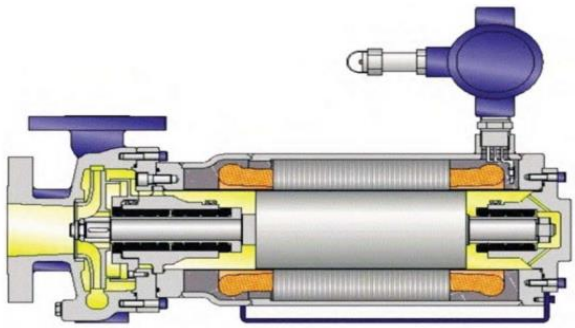

Figure 1-6 A typical canned motor pump for actively thermal control system for space application

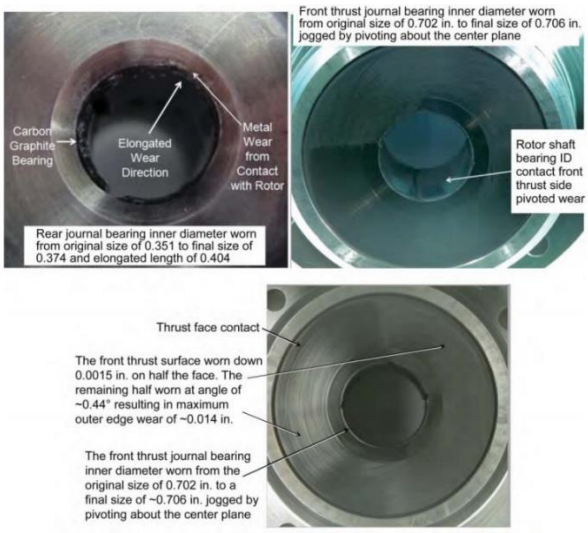

Figure 1-7 Wear pattern in the journal bearings and the thrust bearing

Kevin [7] compared the methods of controlling centrifugal pump axial thrust and optimized the axial thrust control in a CMP. The first method, the balance drum and disc, operates on the same principle of discharging the pressure on the area where the thrust generated. Another way to reduce the surface force on the impeller is to use ribs to disturb the pressure profile and thus control the axial thrust. Since both methods can decrease of pump efficiency, a specially designed tandem axial thrust control system was

adopted to control the thrust on a CMP. By controlling the rear shroud leakage, the thrust decreased under various operating conditions while the pump performances evidently increased.

1.2.1. Thrust force in centrifugal pumps

In common centrifugal pumps, there are two kinds of thrust that affect pump performance: radial thrust and axial thrust. The radial thrust is mainly generated from the unevenly distributed pressure inside the volute casing. It will affect the pump in several ways: increasing the load force on bearing and lowering bearing life span; Making seals wearing faster; Bending pump shaft and lowering pump efficiency; Increasing pump vibration and maintenance.

Axial thrust is another constrain in centrifugal pump design. Figure 1-8 shows the pressure distribution on a single stage pump at operation including the relevant forces.

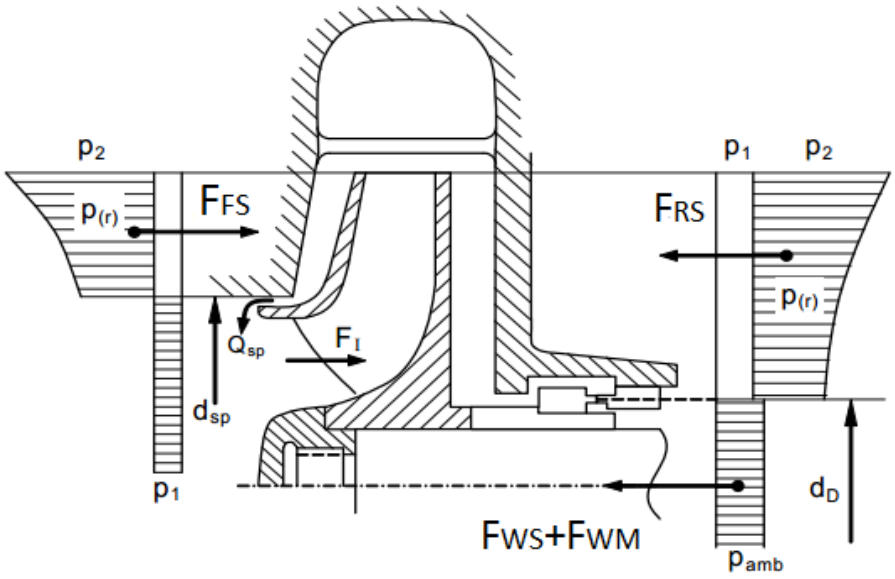

Figure 1-8 Pressure and force distribution on a single stage impeller

The forces F_{FS} and F_{RS} are generated by the pressure on the front and rear shroud of the impeller. F_I is caused by the momentum of changing the processing fluid velocity as well as the pressure exerted on impeller eye. F_{WS} results from the static pressure difference between the upstream and downstream of the shaft seal on the shaft and impeller relevant cross section. F_{WM} is all other axial forces such as weight of the impeller, shaft assembly and magnetic pull from the electrical motor.

The large pressure difference on the two shrouds of the impeller causes high axial thrust. For open impellers, since there is no shroud on which the pressure force is generated, the axial thrust is lower. The semi-open impeller has very high axial force because the large backface is directly exposed to the high pressure on the back side and a radially increasing pressure on the front side. For the closed impeller with shrouds on both sides, the axial thrust can be balanced through drilling balance hole, using backface vanes, or pump-out-vanes, as shown in Figure 1-9. The unbalanced axial thrust can severely impact the operation of a pump and thus thrust balancing methods are necessary even through these methods have a negative effect on pump efficiency.

In industry, the axial thrust is usually balanced or controlled through various ways[9]:

1. Completely absorb the axial thrust via a thrust bearing; the bearing size depends largely on accurately predicting or measuring the axial thrust.
2. Reduce the thrust by design using a back-to-back arrangement of the impellers and absorb the residual thrust through a thrust bearing.

3. Use balancing devices such as balance disk or a balance drum to completely or partially balance the thrust.
4. Reduce the thrust on an individual impeller by using an impeller seal, balancing holes on impeller and vanes on the impeller backface as well as on the impeller front casing.

Guelich[8] summarized the origin of hydraulic forces on centrifugal impellers and analyzed the dominating factors that affect these forces. In pump technology, the general empirical method for predicting the axial thrust is based on a velocity ratio factor K=0.5. The factor K represents the ratio of the rotating velocity of the liquid in the impeller-casing gap and the rotating velocity of the impeller itself. The K value affects the pressure distribution on the impeller shroud and backface and also the resulting axial thrust. In general, K is greater than 0.5 in the front shroud gap and less than 0.5 in the backface gap. Accumulative errors can be introduced when using 0.5 for multistage pump axial thrust calculation.

By adopting vanes or ribs on the shroud of the impeller or the pump casing, the velocity ratio factor can be controlled resulting in reduced axial thrust. When ribs are installed on the impeller backface, the liquid in the backface gap is forced to rotate at a higher circumferential velocity, thus lowering the average pressure on the backface. On the other hand, the ribs installed on the front pump casing can slow down the circumferential velocity and increase the average pressure on the impeller front shroud. The combined result is a decrease in the axial thrust towards the pump inlet.

The chief advantage of employing ribs is their simplicity for installation while its limitations are obvious[10]. The clearance between the rib top and the pump casing is very important and is usually kept between 0.4 and 1 mm. However, the axial movement of impeller and wear of the ribs make it difficult to maintain this clearance. Also, the ribs can introduce more friction loss and thus can decrease the pump efficiency by as much as 3%[11]. Radial ribs with rectangular sections are often adopted and sometimes ribs with the same contour of the impeller blades are employed. It is believed that the later design will have little or no efficiency impairment since these ribs essentially create the same pressure rises as the main blades[8].

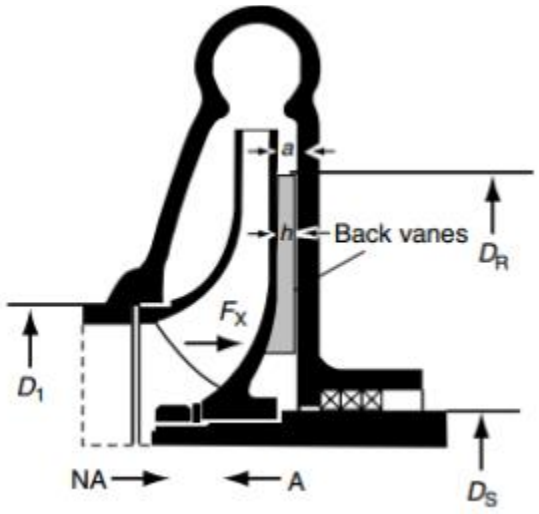

Figure 1-9 Closed impeller with back vanes and no back wearing rings

Since the additional power consumption by the ribs increases with 5^{th} power of their outer diameter while the pressure differences are proportional to the square of the diameter, it is suggested that power consumption can be reduced by selecting ribs with

diameters smaller than the impeller diameter and the pressure relieve result is little affected by the reduced rib diameter.

There are already detailed methods to theoretically calculate axial thrust in a centrifugal pump, in which pressure distributions are usually assumed. When thrust balancing devices, like back vanes, balancing disk and drums, are presented in the geometry, the pressure distribution can be very complex. Also, as the impeller and casing wear with operation, the clearance between the impeller backface and pump casing. Thus, the assumed pressure distribution can generate significant error for thrust calculation. For these cases, CFD or experimental test data can help to obtain more accurate thrust calculation results.

1.2.2. Heat transfer in a Canned Motor Pump

1.2.2.1. Heat generations in an induction motor

Venkataraman et al. [13] analyzed the surveys from IEEE (Institute of Electrical and Electronics Engineers) and EPRI (Electric Power Research Institute) on motor reliability and major causes of motor failure. They concluded that many failures are directly or indirectly caused by overheating of the different motor parts during operation[13]. When a motor overheats, the stator insulation will age and degrade significantly and the rotor conductor's capability to resist bending forces decreases as well. When motor temperature goes above the designed limit, the insulation doesn't fail immediately but the insulation's life expectation can be significantly reduced. The Arrhenius equations[13, 14], which governs the chemical deterioration process in

insulation, reveals that the increase of 10^{o}C over the operating temperature limit will cut the insulation life expectancy by half.

The heat generation in an induction motor can be divided into four groups: Joule losses, iron losses, stray load losses and mechanical losses[15]. The Joule losses are caused by the conductor resistance. They are proportional to the square of the current and occur in the stator copper winding and in the squirrel cage aluminum bars. The iron losses are divided into two parts: hysteresis losses that are due to the energy loss from aligning the iron magnetic poles to the applied magnetic field and eddy current losses that are due to the Joule losses from the induced current in the motor iron core. The stray losses are relatively small and difficult to quantify and they are due to the losses like skin friction. The mechanical losses include the losses friction of bearings and viscosity losses from the interaction between the rotating parts and the fluid (air, water, etc.) flowing inside the motor. All these losses will finally become heat generation in motors. Figure 1-10 shows the contribution of each group to the heat generation with relative scale.

The contribution of the stator and the rotor are of the same order and the actual difference can be affected by many design and operation factors. Juha Saari[16] systematically studied the losses in high speed induction motors. It was found that both the motor winding losses and rotor losses increase while the stator core losses decrease with slip ratio, as shown in Figure 1-11. The gap between the motor stator and rotor also affects the electrical losses in different locations and the rotor electrical losses become larger with narrow stator-rotor gap.

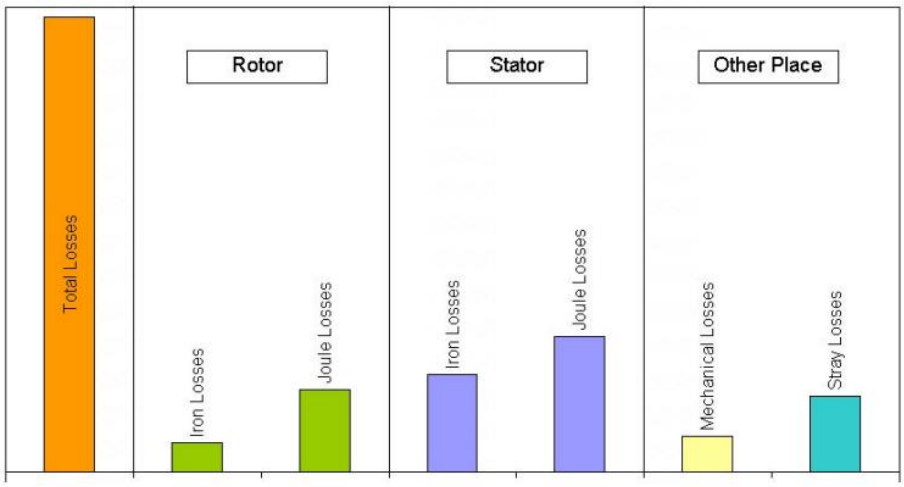

Figure 1-10 Contribution of each group to the total heat generation with relative scale

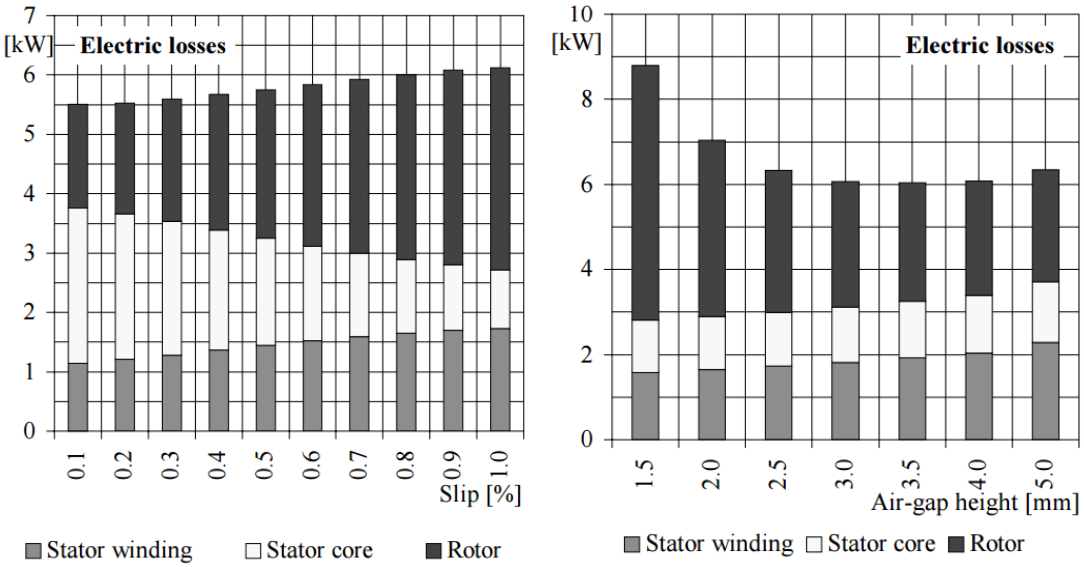

Figure 1-11 Motor major losses

The cooling passage of a CMP includes the main loop between the shell and the jacket, and the secondary loop between the motor stator and the rotor. The main loop is

modeled as a concentric channel flow. The second one can be modeled as flow between concentric rotating cylinders, also known as Taylor-Couette-Poiseuille flow.

1.2.2.2. Heat transfer in an annulus with two stationary concentric cylinders

For the fluid flowing through the annulus with two concentric stationary walls, Reynolds [17] studied the heat transfer problem in an annular passage and developed a general formulation for the heat transfer for defined wall temperature or heat flux. The development of the general equations follows these assumptions: 1. Velocity field is steady and independent of thermal field 2. In turbulent flow, eddy diffusivities in radial and tangential direction are independent of temperature field. 3. Eddy and molecular conduction are neglected in flow direction. 4. Temperature field is steady and fluid properties remain constant. The final simplified equation become:

$$\frac{\partial}{\partial \mathrm{r}}\left\{r(\varepsilon_{Hr}+\alpha)\frac{\partial T}{\partial r}\right\}+\frac{1}{r}\frac{\partial}{\partial \theta}\left\{(\varepsilon_{H\theta}+\alpha)\frac{\partial T}{\partial \theta}\right\}=Ur\frac{\partial T}{\partial x}+Vr\frac{\partial T}{\partial r}+W\frac{\partial T}{\partial \theta} \qquad 1.1$$

Where *T* is the temperature, *U, V, W* are the bulk averaged axial, radial, and tangential velocity components respectively, while ε_{Hr} and $\varepsilon_{H\theta}$ are the eddy diffusivity in radial and tangential directions respectively.

Reynolds evaluated the four fundamental solutions in the thermal energy regions and compared them to experimental measurements. The laminar fully developed flow heat transfer in the stationary annulus study by Lundberg[18, 19] include the following assumptions: 1. Axisymmetric temperature field 2. Incompressible flow with constant properties 3. Negligible axial heat conduction and effect of viscous energy generation 4. No internal heat source 5. Steady state conditions.

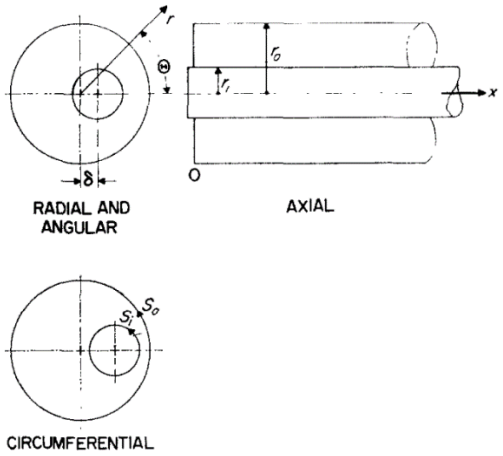

Figure 1-12 Coordinates and parameter definitions in Reynolds' study

The governing equation becomes:

$$\frac{\partial^2 T}{\partial r^2} + \frac{1}{r}\frac{\partial T}{\partial r} = \frac{U(r)}{\alpha}\frac{\partial T}{\partial x} \qquad 1.2$$

Four types of boundary conditions are considered: 1. Temperature arbitrarily specified on both walls 2. Heat flux arbitrarily specified on both walls 3. Heat flux arbitrarily specified on one surface and temperature arbitrarily specified on the other 4. Heat flux specified over a portion of one or both surface and temperature specified over another portion. Lundberg [19] determined the non-dimensional temperature, heat flux and Nusselt number results from the fundamental solutions for a range of radius ratios are presented.

Childs[20] arranged and summarized Leung's results as the following:

$$\theta_{lj}^{(k)} = \frac{T - T_e}{T_j - T_e} \quad \text{or} \quad \theta_{lj}^{(k)} = \frac{T - T_e}{q_j'' D_h / k} \qquad 1.3$$

$$\theta_{mj}^{(k)} = \frac{1}{AU_m}\int_A U\theta_{lj}^{(k)} dA \qquad 1.4$$

$$\emptyset_{lj}^{(k)} = -D_h \frac{\partial \theta_{lj}^{(k)}}{\partial n} \quad 1.5$$

$$Nu_{lj}^{(k)} = \frac{hD_h}{k} = \frac{\emptyset_{lj}^{(k)}}{\theta_{lj}^{(k)} - \theta_{mj}^{(k)}} \quad 1.6$$

Where $\theta_{lj}^{(k)}$, $\theta_{mj}^{(k)}$, $\emptyset_{lj}^{(k)}$ and $Nu_{lj}^{(k)}$ are the non-dimensional wall temperature, mixed mean temperature, heat flux and Nusselt number, respectively. The subscript *l* refers to the wall to be evaluated, *l=i* for inner wall while *l=o* for outer wall. The subscript *j* refers to the wall at which boundary conditions are applied, *j=i* for inner wall condition while *j=o* for outer wall condition. The subscripts *m*, *e*, *k* refer to mixed mean temperature, the value on annulus entry and the type of boundary conditions mentioned before. The results for the fundamental solutions are provided in both tables and graphics. The effect of heat transfer between the inner and outer wall through radiation are also evaluated. One of the finding for the laminar flow condition is that the maximum heat transfer due to radiation can be 10% of the total heat transferred, which happens at the inner wall heated condition.

For fully developed, incompressible, turbulent flow, including the eddy conductivity, the energy equation becomes[21]:

$$\frac{\partial}{\partial r}\left[r(\varepsilon_H + \alpha)\frac{\partial T}{\partial r}\right] = rU(r)\frac{\partial T}{\partial x} \quad 1.7$$

In another publication[22], fully developed, incompressible, turbulent flow was studied for boundary conditions with arbitrarily prescribed heat flux. The turbulent flow involved the heat transfer through eddy conductivity and a new term was added to the laminar equation, as shown in the above equation. Because the equations involve

Reynolds number and Prandtl number, the turbulent flow heat transfer is much more complex than in laminar flow. Thus, the author only studied the boundary conditions with specified heat flux. The authors provide fundamental solutions for this boundary condition and compared results to experimental data.

Although the series study from Reynolds, Kays and Lundberg presented their solutions in tabular and graphics in very detail, many researchers tried to obtain the correlations of the Nusselt number and Reynolds and Prandtl number. Many empirical correlation have been provided with verified with experimental data [22-27].

Dirker[28] presented several current available empirical correlation for Nusselt number and a comparison of the Nusselt number at a radius ratio, *a*, of 2 and Prandtl number of 3.37 with varying Reynolds number, as shown in Figure 1-13.

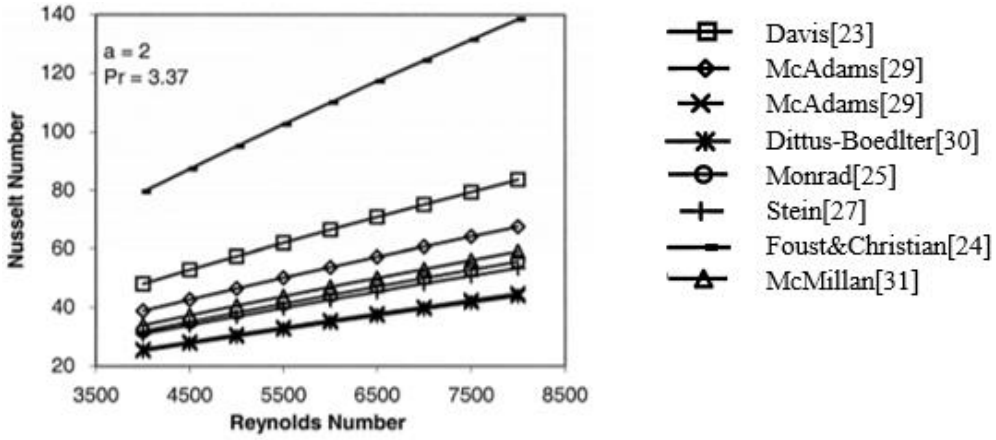

Figure 1-13 Comparison of empirical Nusselt number correlations by different authors

Although the available correlations are empirical, these are not consistent with each other. Dirker's proposed his correlations and compared them with experimental

results. The diameter ratio ranged from 1.68 to 5.04 while the Reynolds number varied from 2600 to 35000. Eq.1.8 and Eq.1.9 show the Nusselt number for the inner and outer walls, respectively:

$$Nu_i = \frac{h_i D_i}{K_i} = C_i Re_i^{0.8} Pr_i^{\frac{1}{3}} \left(\frac{\mu}{\mu_\omega}\right)_i^{0.14} \quad 1.8$$

$$Nu_o = \frac{h_o D_h}{K_o} = C_o Re_o^{P} Pr_{o,D_h}^{\frac{1}{3}} \left(\frac{\mu}{\mu_\omega}\right)_o^{0.14} \quad 1.9$$

P, C_i and C_o account for the geometry influence and for inner wall, *P* is 0.8. The modified Wilson plot method described by *Briggs* [32] can calculate the particular values of *P*, C_i and C_o.

For diameter ratio below 3.2, *P* and C_o had the following expression:

$$P = 1.013e^{-0.067a} \quad 1.10$$

$$C_o = \frac{0.003a^{1.86}}{0.063a^3 - 0.674a^2 + 2.225a - 1.157} \quad 1.11$$

These correlations from Dirker fit well with his experimental data, but still have some differences from the previous published correlations.

All the empirical correlations are based on experimental data, but the prediction from these correlations can diverge largely from each other. The geometry differences are one of the critical reasons. With the same diameter ratio, the actual annular gap can vary largely, and this significantly impact the flow pattern in the annuli and the heat transfer. The tested annuli and the fluid used for the test are the other affecting factors. Puchkov reported that the rough annular walls could yield up to threefold enhancement in heat transfer in comparison with smooth annular walls[33].

1.2.2.3. Heat transfer in Taylor-Couette flow

Taylor-Couette flow is the flow in a concentric annulus with rotating inner cylinder but no axial flow. The Taylor-Couette flow has three regimes: 1. Laminar shear flow 2. Laminar flow with vortices 3. Turbulent flows 4. Turbulent flow with vortices. There are several parameters that affect the heat transfer process:

The tangential Reynolds number[34]:

$$Re_t = \frac{\omega R_i D_h}{\nu} \tag{1.20}$$

When taking the geometric parameters and the viscosity of the fluid into consideration, the Taylor number can descript this kind of flow[34] better:

$$Ta = [\omega^2 R_i (R_o - R_i)^3 / \nu^2](1/F_g) \tag{1.21}$$

F_g is a geometric factor that is affected by the radius ratio and the roughness of the annulus. F_g can be 1 when the radius ratio approaches 1.

The flow is laminar when the Taylor number is lower than 1700. The tangential velocity decreases from the speed of the inner wall rotating speed at the inner wall to 0 at the outer wall. Conduction creates mostly of the heat transfer and the following equation[20] can calculate the Nusselt number:

$$Nu = \frac{2(R_o - R_i)/R_i}{\ln[1+\frac{R_o - R_i}{R_i}]} \tag{1.22}$$

Becker [35]gave another equation for the Nusselt number in terms of the Taylor number for the same flow condition:

$$Nu = 0.128(\frac{Ta}{F_g})^{0.367} \tag{1.23}$$

When the Taylor number is between 1700 and 10000, the flow presents a stable structure in an O ring form known as Taylor vortices (Figure 1-14). At this Taylor number, the vortices are usually steady and axisymmetric and the flow is still laminar.

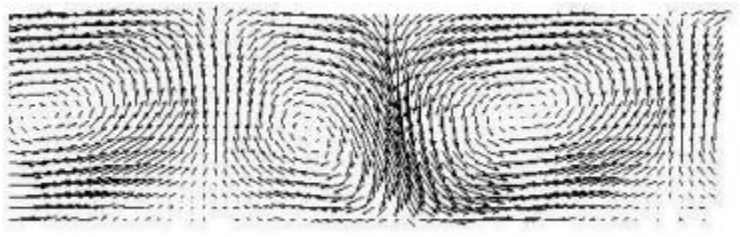

Figure 1-14 Example of Taylor vortices from Wang

The following equation from Becker [35] can calculate the Nusselt umber:

$$Nu = 0.409(\frac{Ta}{F_g})^{0.30.24167} \quad 1.24$$

$$F_g = \frac{\pi^4}{1697}(1 - \frac{b}{2R_m})^{-2}/\mathrm{P} \quad 1.25$$

$$P = 0.0571\left(1 - 0.652\frac{\frac{b}{R_m}}{1-\frac{b}{R_m}}\right) + 0.00056\left(1 - 0.652\frac{\frac{b}{R_m}}{1-\frac{b}{R_m}}\right)^{-1} \quad 1.26$$

Where $b = R_o - R_i$ is the annular gap and $R_m = (R_o - R_i)/\ln(R_i/R_o)$ is the logarithmic average radius.

As the Taylor number grows over 10000, the flow firstly becomes turbulent with vortices and eventually goes into pure turbulent flow regime. The correlation for Nusselt number given by Becker is:

$$Nu = 0.409(\frac{Ta^2}{F_g})^{0.241} \quad 1.27$$

Tachibana[37, 38] and *Ho*[39] verified these Nusselt number correlations in their experiments.

1.2.2.4. Heat transfer in Taylor-Couette-Poiseuille flow

The flow becomes Taylor-Couette-Poiseuille flow when axial flow presents in Taylor-Couette flow. A new parameter axial Reynolds number is introduced:

$$Re_a = V_a D_h / \nu \tag{1.28}$$

V_a is the axial flow velocity and D_h is the hydraulic diameter. Three important factors, axial flow velocity, geometry and thermal conditions can influence the flow pattern and geometry parameters is the prominent factor. Kaye[40] found that the flow pattern changed from laminar flow to turbulent flow more rapidly when the annular gap became narrower at Re_a<1500 while the effects would reverse when the axial Reynolds number went above 1500. In another study, Becker and Kaye[35] presented the effect of thermal gradient on the transfer of laminar flow to turbulent flow, but due to the limit of the experiment, the conclusions cannot be generalized. These researchers have generated different correlations for Nusselt number based on their experiment data. Confined by the testing condition, these Nusselt equations are mostly self-verified. But there are some common heat transfer patterns: in laminar flow, the Nusselt number is constant until the critical Taylor number. The critical Taylor number is the Taylor number when Taylor vortices appears and the critical Taylor number increases with the increasing axial Reynolds number. The Taylor vortices diminish the heat transfer while the turbulence increases the convective heat transfer.

Yoichi [41] experimentally studied the flow pattern of two-phase flow in Taylor-Couette-Poiseuille flow and he observed six patterns: dispersed bubbly, ring-form, single-spiral, double-spiral, triple-spiral flow and transition region. The rotating speed strongly affects the flow pattern.

Figure 1-15 shows the effect of rotating speed and fluid volumetric fluxes on flow pattern. When the rotation speed is low, the flow is bubbly flow. As the rotation speed increases and the Taylor number goes above the critical value, Taylor vortexes begin to form.

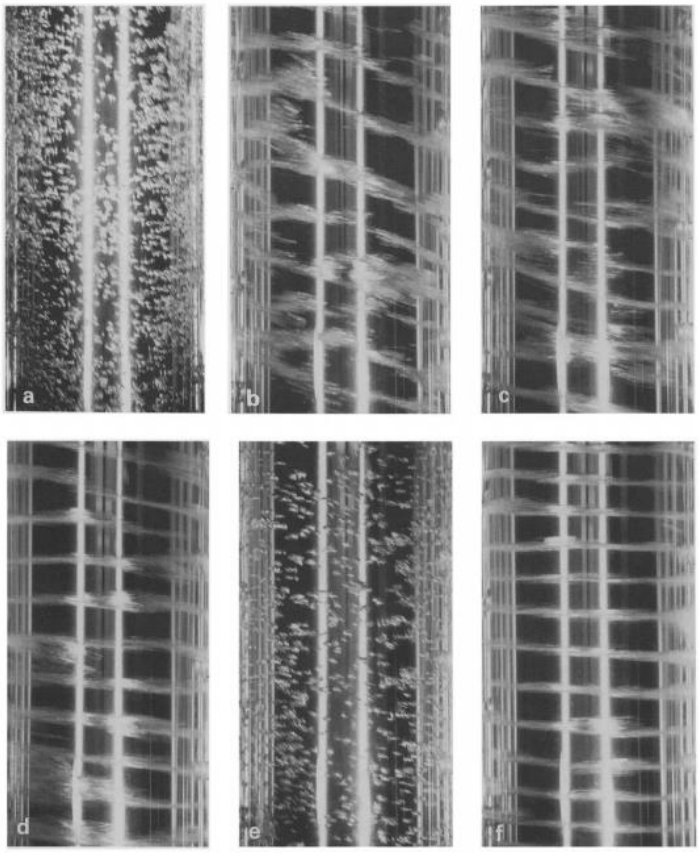

Figure 1-15 Flow patterns observed in two-phase Taylor-Couette-Poiseuille flow

Later, Yoichi [42] conducted an experimental and CFD study about two-phase flow in Taylor-Couette-Poiseuille flow. During the test, the water volumetric flux was 0-0.268 m/s while the air volumetric flux was 0-0.0647m/s. The tangential velocity at the inner wall was 0-7.54 m/s with a rotational speed of 0-800 RPM. The results showed that when the rotational speed was low, the bubbles travelled like in normal pipe because the buoyancy effect was dominating the transportation of the bubbles. When the inner cylinder rotation speed went up to a certain level, the Taylor vortex motion was dominating the bubble flow pattern. Figure 1-16 shows the bubble rings between the Taylor vortices.

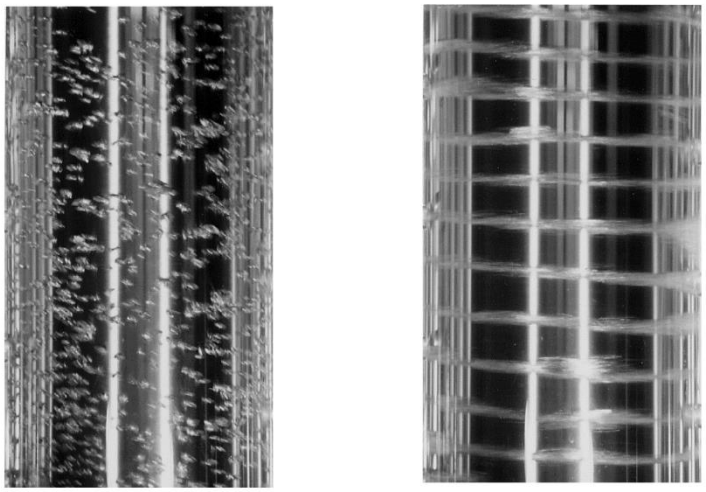

Figure 1-16 Bubbly flow vs Bubble-ring flow in Taylor-Couette-Poiseuille flow

Figure 1-17 shows the annular channel cross-section view. The bubble rings located close to the inner cylinder at the out-flow region of the vortices. The radial void fraction measurement by using a conductivity probe proved this phenomenon. Figure 1-18 shows the void fraction changes with time at different radial locations.

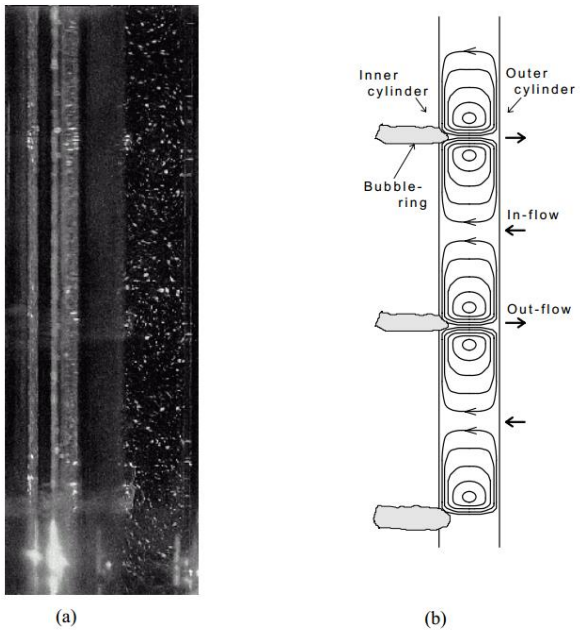

Figure 1-17 Location of the bubble rings

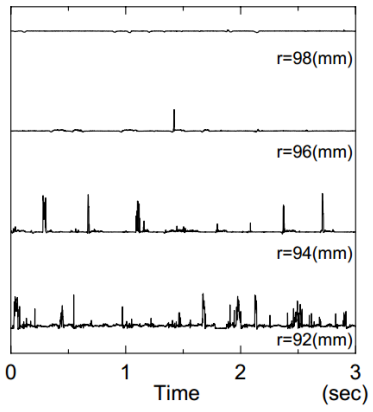

Figure 1-18 radial void fraction measurement by using conductivity probe

Madhu [43] conducted a study about the suspension of rigid particles in Taylor-Couette flow. Figure 1-19 shows the flow pattern transferred from Taylor vortex flow

(TVF), Spiral Vortex low (SVF) to circular Couette flow (CCF) at different Reynolds numbers.

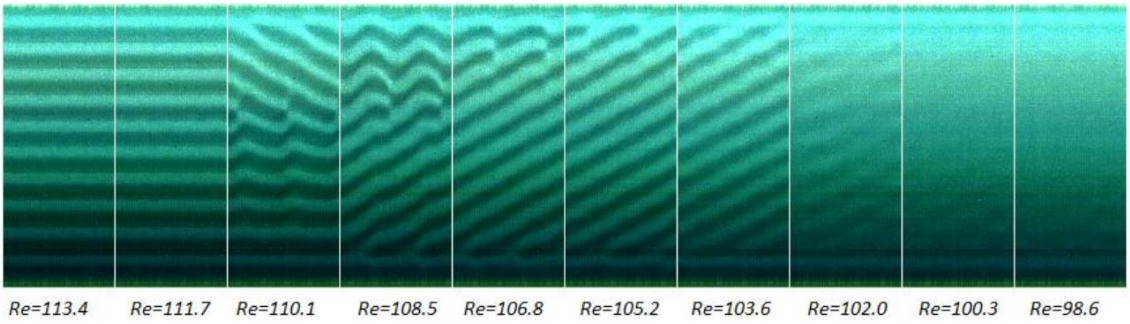

Figure 1-19 Change of flow pattern with reducing Reynolds number

2. OBJECTIVE

Multiphase flow is a common flow condition for the artificial lift process used in the oil industry. In the original designed applications of CMPs, the processing fluid is single phase. When applied to artificial lift, whether the oil-air mixture can supply enough cooling capacity to the motor is a large concern. Also, the thrust bearing faces challenges generating sufficient lift when running with oil-air mixtures. Due to the compact design and complex internal flow path, pure theoretical calculation and simulation is insufficient to evaluate CMP's performance. However, experimental tests can generate valuable information to evaluate CMP's performance.

First, we will build a closed-loop oil-air two-phase flow test rig to test the CMP's performance under two-phase flow conditions. In the test, we will we tested the pump hydraulic performance parameters, the motor temperature and the response of the thrust bearing in different working conditions. All the test results will compare with the CMP specifications to make sure all the test parameters are within design limit.

A CFD simulation of the recirculation channel will study how the recirculation flow rate and entrained air affect the motor cooling. The CFD results will help to optimize the pump design and improve pump efficiency.

In this CMP, pump-out-vanes and pump casing ribs are employed together to reduce the axial thrust. The CFD study of the POVs will systemically evaluate the POVs effect on axial thrust and pump efficiency. The CFD results will provide

recommendations on how to optimize the POVs to control the axial thrust and get better pump efficiency.

3. METHODOLOGY

3.1. Experimental setup

This section describes the test rig built at the Texas A&M University Turbomachinery Laboratory to carry out the CMP two-phase flow test. Figure 3-1 shows the P&ID (Pipe and Instrumentation Diagram) of the oil test facility. The rig comprises of two loops: the main loop that provides oil and air to the CMP and the cooling loop to cool the oil.

The centrifugal pump in the main loop pressurizes the oil exiting the separator and flowing thought a Coriolis flowmeter, a pneumatic control valve before entering the CMP. Because the centrifugal impeller can only handle a limited amount of air, the air injection holes are located at the stator jacket annulus after the second pump stage. The oil and air mix in the stator jacket annulus and exit at the top pump outlet. A pneumatic valve controls the outlet pressure. The oil-air mixture flows to the separator directing the air to the top and recirculating the oil to the main loop.

The oil temperature increases during the test and a second cooling loop removes the heat from the oil. The heat exchange occurs inside a shell-tube heat exchanger and the oil ejects heat to the cooling water. The heat water cools down in a finned air heat exchanger and then returns to the water tank.

Figure 3-2 shows the test pump installed in the main flow loop. Figure 3-3 and shows the separator, air heat exchanger, charging pump and flowmeter used in the test.

In consideration of the operation safety and environmental safety, the test liquid was silicon oil manufactured by the CLEARCO Company. Table 3-1 shows the properties of the silicon oil.

Table 3-1 Test oil properties

Density	920 kg/m3
Dynamic viscosity	0.0046 kg/(m s)
Heat capacity	1506 J/(kg K)
Thermal conductivity	0.108W/(m K)

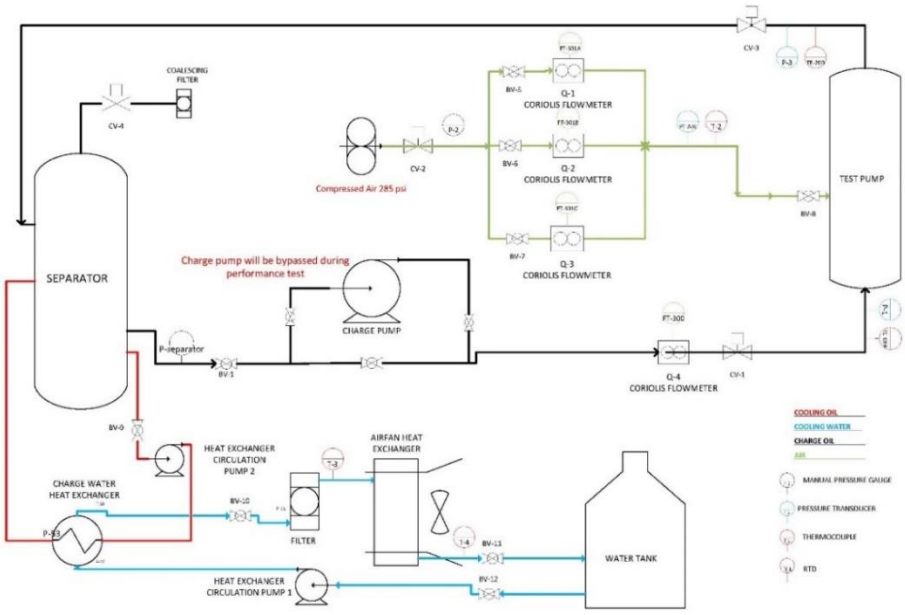

Figure 3-1 P&ID of the Canned Motor Pump oil test

Figure 3-2 Canned Motor Pump in main test Loop

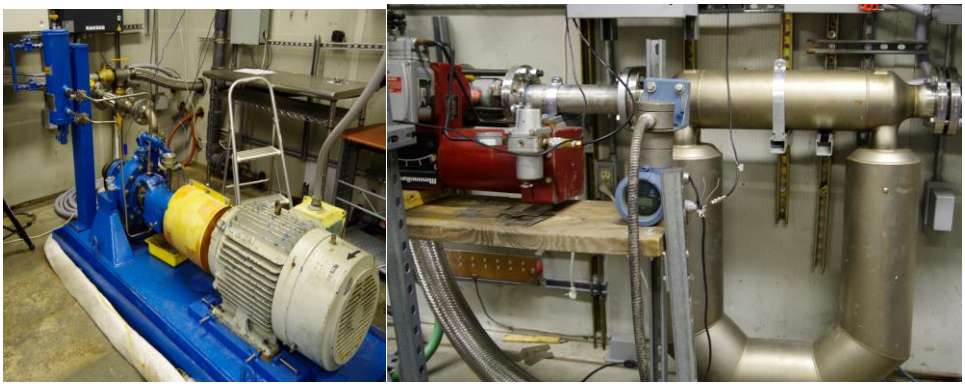

(a) (b)

Figure 3-3 (a) Oil charging pump; (b) Inlet flowmeter and control valve (c) Oil-Air separator; (d) Shell-Tube heat exchanger; (e) Cooling water tank and air-fan heat exchanger

(c) (d) (e)

Figure 3-3 Continued

Four Coriolis flow meter measured the oil and air flow and Table 3-2 shows the details location and specifications of the flowmeters.

Table 3-2 Flow meter specifications

Flow meter	Model NO.	End Connection	Range	Minimum accuracy
Water/Oil	CMF300M	3” 150# Flange	25-1200 GPM	±0.25%
Air	CMF010M	1/4” NPT	0.5-14 SCFM	±0.35%
Air	CMFS040	1/2” 300# Flange	10-150 SCFM	±0.25%
Air	CMF100M	1” 300# Flange	100-500 SCFM	±0.35%

Two tri-axial accelerometers, installed on the top and bottom flanges of the pump, monitor the pump vibration. Two proximity probes monitor the impeller lateral vibration. Table 3-3 provides general information about the transducers.

Table 3-3 Description of accelerometers and proximity probes.

Transducer	Model	Range	Resolution	Sensitivity
Accelerometer	PCB-356A17	±10g peak	0.00006 g in RMS level	500 mV/g
Proximity Probe	Bently Nevada-3300XL NSv	10 – 70 mils		200 mV/mil

Figure 3-4 shows the pressure measurement points along the pump. The differential pressure transducers have manual control valves on the high-pressure side and the low-pressure side. These valves only open after testing starts to prevent possible damage from hydraulic shock at the pump start-up. Table 3-4 shows the details of the pressure transducers. Table 3-5 and Table 3-6 show CMP's specifications.

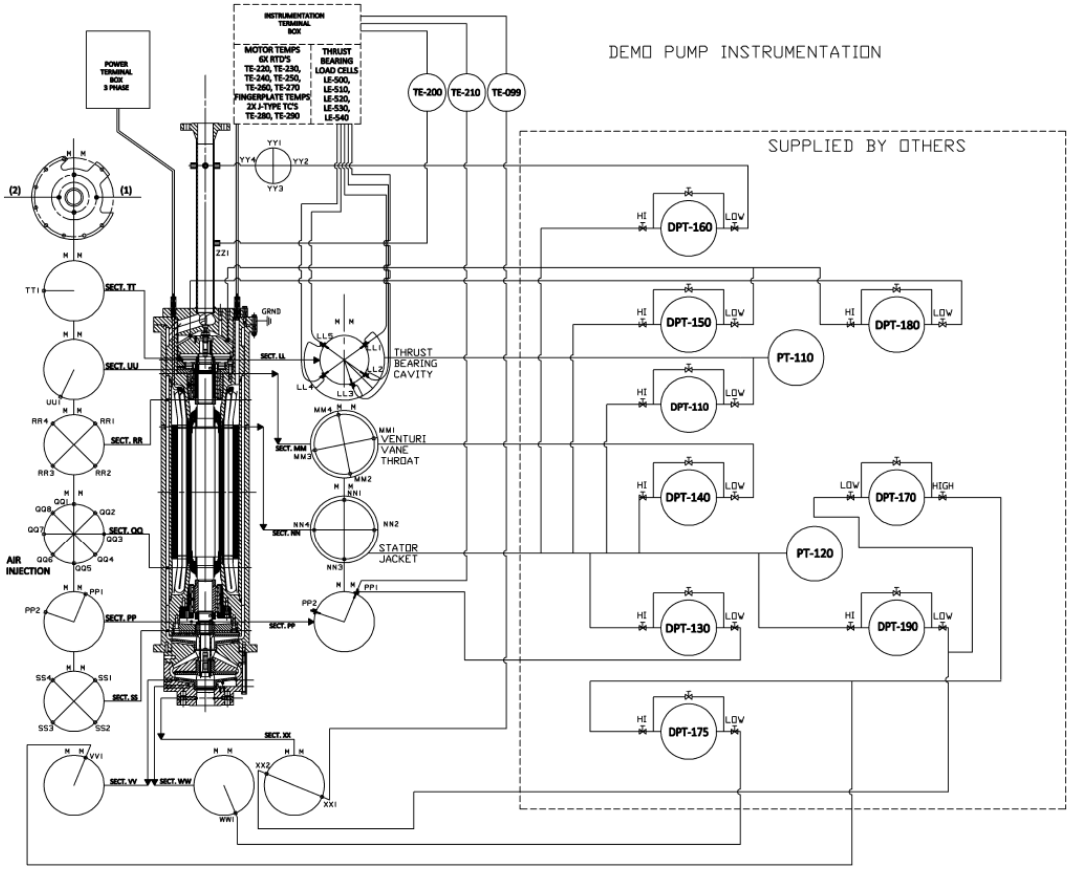

Figure 3-4 CMP pressure measurement setup

Table 3-4 Pressure transducers specifications

Label	Measuring Position	Transducer Model	Range (Psig)	Output	Accuracy
DPT-110	Thrust Cavity Relative Pressure	Omega-PX 429	0-30	4-20 mA	±0.08%
DPT-130	Hub Plate Cavity Relative Pressure	Omega-PX 429	0-50	4-20 mA	±0.08%

Table 3-4 continued

Label	Measuring Position	Transducer Model	Range (Psig)	Output	Accuracy
DPT-140	Venturi Relative Pressure	Omega-PX 429	0-30	4-20 mA	±0.08%
DPT-150	Thrust Runner OD Relative Pressure	Omega-PX 429	0-50	4-20 mA	±0.08%
DPT-160	Discharge Relative Pressure	Omega-PX 429	0-15	4-20 mA	±0.08%
DPT-170	1st Stage Impeller Pressure Rise	Omega-PX 429	0-150	4-20 mA	±0.08%
DPT-175	1st Stage Impeller Shroud Pressure Rise	Omega-PX 429	0-150	4-20 mA	±0.08%
DPT-180	Thrust Runner ID-OD Pressure Rise	Omega-PX 429	0-50	4-20 mA	±0.08%
DPT-190	Pump Hydraulic Differential Pressure	Omega-PX 429	0-500	4-20 mA	±0.08%
Label	Measuring Position	Transducer Model	Range (Psig)	Output	Accuracy

Table 3-4 continued

Label	Measuring Position	Transducer Model	Range (Psig)	Output	Accuracy
PT-110	Thrust Cavity Pressure	Omega-PX 429	0-500	4-20 mA	±0.08%
PT-120	Stator Jacket Diffuser Discharge Pressure	Omega-PX 429	0-500	4-20 mA	±0.08%

Table 3-5 CMP's specifications

Motor Parameter	Value
Nominal Motor Voltage	470 Volts
Nominal Motor Frequency	67.7 Hz
Nominal Motor Speed	3930 RPM
Nominal Motor Current	107.2 Amps
Power Factor	0.69
Vibration limit	Maximum 0.2 G RMS
Loop fluid temperature limit	Maximum 120 oF
Motor temperature limit	Maximum 428 oF
Pump speed limits	Minimum:2000 RPM; Maximum: 4300 RPM
Thrust limits in gravity direction	Minimum:250 lbf; Maximum: 1000 lbf
Flow rate limits	Minimum: 20 GPM; Maximum: 320 GPM

Table 3-6 Pump NPSH requirement

Pumped flow rate (GPM)	NSPHa (ft head)
0	0
100	7
140	11
300	47

3.2. Test control and data acquisition

Figure 3-5 shows the test control and data collection system setup. The National Instruments modules monitor and collect the pressure, temperature, vibration and displacement information and also control the main loop valves.

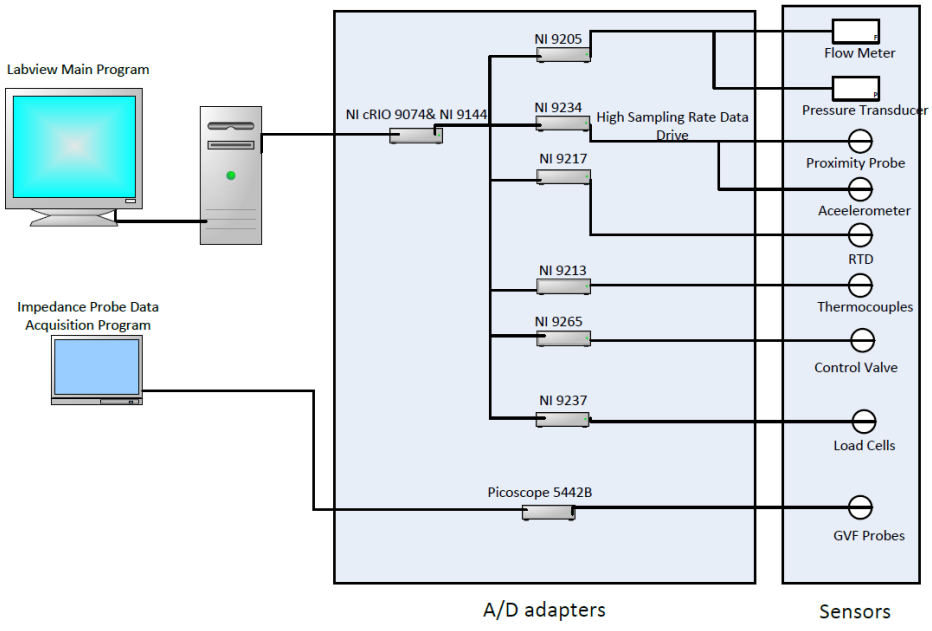

Figure 3-5 System control and data collection system setup

Figure 3-6 and Figure 3-7 show the main LabVIEW control program and the vibration LabVIEW monitor program. The LabVIEW program records the temperature, pressure and thrust load cell reading every one second and also records the average of these values every 60s. The program records the proximity and vibration data at 5.86 kHz sampling frequency. Another laptop records the impedance probe data to get the GVF information in the motor rotor-stator annulus. The pneumatic valves control both the oil/air flow rate and the pressure. A Variable Frequency Drive (VFD) controls the pump speed during the test.

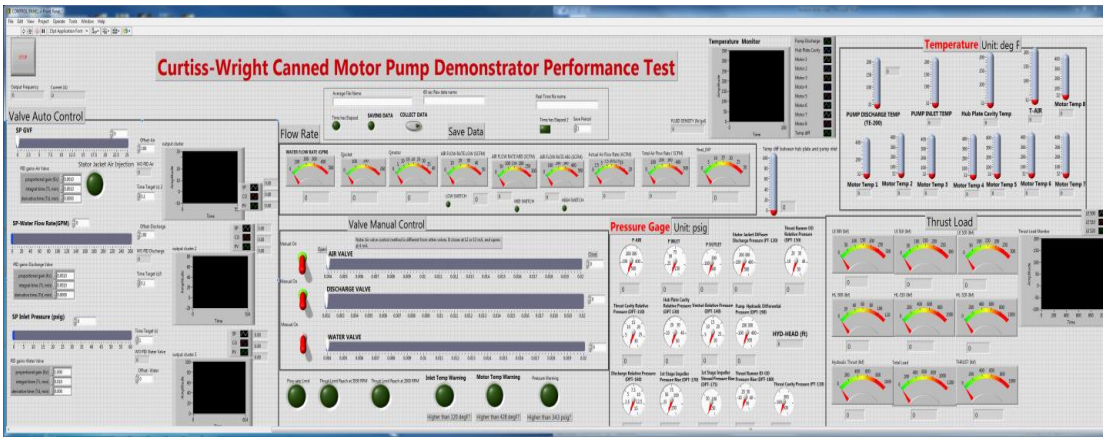

Figure 3-6 Main LabVIEW program control panel

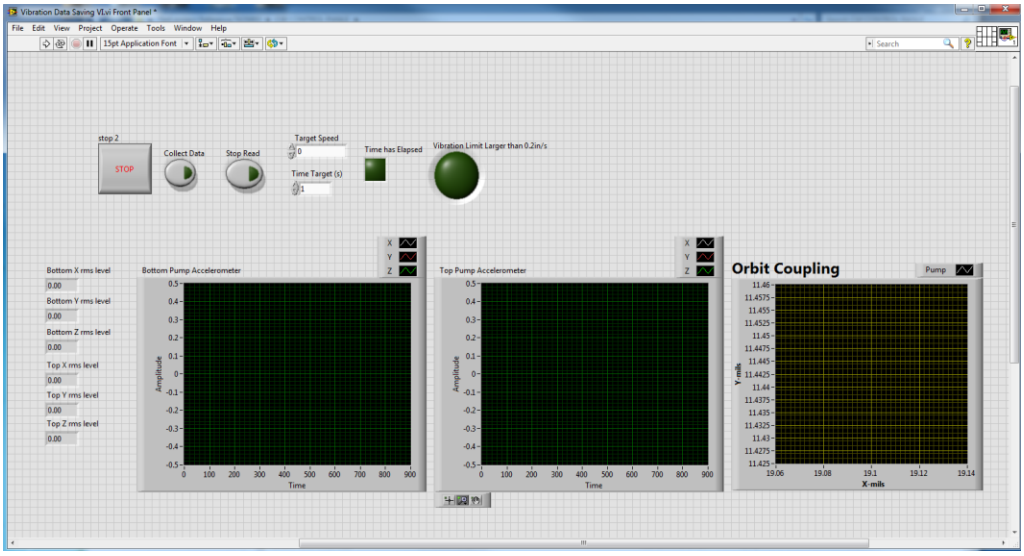

Figure 3-7 LabVIEW program of vibration data monitor panel

3.3. Test procedure

Figure 3-8 displays the flow passage inside the CMP. The fluid enters the CMP from the bottom and flows through the first stage impeller and diffuser. Then it passes the second stage impeller and enters the annulus formed by the stator and the stator jacket. The fluid moves through the second stage diffuser located at the bottom of this annulus. The fluid continues through the annulus and converges at the top of the pump through four cylindrical channels. There are four small openings in each of the cylindrical channels, and through these openings, a small part of the fluid enters the recirculation annulus path between the rotor and the stator. The recirculation fluid exits from the recirculation channel at the bottom of the motor and joins the main flow at the back face clearance of the second stage impeller.

The oil test comprises two parts: The Venturi calibration test and pump performance test. In the top section of the stator jacket annulus, there are sixteen Venturi

channels surrounding the annulus (Figure 3-9). A Venturi calibration process provided the correlations between the stator jacket flow rate and the Venturi channel pressure drop. With these correlations, this annular channel flow rate can be calculated by measuring the pressure drop through the Venturi channels. The internal flow path is blocked during the Venturi calibration process. The motor cooling flow rate Q_{motor} is nil and the stator jacket flow rate $Q_{statorjacket}$ equals the pump inlet flow rate Q_{inlet}. In the performance test, the pump inlet flow rate is directly measured by a flow meter and the stator jacket flow rate is calculated from the Venturi channel pressure drop. Then, the motor cooling flow rate Q_{motor} can be calculated as

$$Q_{motor} = Q_{statorjacket} - Q_{inlet} \tag{3.1}$$

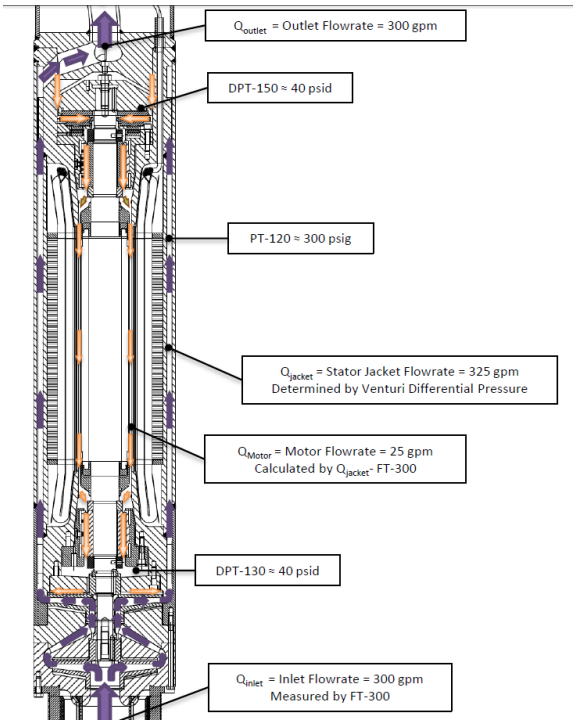

Figure 3-8 Curtiss Wright CMP flow passage sketch

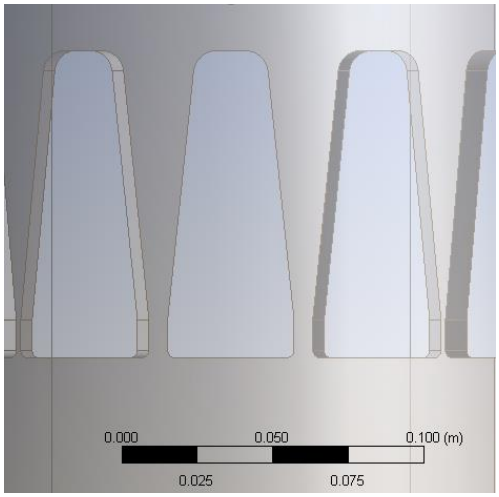

Figure 3-9 Venturi channels inside the annular channel

Table 3-7 Test matrix of oil baseline test

Speed (RPM)	Oil flow rate (GPM)
2000	25
	50
	75
	100
	125
3000	50
	75
	100
	125
	150
Speed (RPM)	Oil flow rate (GPM)

Table 3-7 continued

3700	50
	100
	150
	170
	200
3930	50
	100
	125
	150
	175
	200

Table 3-7 shows the test conditions in the pump oil baseline performance test. For oil-air two-phase flow test, air was injected into the stator jacket annulus under different operation conditions. Table 3-8 shows the two-phase flow test matrix.

Table 3-8 Test matrix of multiphase test

Speed (RPM)	Oil flow rate (GPM)	GVF %
2000	75	0
3000	100	3
3700	115	6
	130	9

Table 3-8 continued

Speed (RPM)	Oil flow rate (GPM)	GVF %
	150	12
	175	15
	190	20
	200	

3.4. Numerical simulation

In the numerical simulations, the commercial software ANSYS FLUENT is used and the simulations include two sections: 1. Simulation of the CMP motor recirculation channel thermal and hydraulic problem; 2. Simulation of the effect of pump-out-vanes (POVs) on both the pump axial thrust and pump performance.

3.4.1. Recirculation channel thermal and hydraulic simulation

Besides the flow channel geometries, the flow rate and fluid properties also affect the heat transfer and cooling effectiveness. The CFD simulation will aim at answering two questions: 1. Would a reduced recirculation flow rate still provide enough cooling for the motor? 2. Does the air in the fluid deteriorates the motor cooling, especially with a reduced flow rate?

The experimental results show that the dominant factor defining motor temperature is the running speed and the temperature gradients due to changes in running speed. Considering that peak temperature is the most important parameter affecting the motor life, the simulation study will focus on the high-speed situation at 3700 RPM, which is the limit of stable operation speed in two-phase flow test. The

recirculation flow rate is 40 GPM based on experimental test at this speed. The simulation will evaluate the effect of reduced flow rate on the heat transfer process. Figure 3-10 shows the Taylor number and axial Reynolds number at 40 GPM, 30 GPM and 20 GPM.

Figure 3-11 shows the recirculation channel geometry and the surfaces with heat transfer in the simulation. Based on the axial Reynolds number and Taylor number at the three flow rates, the flow inside is turbulent and Taylor vortex will not be present. Without the Taylor vortex, the bubble rings will not form and risk of high local temperature due to the bubble rings is eliminated. For this turbulent flow, the Nusselt number, *Nu*, grows with increasing axial Reynolds number[44].

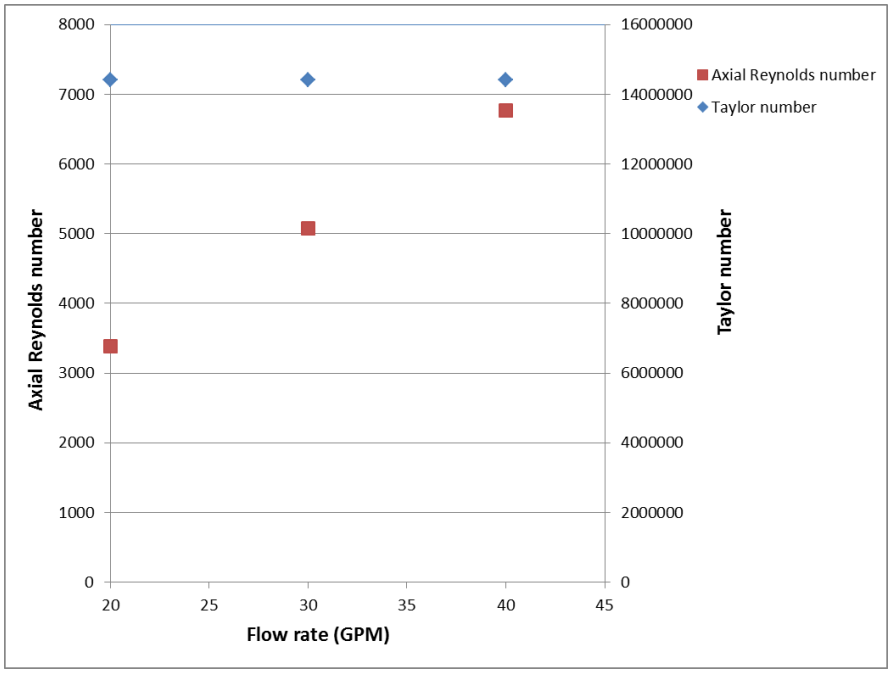

Figure 3-10 Axial Reynolds number and Taylor number at different recirculation flow rates

Tetrahedral elements are used to mesh the flow domain. The liquid enters from the top inlet and exits from the bottom. For the CFD simulation boundary settings, the inlet boundary condition is velocity with mixture phase and the outlet is pressure outlet with mixture phase. The inner surfaces rotate at 3700 RPM and the outer surface is stationary.

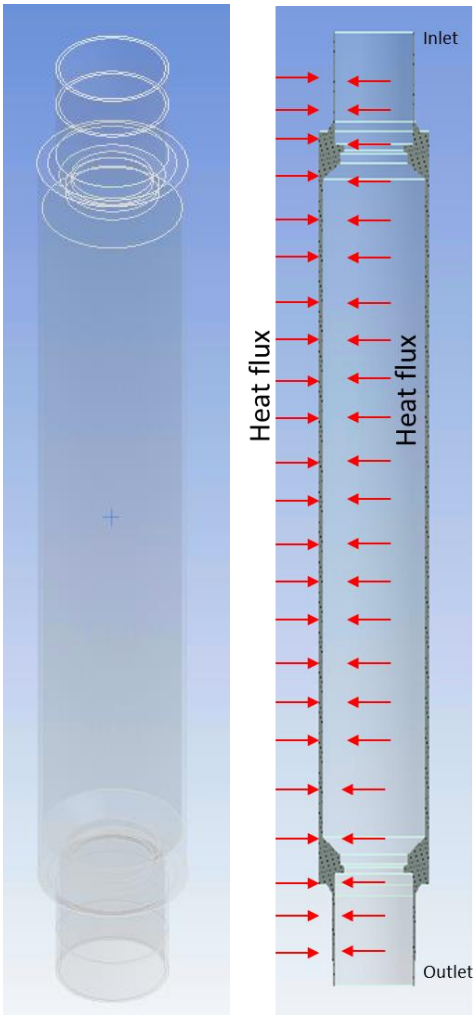

Figure 3-11 Recirculation flow channel geometry and heated surfaces

The CMP features a NEMA-MG-1 standard 60 HP motor with an efficiency of 93%-94% at full load[45]. At 3700 RPM and 150 GPM, the power input is 42.5 kW and the motor efficiency is assumed to be 93%. The 7% efficiency loss is assumed to become heat generation in the motor. As discussed in section 1.1.3.1, the assumed distribution of the heat generation inside the motor is 45% in the winding, 30% in the rotor and 25% in the core. The heat transferred to the recirculation flow includes 50% of the heat generated in the winding and core, and 100% of the heat generated in rotor. Table 3-9 introduces the assumed heat source from the stator and the rotor. Because the motor stator thickness and the rotor diameter are relatively small compared to the axial length, the heat transfer in axial direction of the stator and the rotor is neglected. The heat sources are converted to heat flux and applied to the cylinder surfaces shown in Figure 3-11. Table 3-10 shows the heat flux on each surface.

Table 3-9 Heat distribution in different components

Location	Heat from stator's winding and core	Motor rotor	Sum
Power (kW)	1.5	0.9	2.4

Table 3-10 Heat flux on the heated surfaces

Location in the recirculation channel	Middle cylinder surface of the outer surface	Middle cylinder surface of the inner surface
Heat flux (W/m2)	6446.35	4222.973

Table 3-11 shows the grid independence study with three different meshes at 3700 RPM, 40 GPM with silicon oil as working fluid. Figure 3-12 shows the pressure drop ratio change and temperature increase ratio change with different meshes. The simulation employs the 2.5 million-element mesh as it renders less than 1% variation.

Table 3-11 Mesh elements in grid independence study

Mesh	No. of Elements (Million)
Mesh-1	2.15
Mesh-2	2.50
Mesh-3	2.84

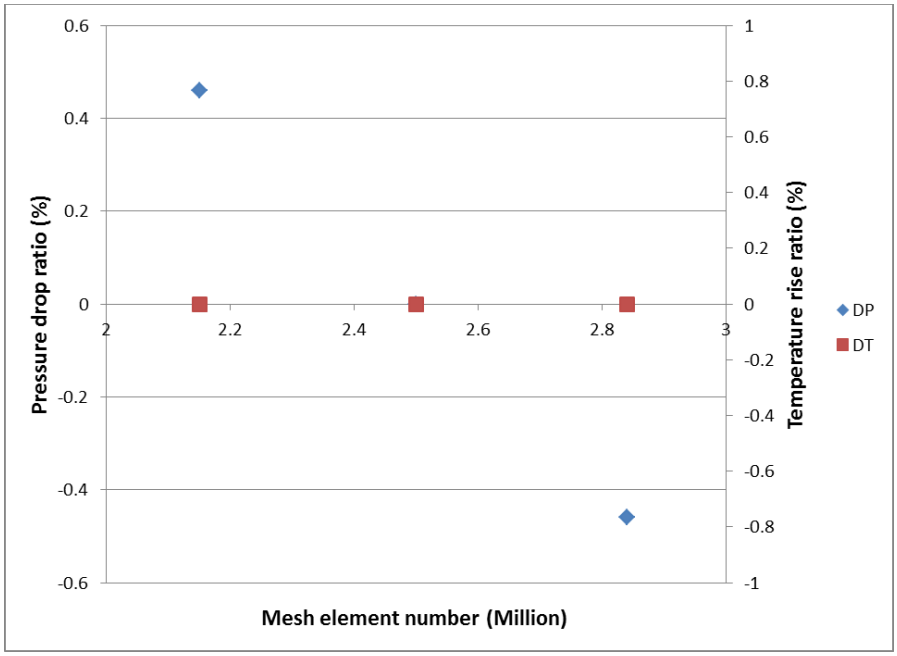

Figure 3-12 Pressure drop ratio change and temperature rise ratio change in grid independence study

3.4.2. Pump axial thrust control with POVs

In standard industrial applications, the clearance between the rib top and the pump casing is usually between 0.4 and 1 mm to maintain the best thrust control capacity. Because the studied CMP needs to handle the solid particles inside the fluid, it features a much larger vane top clearance.

Figure 3-13 depicts the first stage impeller, inlet casing, return channel. The impeller has three pump-out-vanes (POVs) installed. To further control the axial thrust, casing ribs used as vortex breakers are installed on the inlet casing to reduce the swirling flow. The effect of the casing ribs will be the studied in the future while this study will focus on the effect of the POVs.

Figure 3-13 The first stage pump impeller with POVs and the inlet casing and the return channel

Figure 3-14 presents the section view of the studied impeller with POVs. $R_{V\text{-}I}$ and $R_{V\text{-}O}$ are the inner and outer radius of the POV, respectively. H_V and δ are the POV height and the clearance between vane top and casing, respectively. The study includes 6 impeller models with different POV outlet diameter and axial vane height. Table 3-12

lists the POV details of the six models. Model 2 has the same dimension of POVs as the tested impeller. Model 1 has neither POVs nor casing ribs and the other five models have different POVs with the same casing ribs.

Table 3-12 POV dimensions of the 6 models

	Vane inlet radius RV_I (mm)	Vane outlet radius RV_O (mm)	Vane height HV (mm)	Axial clearance δ (mm)	Front casing ribs
Model 1	31	0	0	5.5	NO
Model 2	31	103	3	2.5	YES
Model 3	31	103	4.5	1	YES
Model 4	31	103	1.5	4	YES
Model 5	31	76	3	2.5	YES
Model 6	31	86	4.5	1	YES

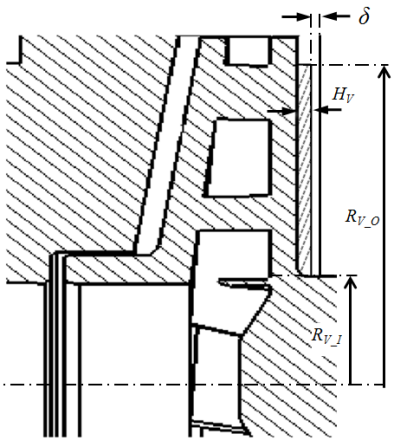

Figure 3-14 Section view of the impeller with POVs

In order to accurately evaluate the effects of POVs on the pump performance, the CFD models includes the main flow passages, the leakage channel between the first stage impeller and the leakage channel between impeller front shroud and pump inlet, as shown in Figure 3-15.

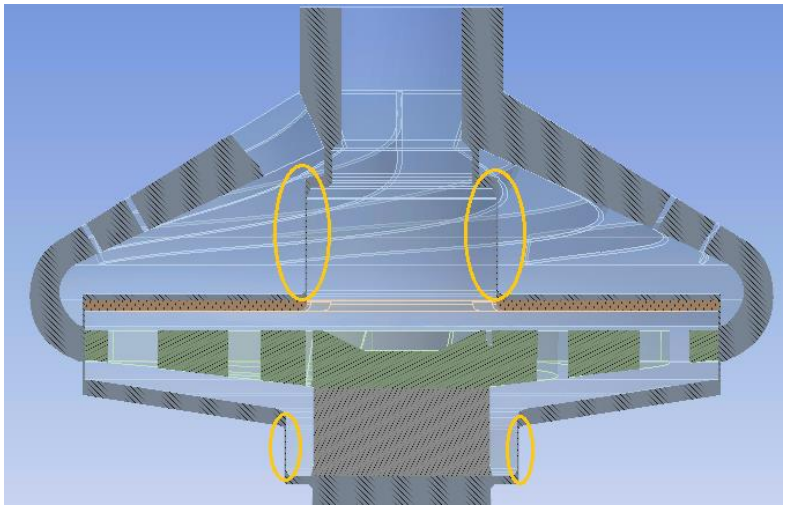

Figure 3-15 Section vies of the flow channel with leakage channel marked

A mesh independence study was carried out based on Model 2 evaluating five different meshes with different element numbers and first layer mesh heights. Table 3-13 and Figure 3-16 shows the meshing details results of the grid independence study, respectively. The pressure rise ratio changes are within 0.25% and the torque ratio changes are within 0.6%. The mesh with 8.43 million elements for Model 2 provides the best balance between accuracy and computational cost. Figure 3-17 shows the meshed model including a section view.

Table 3-13 Mesh details in grid independence study

Mesh	Number of elements (Million)	Number of nodes
Mesh-1	8.43	3062665
Mesh-2	10.55	3874508
Mesh-3	13.90	5173224
Mesh-4	29448620	9608518
Mesh-5	33973489	11074994

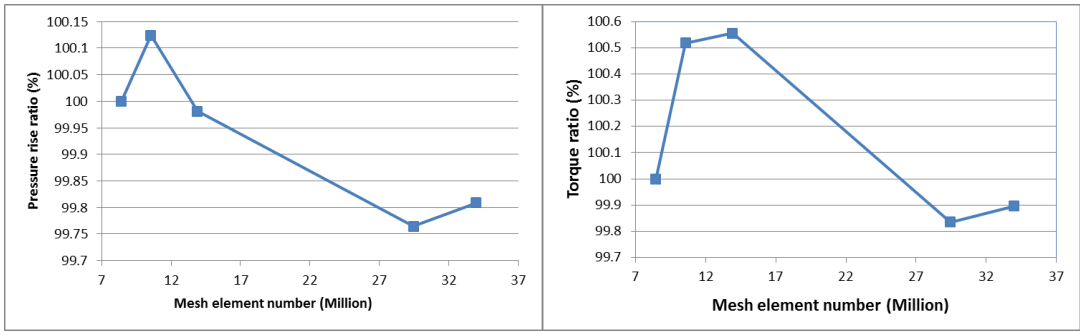

Figure 3-16 Meshing independence study results

Since all the models share the similar flow passage and flow conditions, it is reasonable to apply the same mesh setting for Model 2 to others models without further grid independence study. The simulation model includes both the front and rear leakage passages. Since much smaller element sizes are required with these small channels included in the geometry, the resulting mesh size significantly increased for other models.

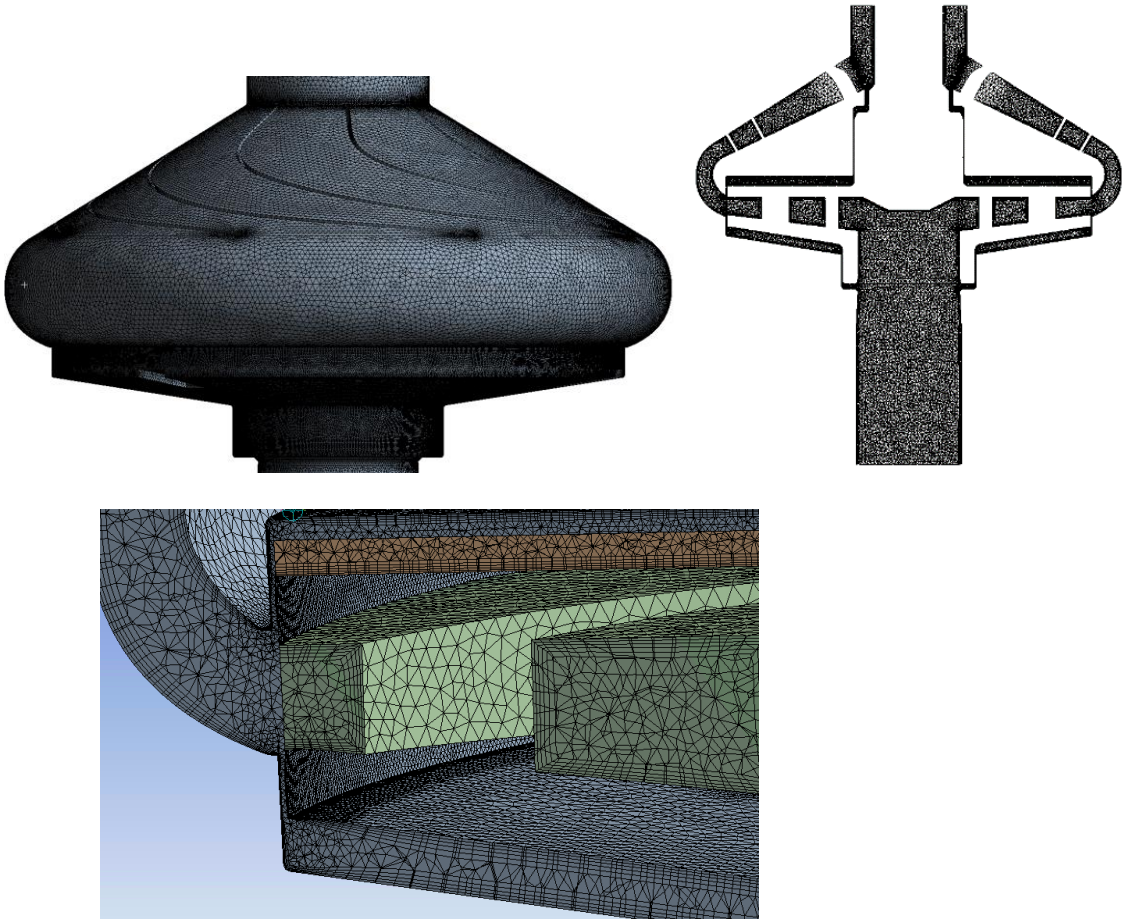

Figure 3-17 Mesh of pump first stage flow channel assembly

For each model, the simulation includes varying flow rates at different pump running speeds. Table 3-14 shows the simulation runing matrix. The CFD simulation models the flow a single phase sinse the centrifugal pump stages are not designed to handle two-phase flow and there is no air in the pump inlet during the test.

Table 3-14 CFD simulation boundary conditions

Pump running speed (RPM)	Inlet flow rate (GPM)	Outlet pressure (Psi)
2000	50	53
	75	53
	100	53
3000	75	87
	100	87
	150	87
3700	100	120
	150	120
	190	120

4. RESULTS AND DISCUSSIONS

This chapter includes two sections describing experimental test results and CFD simulation results.

4.1. Experimental test results

This section covers the performance of the two-stage CMP, including the Venturi calibration test, oil baseline test, pump thermal run test and pump multiphase test.

4.1.1. Venturi calibration test

The Venturi calibration test creates the correlations between the Venturi channel pressure drop and the CMP jacket flow rate. These correlations allow the calculation of the motor recirculation flow rate in the subsequent pump performance test. Because the pump is installed vertically, the elevation difference between the Venturi channel inlet and outlet generates a static pressure difference and all the Venturi channel pressure drop data are corrected with this value.

The GVF of the Venturi calibration test is calculated by the following equation:

$$\mathrm{GVF} = \frac{\mathrm{Q_{air}}}{\mathrm{Q_{air}} + \mathrm{Q_{stator\ jacket}}} \times 100\% \tag{4.1}$$

The GVF of the pump performance test is calculated by the following equation:

$$GVF = \frac{Q_{air}}{Q_{air} + Q_{oil\ flowmeter}} \times 100\% \tag{4.2}$$

Q_{air} is the actual air flow rate at the position of air injection, $Q_{stator\ jacket}$ is the stator jacket flow rate and $Q_{oil\ flowmeter}$ is the oil inlet flow rate measured by the flow meter. Since the Coriolis flow meter provides air flow rate at the standard condition, the actual air flow rate is calculated from the following equation:

$$Q_{air} = Q_{airflowmeter} \frac{P_{standard}}{P_{actual}} \frac{T_{actual}}{T_{standard}} \quad 4.3$$

Where $Q_{airflowmeter}$ is the flow rate in SCFM (Standard Cubic Feet per Minute). Q_{air} is the flow rate in ACFM (Actual Cubic Feet per Minute). $P_{standard}$ is 14.7 Psi. $T_{standard}$ is 60 ^{o}F. P_{actual} is the absolute pressure at the air injection position. T_{actual} is the air temperature at the injection position. The effect of air humidity is minor factor and is not considered in the air flow rate conversion.

For a normal Venturi flow meter, the flow rate is a function of the pressure drop with a power of 0.5. The power functions between the corrected pressure drops and the jacket flow rates have the power ranging from 0.48 to 0.52. Figure 4-1 shows the calibration result plots and the generated correlations.

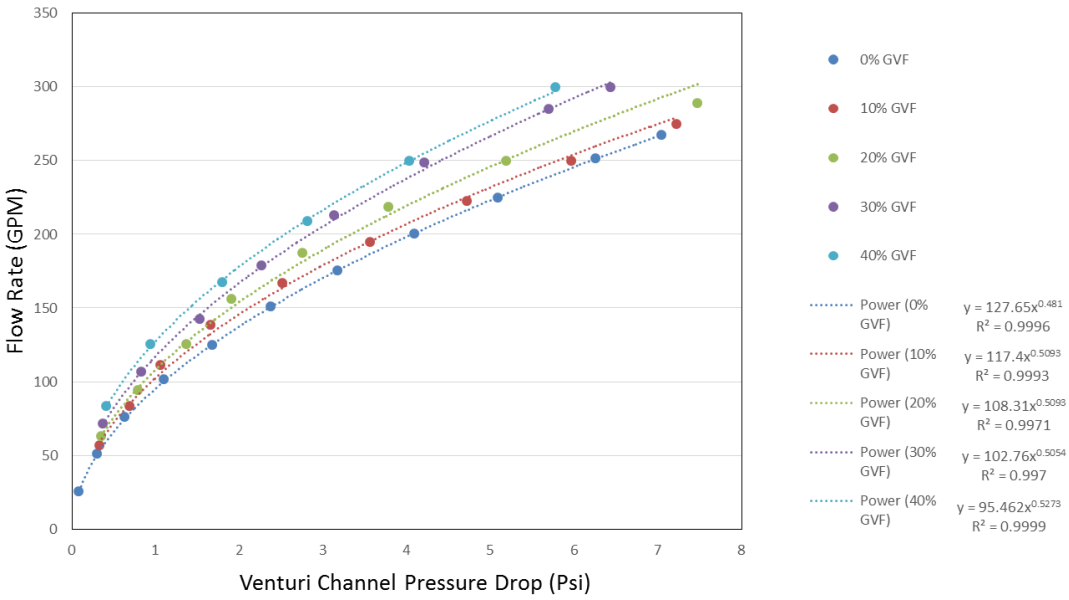

Figure 4-1 Venturi channel pressure drop vs jacket flowrate

4.1.2. CMP oil baseline performance test

In the experimental test, the inlet pressure is above the NPSH to avoid cavitation. The low flow rate limit choice is not based on pump surging, but on minimum motor cooling flow requirement. The selected test flow range provides sufficient margins to avoid stall and stonewall. Figure 4-2 and Figure 4-3 show the head rises and power consumption changes at different flow rates and speeds, respectively. At the same speed, the pump head decreases with the increasing flow rate. At the same flow rate, the higher the speed, the higher the pump head. The power consumption increases with the increasing flow rate and pump head.

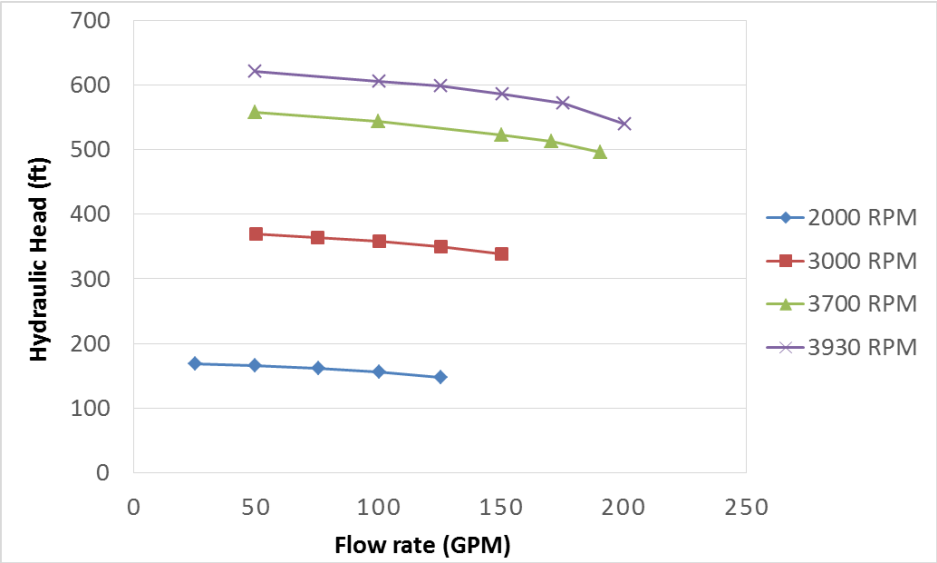

Figure 4-2 CMP head rises at different running speeds

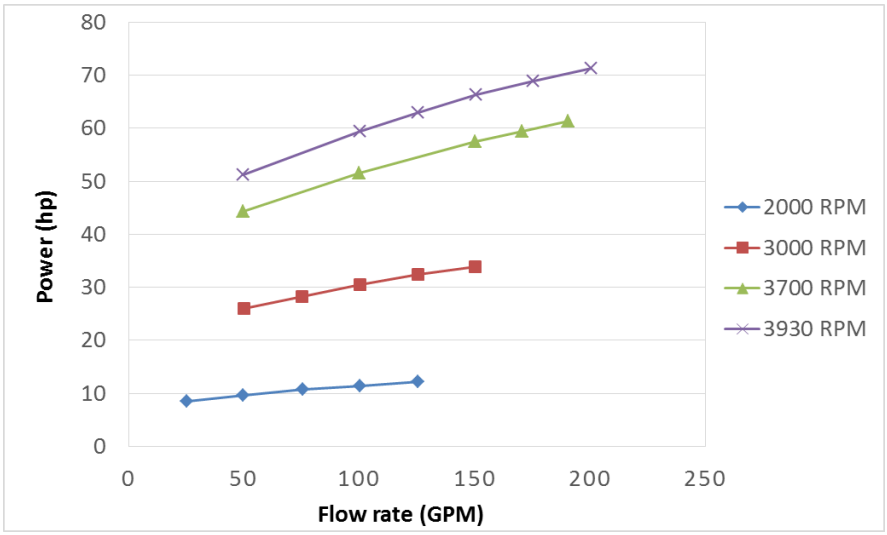

Figure 4-3 CMP power consumptions at different running speeds

Pump efficiency is defined as:

$$\eta = \frac{Q_{oil} Head}{P_{motor}} \times 100\% \qquad 4.4$$

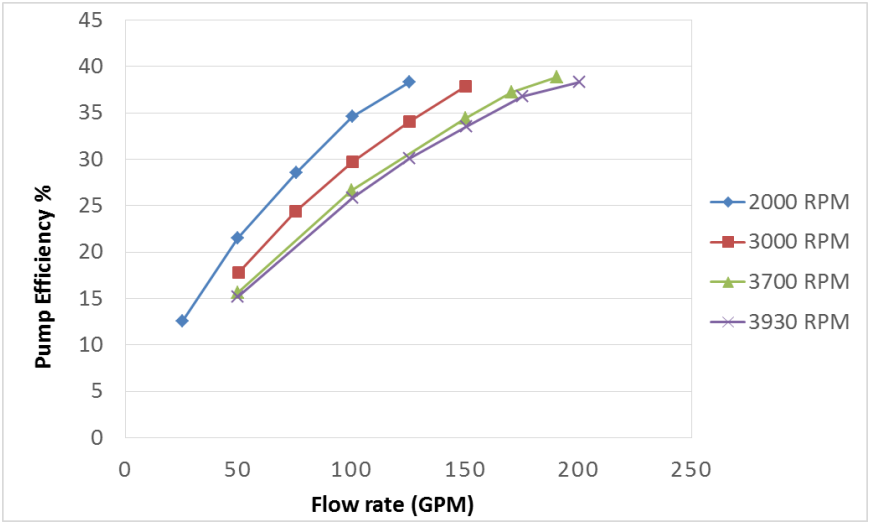

Figure 4-4 Pump efficiency at different running speeds

Figure 4-4 shows the pump efficiency at different conditions. For a given speed, the pump efficiency increases as the flow rate increases. The overall pump efficiency is

lower than a normal centrifugal pump since CMP designs for nuclear waste liquid applications prioritize reliability over efficiency. Part of the loss is due to the high friction losses from the rotating thrust bearing surfaces and immersed motor rotor surfaces. Another significant loss arises from the internal recirculation flow that cools the motor.

Figure 4-5 shows the changes of internal recirculation flow rate in the oil baseline test and Figure 4-6 presents the thrust cavity relative pressure variation. For a given speed, the thrust cavity relative pressure increases with the pump inlet flow and the higher thrust cavity pressure drives more recirculation flow. Furthermore, the recirculation flow rates are higher at high flow rate conditions but the ratio to the inlet flow rate is lower. At 50 GPM, the recirculation flow reaches up to 50% of the inlet flow rate and even at 200 GPM, the recirculation flow ratio is still over 20%. The high recirculation flow ratio reduces the pump efficiency further at partial load condition.

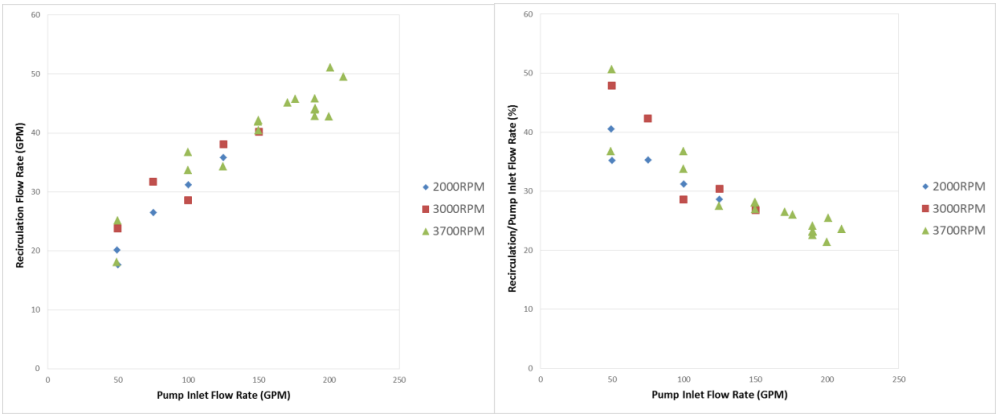

(a) (b)

Figure 4-5 (a) Internal recirculation flow rate in oil baseline test (b) Internal recirculation flow to pump inlet flow ratio in oil baseline test

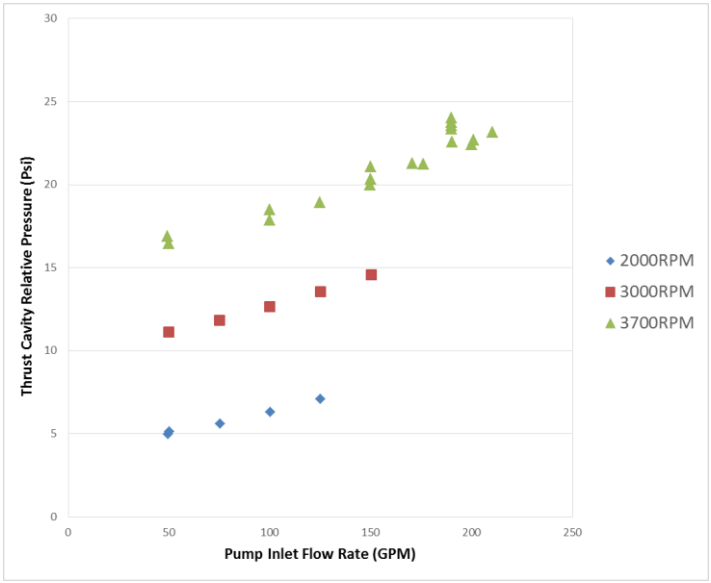

Figure 4-6 Thrust cavity relative pressure changes in oil baseline test

4.1.3. CMP oil-air two-phase flow performance test

The two-phase flow performance tests include gas injection after the second pump stage only affecting the downstream flow passages around the motor. The maximum GVF is limited to 20% in order to prevent failures of the process liquid-lubricated thrust bearing. Figure 4-7 shows the CMP head performance under different running speeds and GVFs. Figure 4-8 shows the pump efficiency at different working conditions. The change of GVF has little effect on pump hydraulic head because, as mentioned before, the air was injected after the impeller. As the GVF increases, more air enters the recirculation channel reducing the overall fluid viscosity of the oil-mixture and, consequently, reducing the power requirement to overcome the friction on the rotor.

In this case, since the motor input voltage is constant, the motor current input decreases, as shown in Figure 4-9.

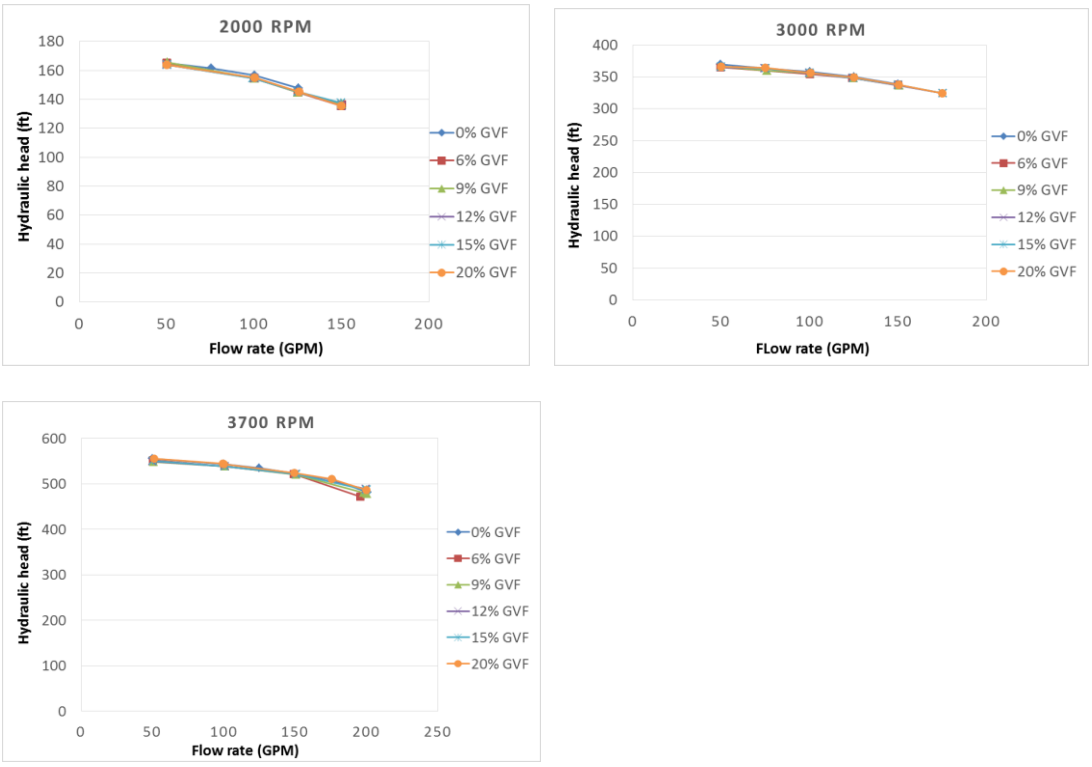

Figure 4-7 Pump head rise at different running speed and different GVFs

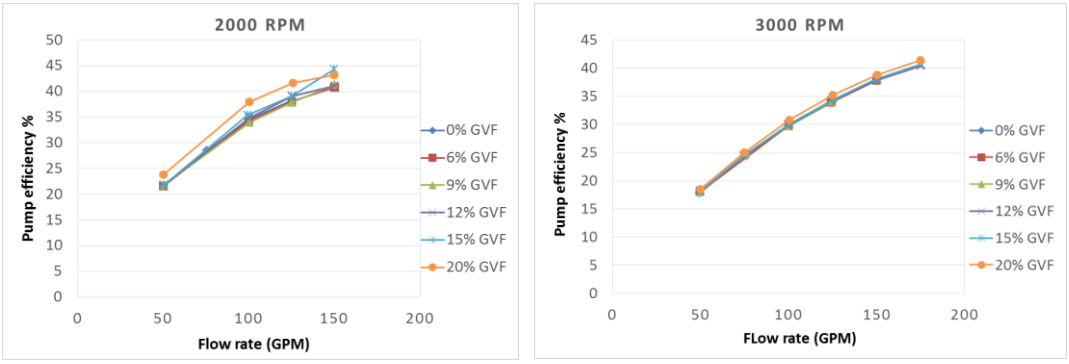

Figure 4-8 Pump efficiency performance at different running speed and GVFs

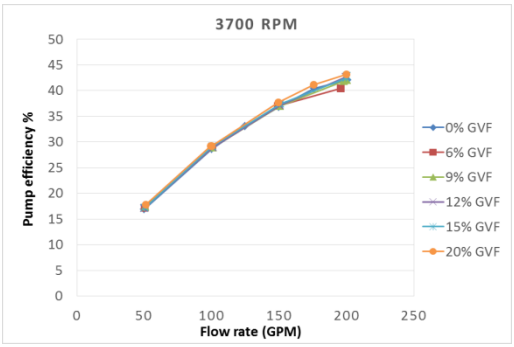

Figure 4-8 Continued

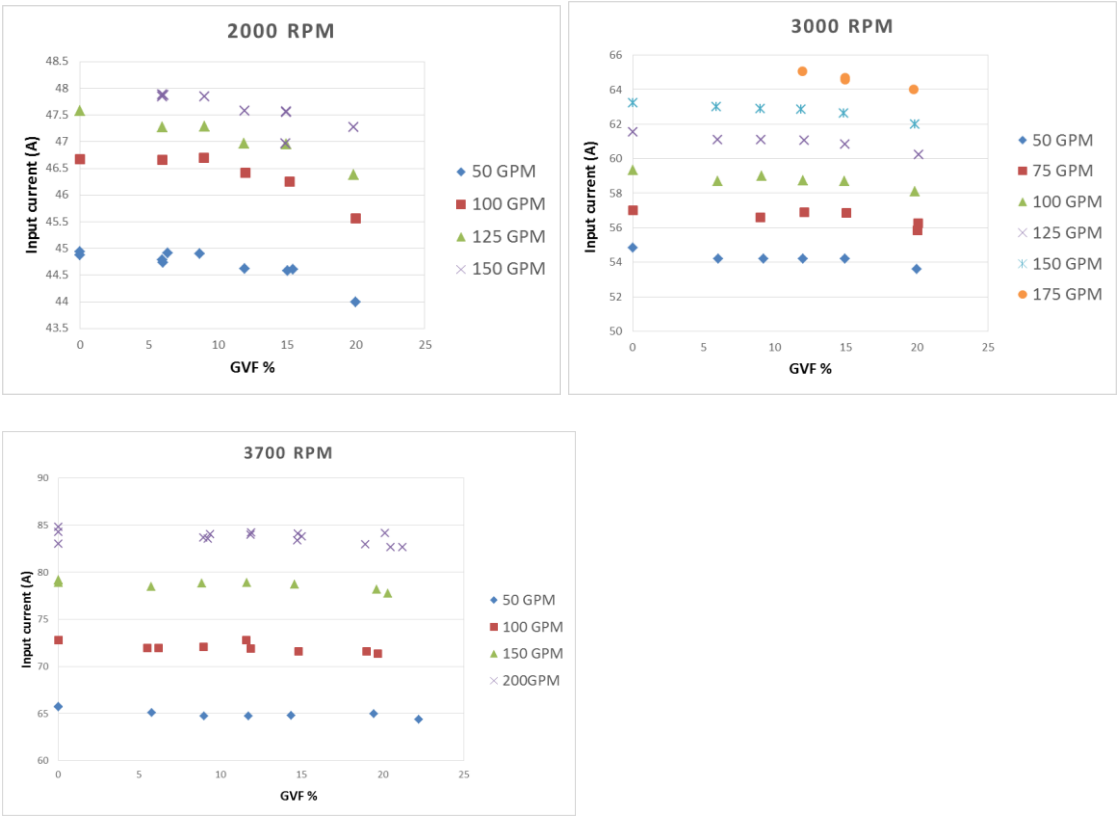

Figure 4-9 Pump input current changes at different running conditions

4.1.4. Pump thermal run test

For an air-cooled motor, when the motor stops, the attached cooling fan stops working and the forced heat convection cooling the motor also stops. In a short period of time after the motor stops, the motor stator and rotor temperatures can reach even higher temperatures than those experienced during motor operation. In the CMP thermal run test, the pump starts at ambient temperature and is operated at a constant speed until all the temperature sensors become stable. Then the pump stops and the computer will continue monitor and record the temperatures until it starts decreasing.

The steady state thermal run test is required to evaluate pump thermal performance at both single-phase flow conditions and two-phase flow conditions. The maximum motor temperature should be under 428^{o}F in both tests.

Figure 4-10 shows the temperature change during pump single-phase thermal run test at 3930 RPM, 200 GPM. The motor reached the thermal steady state in about an hour. The highest temperature observed in the test was 310^{o}F and it was below the maximum temperature limit. Because the motor was immersed in the liquid, it did not show an apparent temperature jump after the motor stopped.

Another test evaluated the motor thermal performance under two-phase flow conditions. The CMP ran at 3700 RPM, 150 GPM with varying GVF. Figure 4-11 shows the motor temperature changes with time and GVF. All the motor temperature sensors are below the maximum temperature limit at all the running conditions. The single-phase flow test was relatively easy to control, but the two-phase flow test was very complex. Compared with the oil baseline thermal run test, there are more variables affecting the

motor temperature and Figure 4-11 alone cannot provide enough information to diagnose motor temperature changes. Figure 4-12 shows the changes of motor temperature sensor 1, the pump oil inlet temperature, the motor power input and the GVFs during the two-phase flow thermal run test. The system became unstable and the oil flow rate was no longer constant after the air was injected. The inlet oil temperature increased because the air-fan heat exchanger could not provide enough cooling. As the ambient room temperature increased during the test, the air temperature from the air compressor also rose up and the inlet air temperature at the CMP air inject holes also increased.

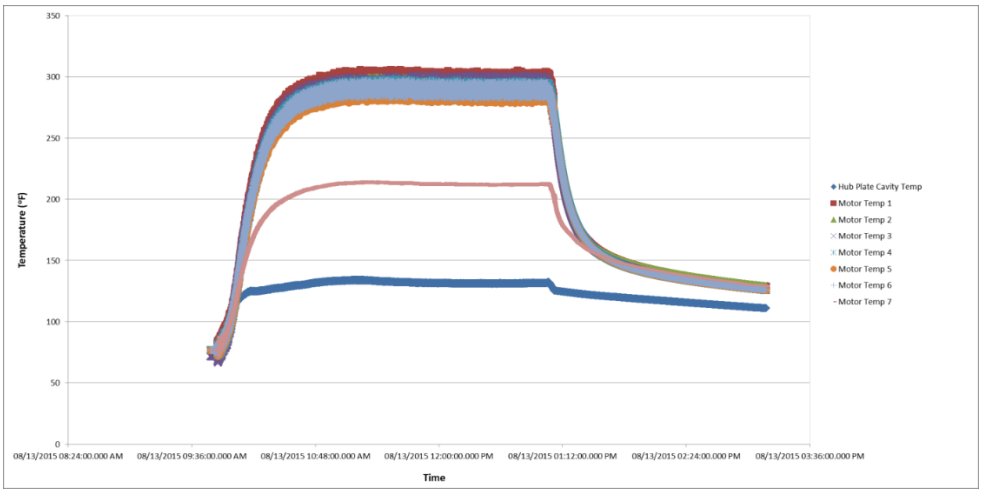

Figure 4-10 Pump thermal steady running test at 3930 RPM, 200 GPM, 0% GVF

The pump thermal running test proved that the CMP can work under two-phase flow conditions without thermal problems. But it is not clear if the reduced recirculation flow rate will significantly increase the motor temperature, especially when air is presented in the flow. CFD simulations will address this concern.

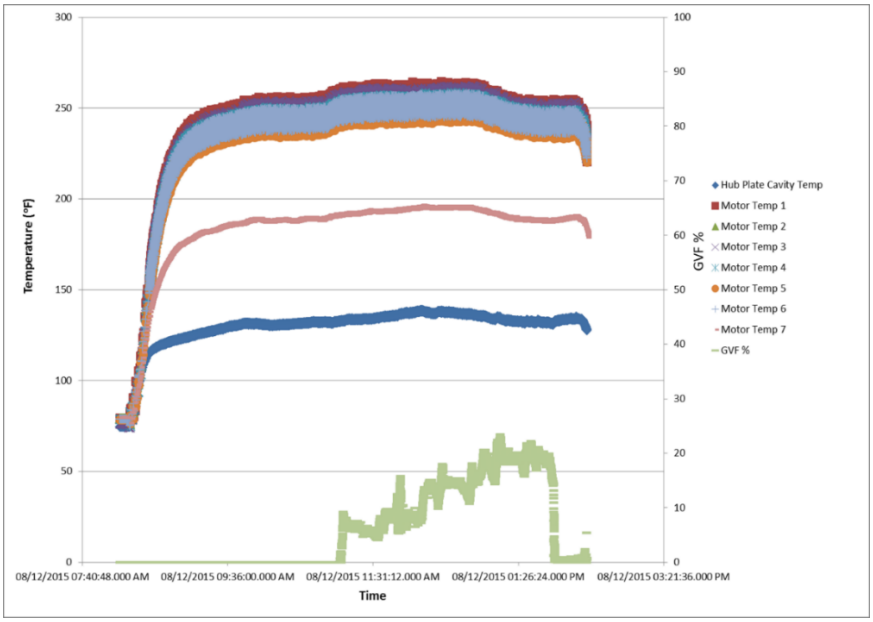

Figure 4-11 Pump thermal steady running test at 3700 RPM, 150 GPM, and varying GVFs

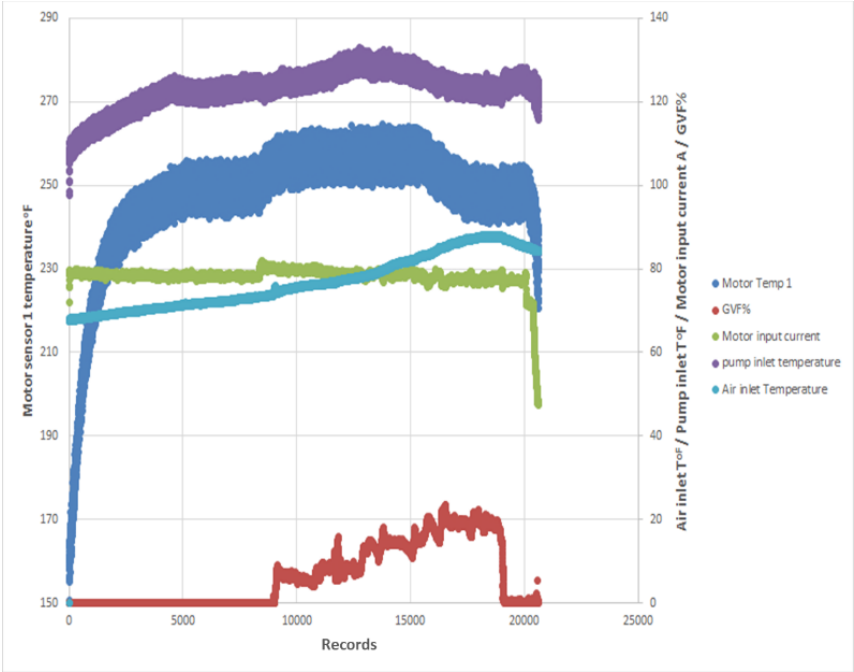

Figure 4-12 Changes of motor temperature sensor 1, the pump oil inlet temperature, the motor power input and the GVFs during the two-phase flow thermal run test

4.1.5. CMP axial thrust analysis

Figure 4-13 shows the pump axial thrust changes at different flow rates and GVFs. The upward thrust is defined as positive and the downward thrust in gravity direction is defined negative. For a given speed, the outlet pressure increases as the flow rate reduces and results in an increase in the impeller backface clearance pressure. Since the impeller shroud clearance pressure is almost constant, the axial thrust increases in the direction of gravity. For the same reason, when air is injected in the stator jacket annulus, the pump outlet pressure increases and the axial thrust increases in the direction of gravity. The outlet pressure increases with GVF, and thus the gravity-direction axial thrust grows with increasing GVF.

The pump thrust limit is -1000 lbf. The experimental data shows the thrust is under this limit except at some low flow rate combined with high GVF at 3700 RPM.

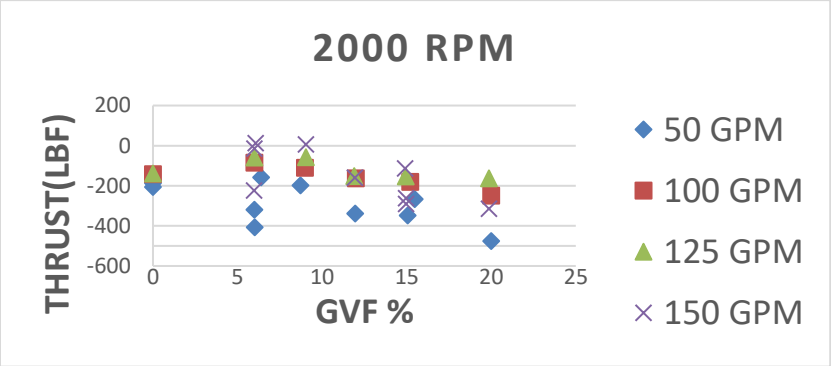

Figure 4-13 CMP axial thrust changes in different conditions

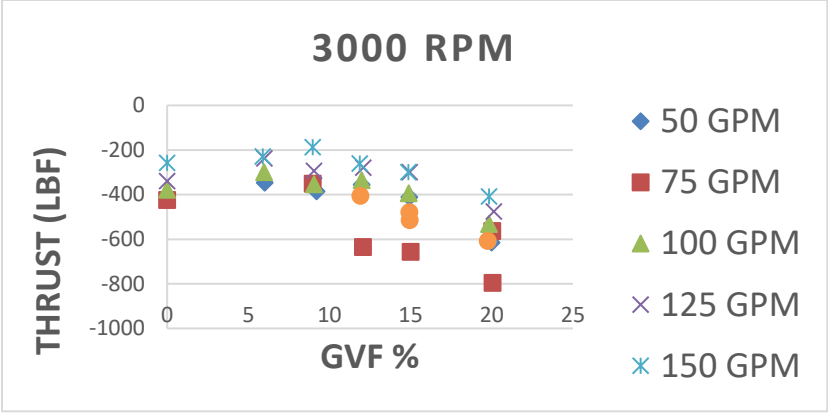

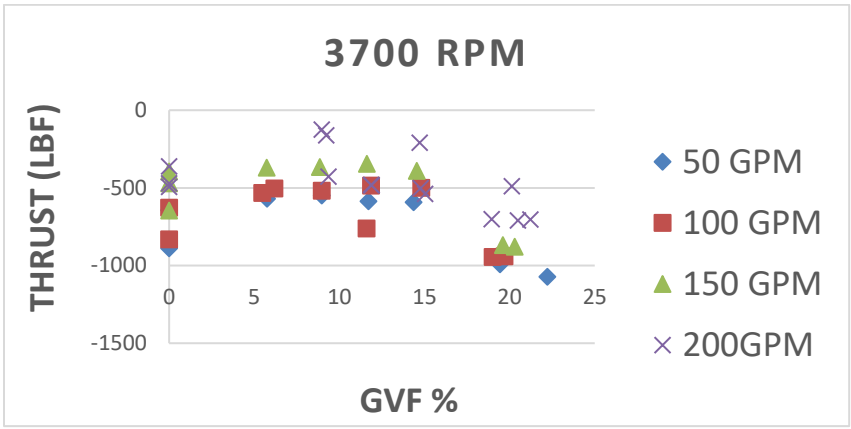

Figure 4-13 Continued

4.1.6. Pump impeller orbit analysis

Two perpendicularly installed proximity probes monitor the radial movement of the impeller during the test. Since the air was injected after the impellers, the GVF changes had little effect on the impeller orbits.

Figure 4-14 to Figure 4-19 present the processed orbit data for 0% GVF at different running speeds. The Fast Fourier Transform (FFT) plot shows one low frequency signal at 1/10 of the pump running speed, a synchronous component and another component three times of running speed.

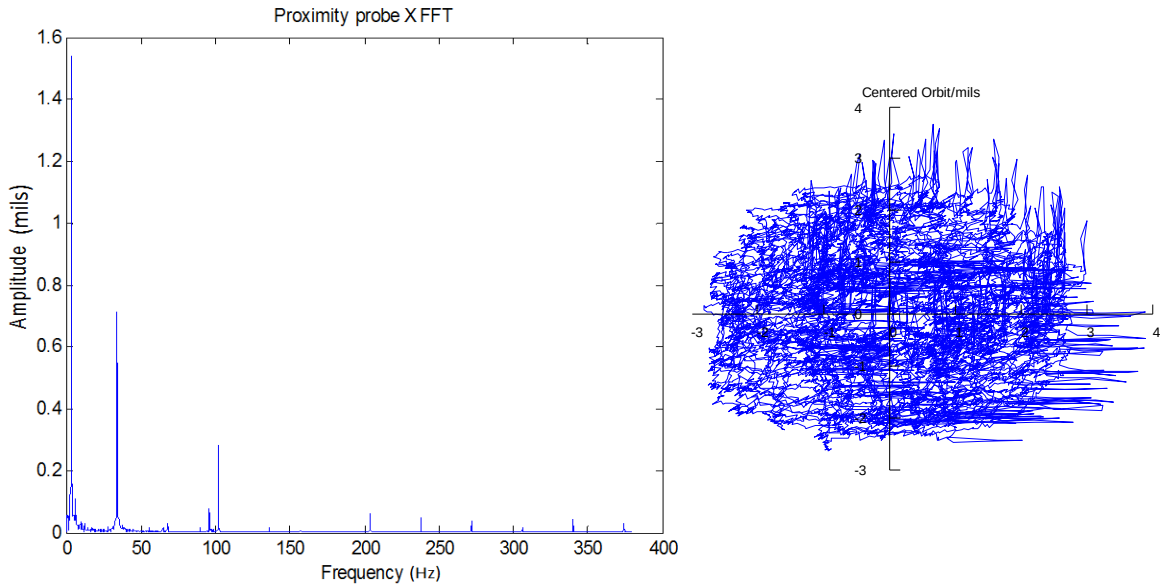

Figure 4-14 Impeller orbit and FFT spectrum plot for 2000 RPM 50 GPM 0% GVF

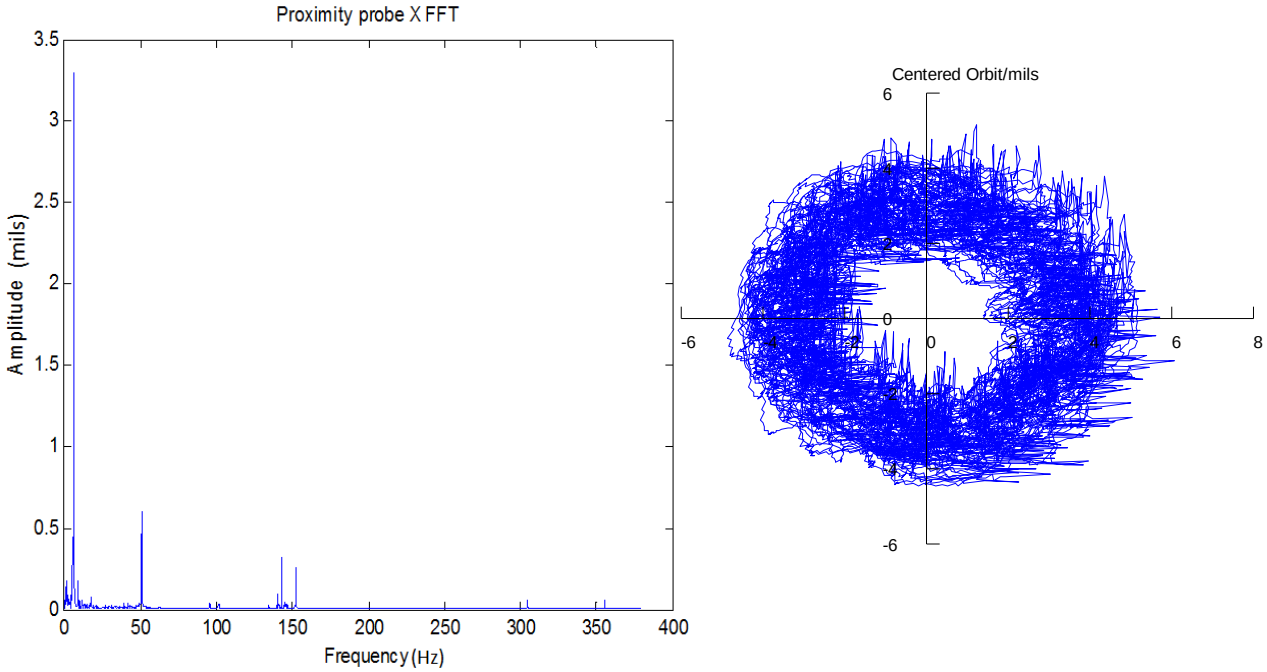

Figure 4-15 Impeller orbit and FFT spectrum plot for 3000 RPM 50 GPM 0% GVF

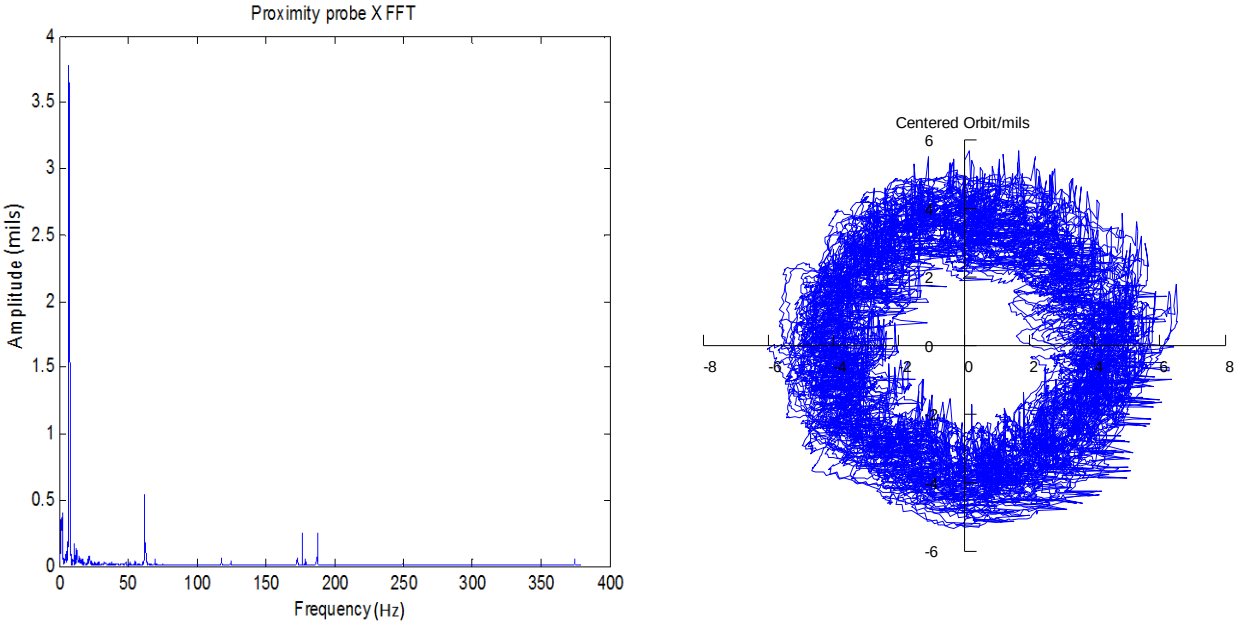

Figure 4-16 Impeller orbit and FFT spectrum plot for 3700 RPM 50 GPM 0% GVF

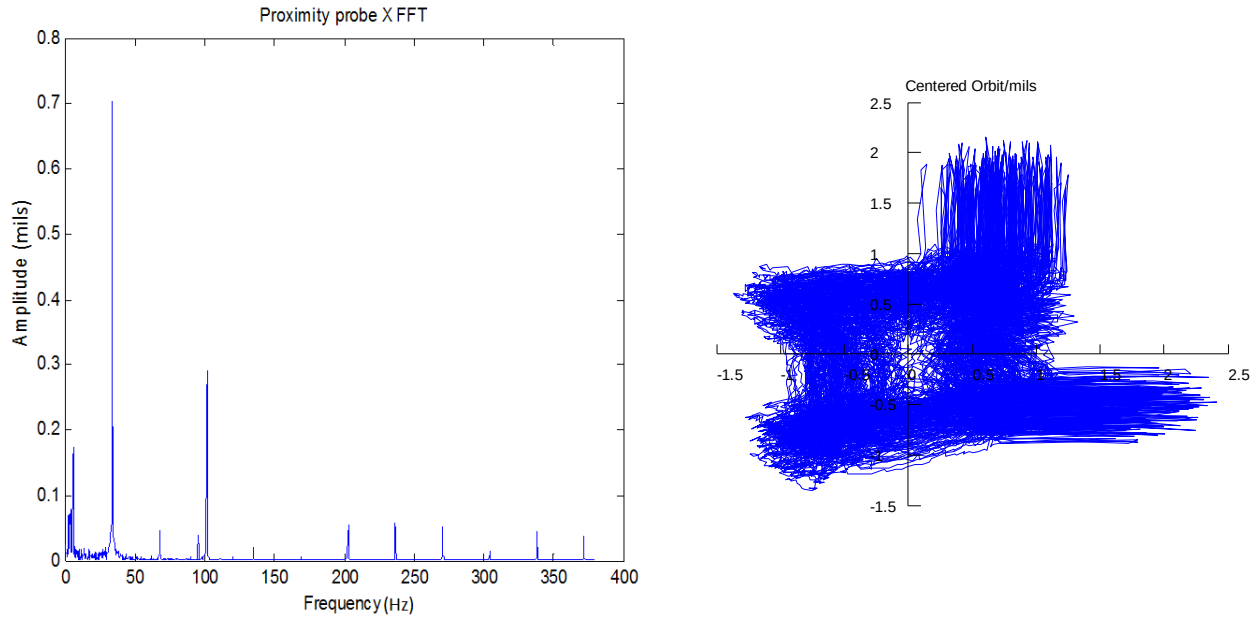

Figure 4-17 Impeller orbit and FFT spectrum plot for 2000 RPM 150 GPM 0% GVF

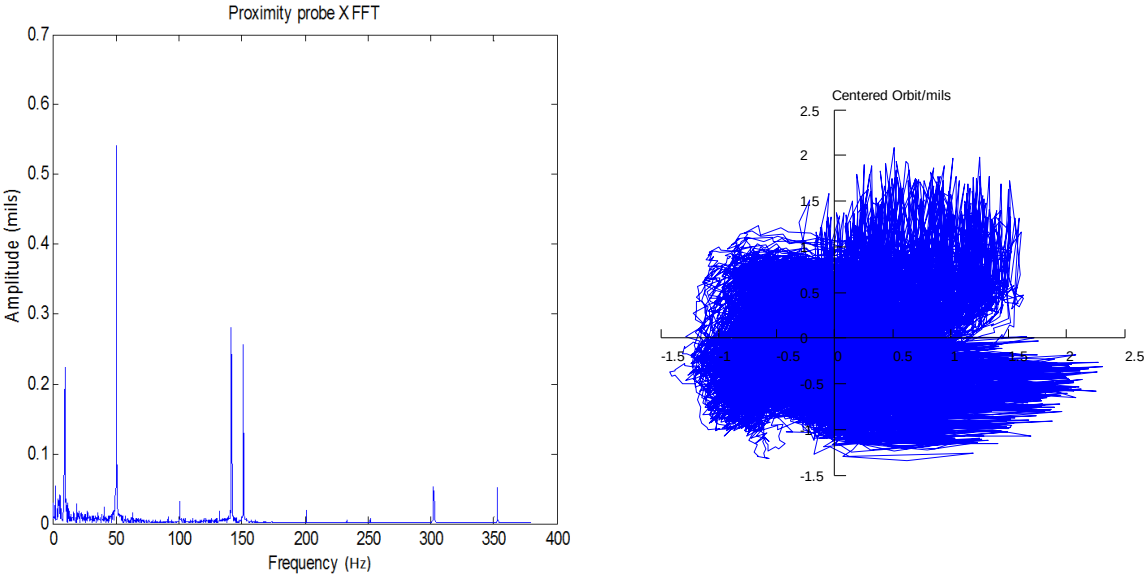

Figure 4-18 Impeller orbit and FFT spectrum plot for 3000 RPM 150 GPM 0% GVF

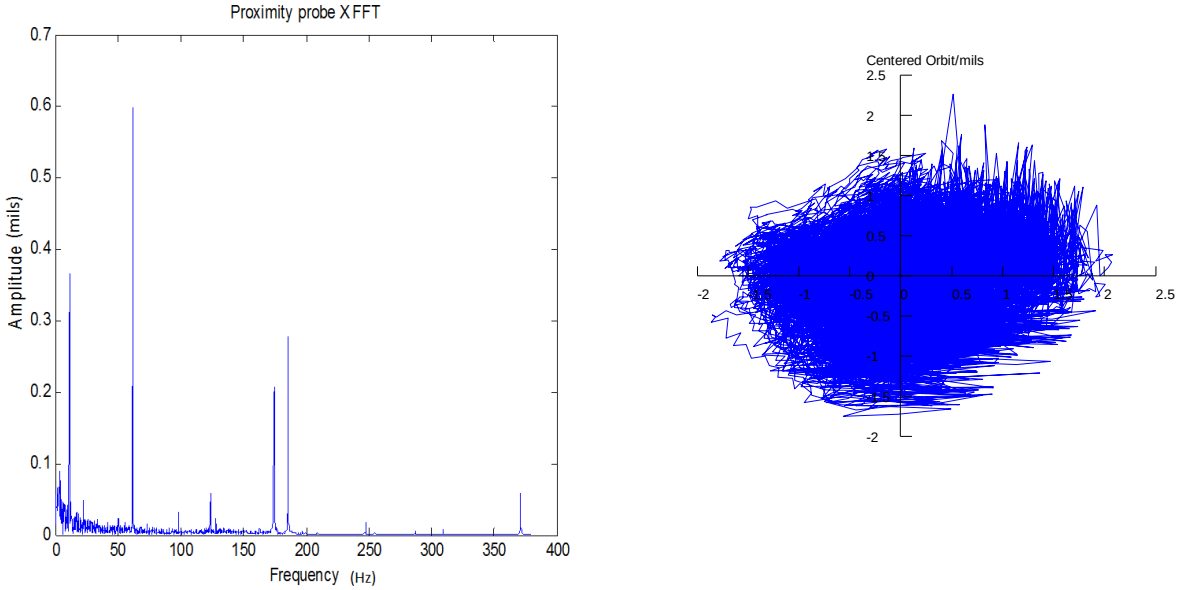

Figure 4-19 Impeller orbit and FFT spectrum plot for 3700 RPM 150 GPM 0% GVF

4.2. Recirculation channel heat transfer simulation

This section presents the simulation of heat transfer in the recirculation channel with different flow rates and GVFs.

Figure 4-20 shows the outer and inner wall temperature of the recirculation channel at 3700 RPM and 40 GPM flow rate corresponding to the single-phase oil flow simulation. The highest temperature of the outer wall occurs at the top cavity where the flow channel suddenly expands. Figure 4-21 shows section views of the temperature distribution and the velocity vector in the top cavity. When the inlet flow enters the top cavity, the flow slows down and forms a vortex near the outer cylinder wall. The low flow velocity in the cavity reduces the local heat convection resulting in a high wall temperature. The outer wall temperature at the bottom cavity is lower than the outer wall temperature at the top cavity. Figure 4-22 displays the flow field in the bottom cavity. The flow still has relatively high axial flow velocity after entering the bottom cavity until it reaches the horizontal wall. The high axial flow velocity benefits the outer wall heat transfer in the bottom cavity.

Due to the rotation of the inner wall, the near wall fluid has high tangential speed and the wall temperature depends more on the near wall fluid temperature. The fluid temperature increases along the axial flow direction and becomes relatively high when the fluid enters the bottom cavity. In the bottom cavity, the main stream of the flow moves along the outer wall and a small fraction of the main flow recirculates in the bottom cavity. The fluid recirculated in the bottom cavity is too small and the heated

fluid cannot smoothly leave the cavity, which results in the highest temperature of the inner wall.

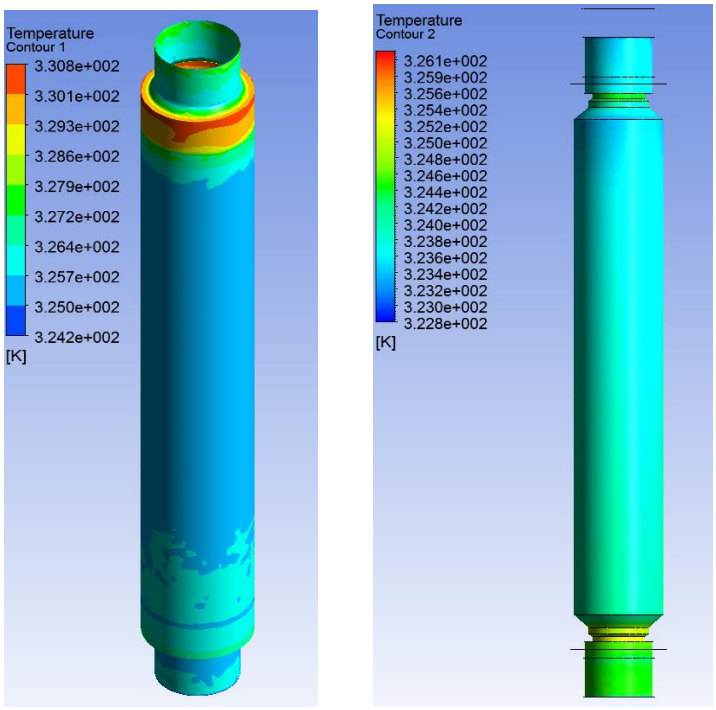

Figure 4-20 Recirculation channel outer and inner wall temperature (K)

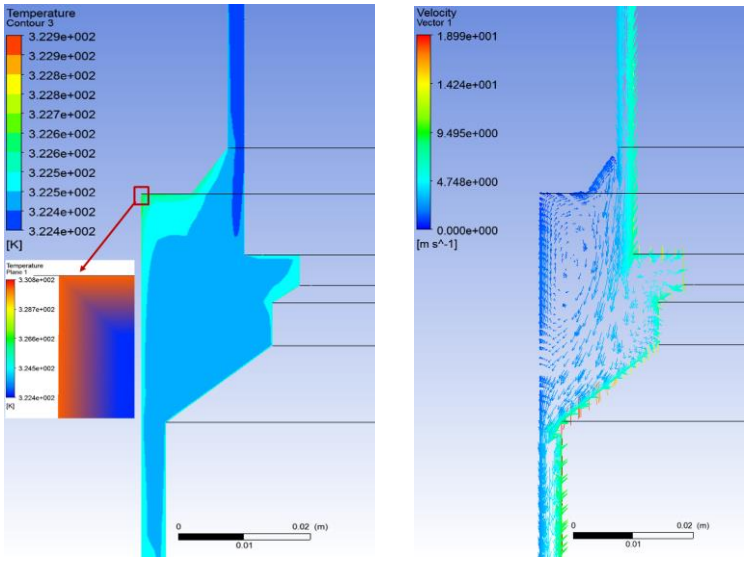

Figure 4-21 Temperature (K) and flow field (m/s) in top expansion cavity

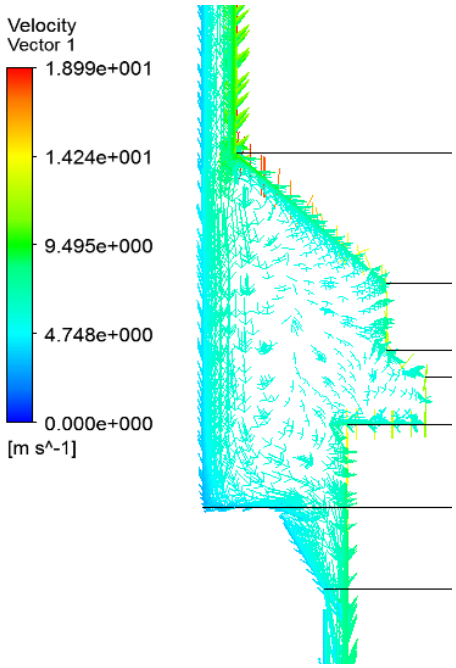

Figure 4-22 Flow field in the bottom expansion cavity

Tests with different flow rates (40 GPM, 30 GPM and 20 GPM) aimed at evaluating the effect of reduced recirculation flow on the heat transfer efficiency. The heat transfer analysis will focus on the outer wall of the recirculation channel since the stator and winding temperature are the critical parameters. Figure 4-23 presents the temperature changes along the outer wall at different flow rates.

In the zone “A”, the temperature is highest at 20 GPM and lowest at 40 GPM. The Nusselt number in this zone is highly influenced by the axial fluid velocity. The high axial flow velocity increases the Nusselt number and improves the heat transfer process. In zone “B”, the wall temperature is mainly affected by the recirculation flow in the local cavity. The peak temperature is almost the same at 30 GPM and 40 GPM while it is lower at 20 GPM. Figure 4-24 shows the streamlines in the top cavity at different

flow rates. The extra small vortex in the cavity at 20 GPM enables better heat transfer compared with the situation at 30 GPM and 40 GPM.

The peak temperature changes caused by the varying flow rates are small. There is no evident of temperature variation after reducing the recirculation flow rate by 50%.

Air entering the recirculation flow reduces the overall liquid heat capacity and cooling effectiveness. **Error! Reference source not found.** Figure 4-25 shows the outer wall temperature change at 40 GPM and 20 GPM with 10% GVF and 20% GVF. The results indicate that the flow rate dominates the overall temperature change and the reduced flow rate increases the wall temperature. At the same flow rate, high GVF will further increase the local temperature.

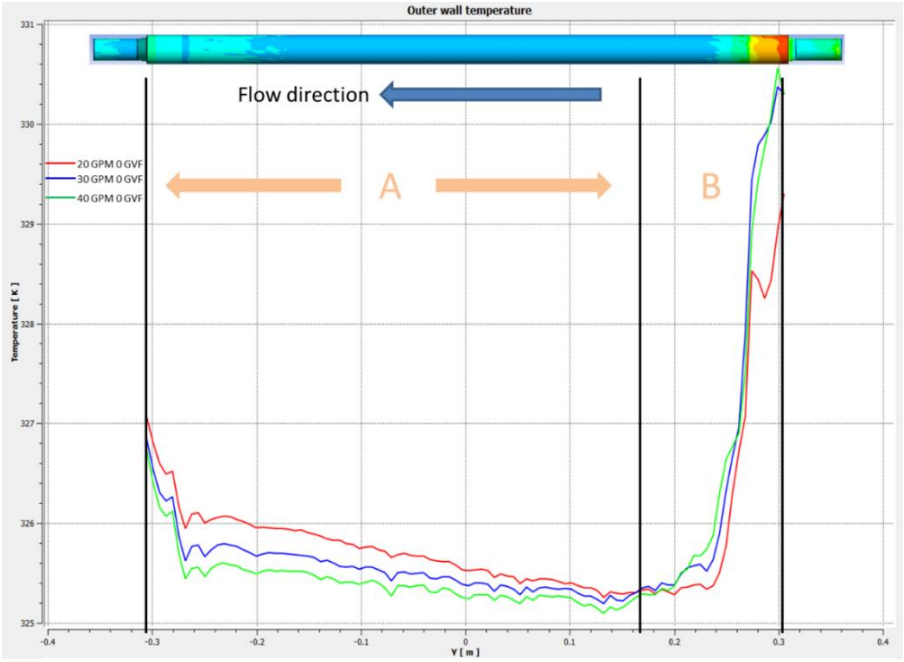

Figure 4-23 Temperature on recirculation channel outer wall at different flow rates

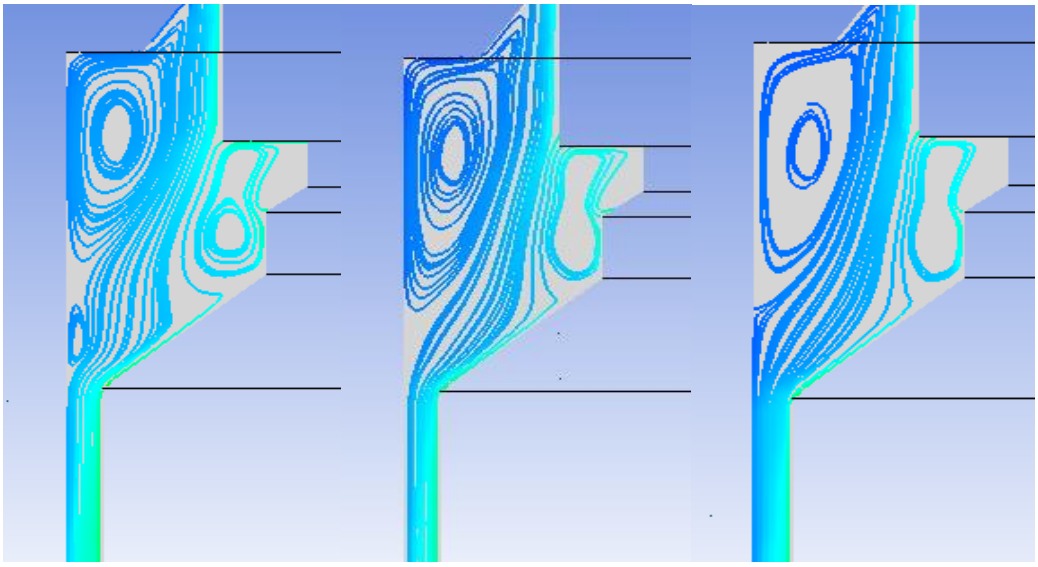

(a) (b) (c)

Figure 4-24 Local streamline at different flow rate (a) 20 GPM (b) 30 GPM (c) 40 GPM

Comparison of Figure 4-24 and Figure 4-25 indicate that the difference between the peak temperatures in zone “A” and zone “B” reduces when air enters the flow. The increase of peak temperature in zone “B” is higher than the rise in zone “A”.

Figure 4-26 shows the air volume fraction of 10% and 20% GVF at 40 GPM. The bottom cavity shows high air concentration in the recirculation channel. The outer wall temperature at 20% GVF is higher than one at 10% GVF because of the higher concentration of air in the bottom zone. Due to centrifugal effect from the rotation of the inner surface, air shows high concentration near the inner wall, which reduces the viscous friction exerted on rotation. Therefore, the pump efficiency slightly increases in the experimental results when GVF rises.

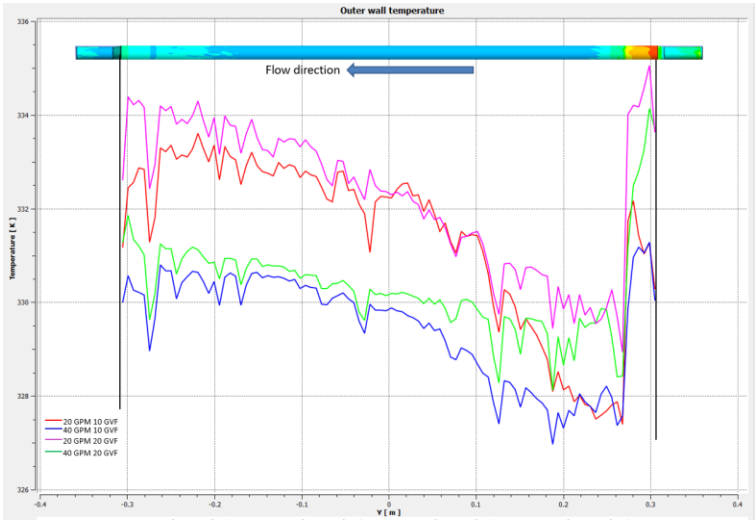

Figure 4-25 Temperatures on recirculation channel outer wall at different flow rates and GVFs

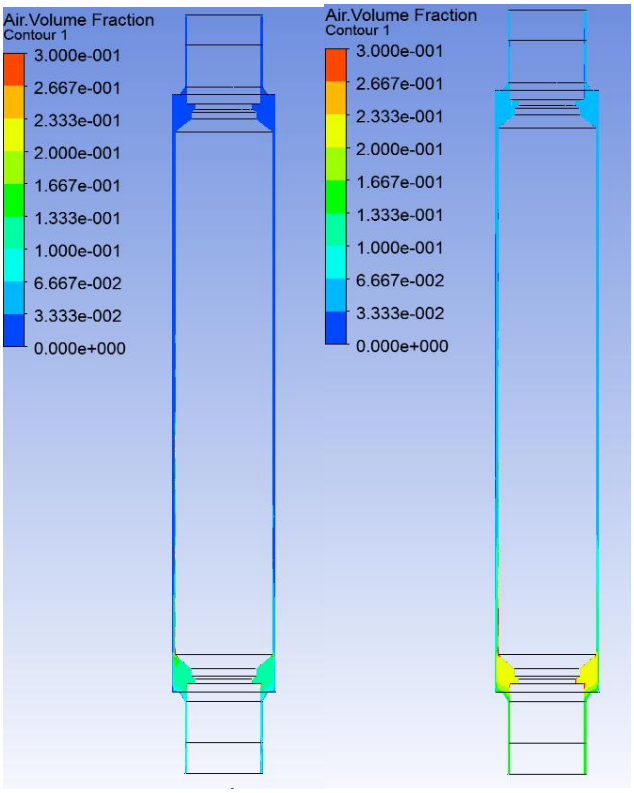

(a) (b)

Figure 4-26 Air volume fraction of 10% GVF (a) and 20% GVF (b) at 40 GPM

Figure 4-27 shows a simplified thermal resistance circuit and serves to evaluate the recirculation channel outer wall temperature effects on the motor components temperatures. The heat transfer process is simplified to a 1D model; a uniform heat source located in the middle of the motor with radial heat transfer. When the recirculation flow rate reduces, the thermal resistance R_{RE} increases and the recirculation flow temperature increases from T_{RE} to T'_{RE}. With constant power input in the middle component, the increase in R_{RE} will reduce the heat flux to the recirculation flow side. Ignoring the thermal conductivities changes of the components, a new temperature profile is defined as T'_{JK}-T'_{RE}. The largest temperature change between the two profiles can only be (T'_{wall}- T_{wall}) or (T'_{peak}- T'_{shift}). Based on the 1D heat transfer analysis, the maximum temperature change will be on the wall between R_2 and R_3, while maximum temperature change in R_3 is on the recirculation cylinder outer wall. Thus, the outer wall maximum temperature change is an adequate indicator of the motor maximum components inner temperature change.

Figure 4-28 (a) shows CFD results of the wall temperature change along the main outer surface when the working condition shifts from 40 GPM 0 GVF to 40 GPM 10% GVF. Figure 4-28 (b) shows the recorded motor sensor temperature changes from 40 GPM-0 GVF to 40 GPM-10% GVF in the test. The maximum temperature change in the CFD simulation is comparable to the average motor sensor temperature change in the experimental test. Therefore, the CFD simulation outer wall temperature can track the motor temperature changes when the recirculation flow conditions change.

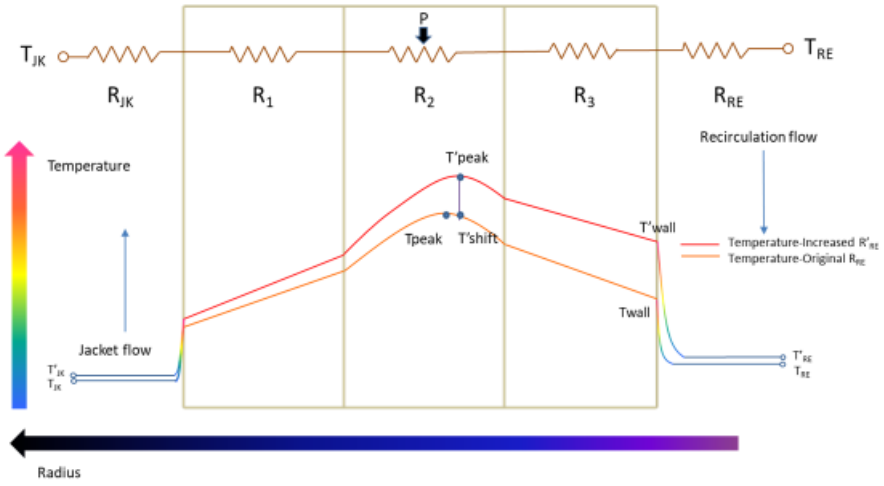

Figure 4-27 Simplified motor cooling thermal resistance circuit

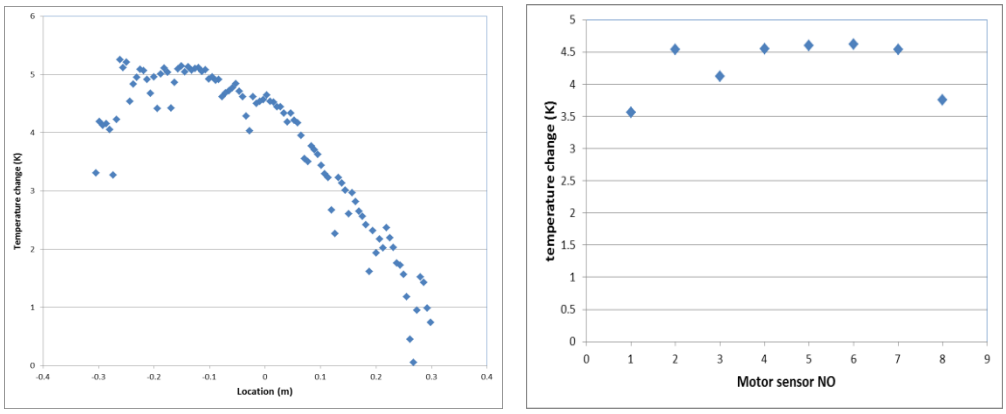

(a) (b)

Figure 4-28 Comparison of (a) CFD simulation wall temperature changes along the wall and (b) experimental motor sensor temperature change from 40 GPM 0 GVF to 40 GPM 10% GVF

Comparing Figure 4-23and Figure 4-25, the highest temperature change along the outer wall is between the 40 GPM single-phase flow and the 20 GPM, 20 GVF two-phase flow, and the highest temperature increase is about 9K, or 16.1^{o}F. Therefore, this

will be the highest expected temperature rise if the recirculation flow changes from 40 GMP single-phase flow to the 20 GPM, 20 GVF two-phase flow at 3700 RPM. The current experimental test results show that the peak motor temperature is 130^{o}F below the maximum allowable at 3700 RPM, and thus the motor temperature will still be under the temperature limit even the recirculation flow changes to the 20 GPM, 20 GVF two-phase flow. Pump efficiency increases as the recirculation flow rate decreases.

4.3. Pump thrust control simulation

Figure 4-29 shows the comparison of the pressure rise between the test results and the CFD simulation using Model 2, which is based on the first stage of the pump. The CFD simulation presents the same trend as that shown in the test data. The difference between CFD and test results is within 5%, thus validating the CFD model and methodology.

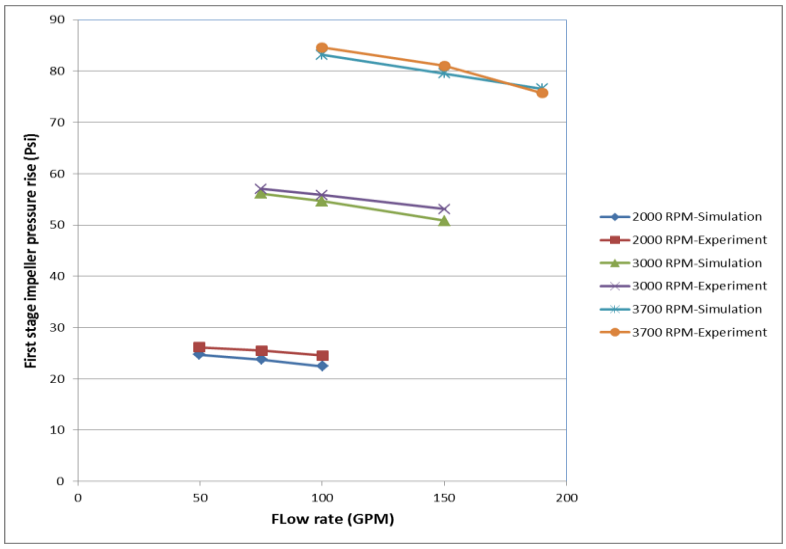

Figure 4-29 Pressure rise of first stage impeller: experiment vs. simulation

Figure 4-30 shows the pressure and velocity distribution at 3000 RPM, 100 GPM. The lowest pressure occurs at the bottom leakage channel. The bottom leakage channel width with a rotating inner surface is 0.5mm. When the flow enters the leakage channel, both the axial and tangential speed increases and thus the pressure drops. When the flow exits the leakage channel, it slows down and the pressure recovers.

Figure 4-31 shows the 3D and 2D streamline in the flow channel. In the front shroud clearance, the casing ribs disturbs the flow and the fluid tangential speed decreases. As the flow slows down, the pressure in the cavity increases. Figure 4-31 also shows the flow pre-rotation before it enters the impeller eye. The leakage flow and flow pre-rotation reduce the pump efficiency[46].

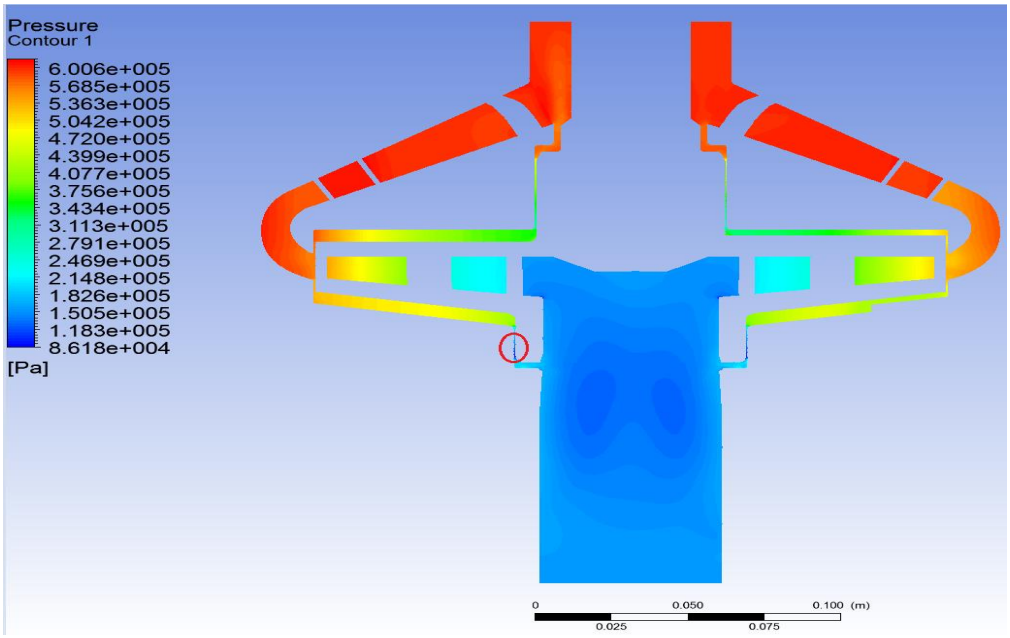

Figure 4-30 Stage 1 pressure distribution and leakage channel local pressure and velocity at 3000 RPM, 100 GPM

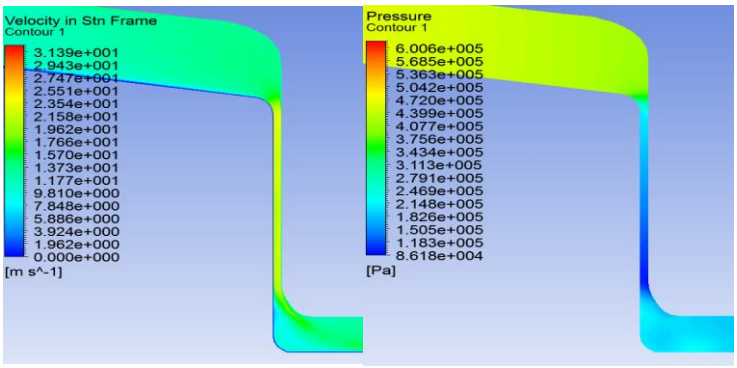

Figure 4-30 Continued

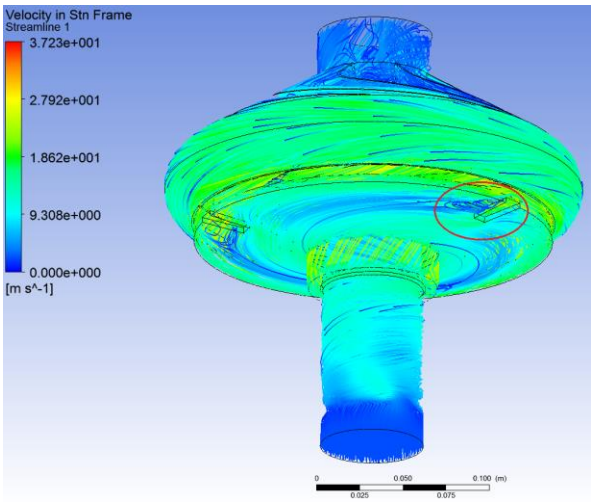

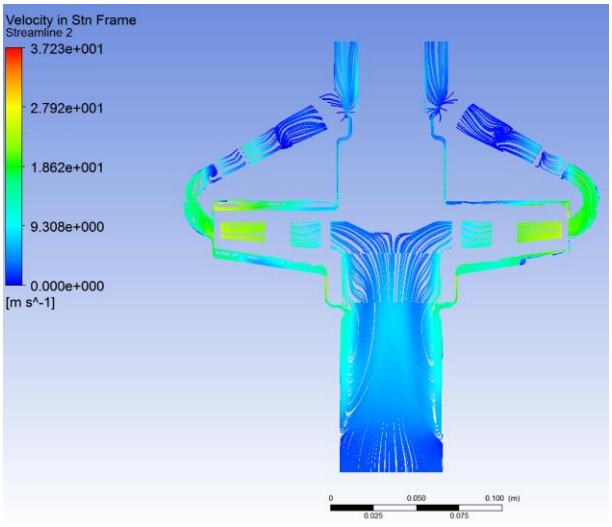

Figure 4-31 Streamline in the flow channel

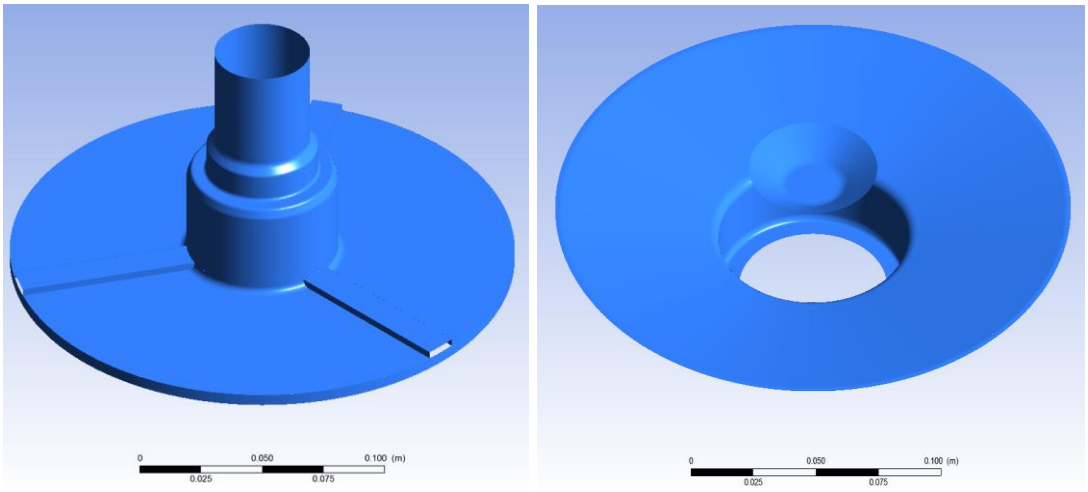

Figure 4-32 Impeller surfaces generating axial thrust

Figure 4-32 shows the surfaces that generate axial thrust in the CFD simulation. The thrust is calculated by integrating the pressure in the Y (gravity) direction. Negative thrust means downward (gravity) direction and positive means upward (anti-gravity) direction.

The axial thrust in nondimensional terms for a fixed flow rate is given as [48]

$$\boldsymbol{f_a} = \frac{\boldsymbol{2F_a}}{\boldsymbol{\rho u_2^2 \pi r_2^2}} \tag{4.3}$$

where f_a is the total axial thrust, u_2 is the impeller outlet tip speed and r_2 is the impeller outlet radius. When the pump runs at different flow rate at the same speed, the following axial thrust coefficient

$$f' = \frac{(\boldsymbol{F - P_1 \pi r_2^2})}{(\boldsymbol{P_2 \pi r_2^2 - P_1 \pi r_2^2})} \tag{4.4}$$

is proposed to include the effect from the inlet and outlet pressure changes. P_1 and P_2 are the inlet and outlet pressure, respectively.

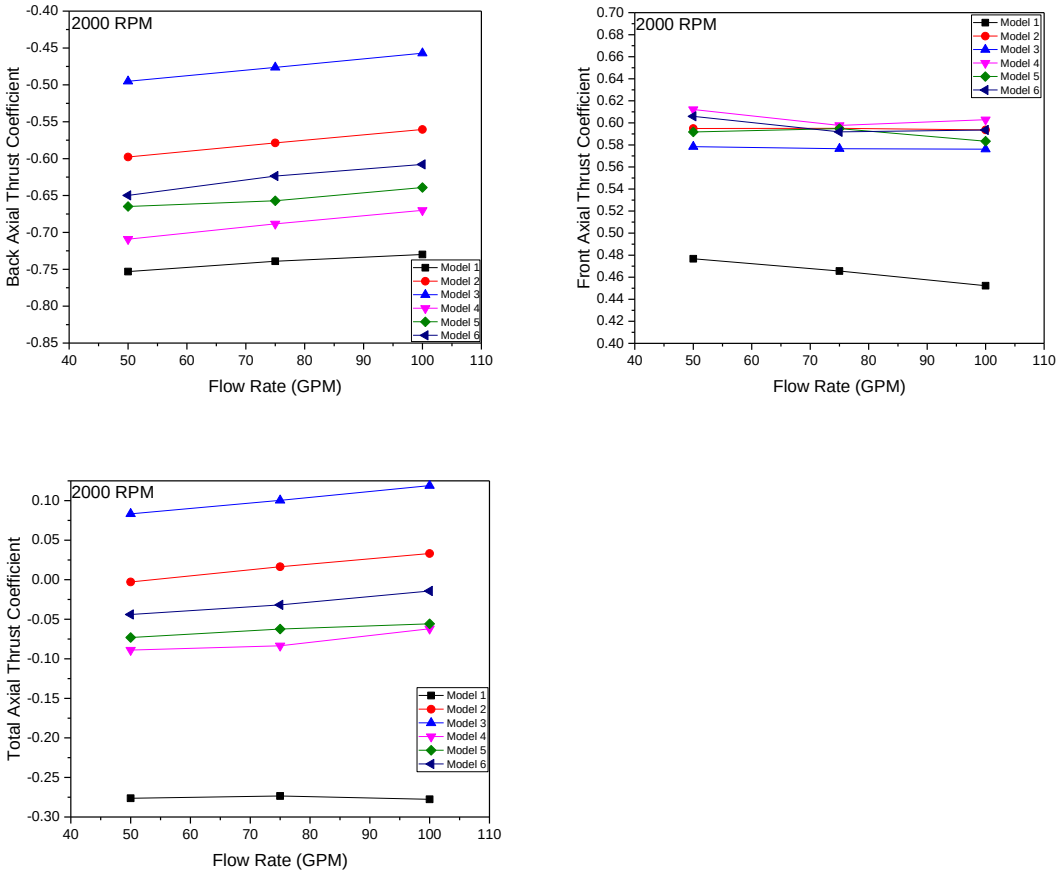

Figure 4-33 Thrust coefficient changes of different models at 2000 RPM

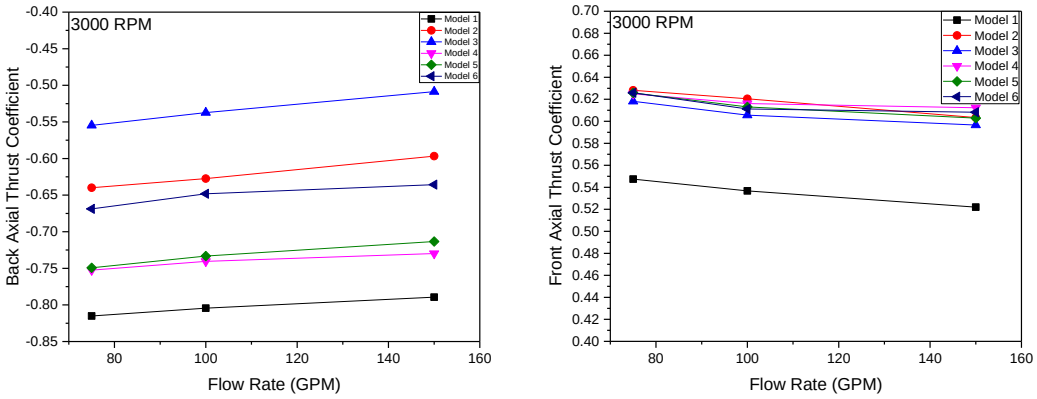

Figure 4-34 Thrust coefficient changes of different models at 3000 RPM

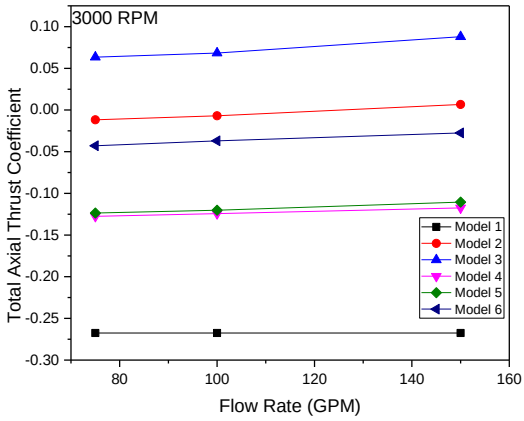

Figure 4-35 continued

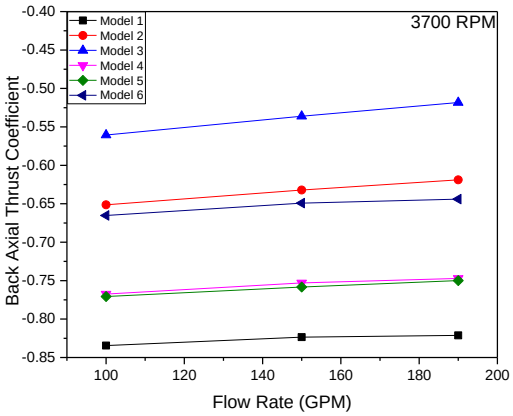

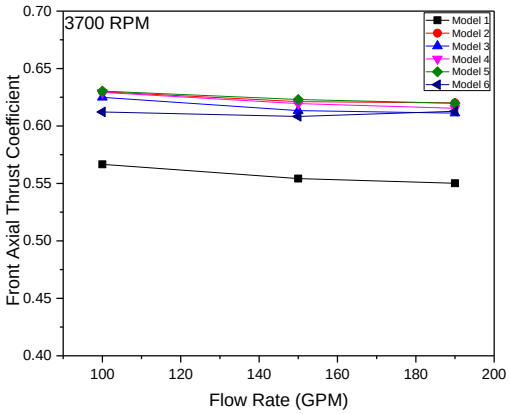

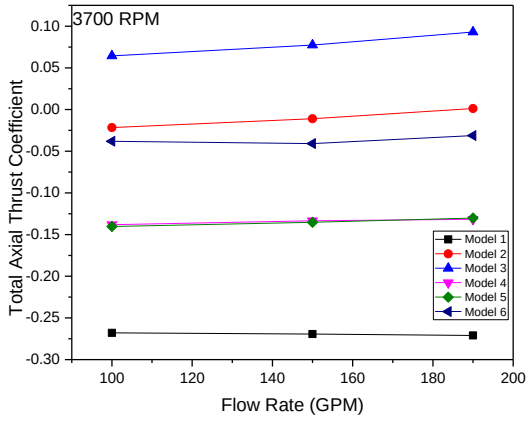

Figure 4-36 Thrust coefficient changes of different models at 3700 RPM

Figure 4-33, Figure 4-35 and Figure 4-36 show the axial thrust coefficient changes of the 6 models at 2000 RPM, 3000 RPM and 3700 RPM, respectively.

Model 1 has no casing ribs and its front thrust is the smallest of all the six models. The remaining five models include casing ribs and the front thrust significantly increases compared with Model 1. For a given speed, the front axial thrust increases as the flow rate increases following the pressure increases in the shroud clearance. For the models with casing ribs, the changes in POVs do not affect the front axial thrust significantly. The front axial thrusts are similar for all five models for the given speed and flow rate.

Model 1 and 3 exhibit the highest and lowest back axial thrust, respectively. Comparing the back axial thrust between the five models leads to the conclusion that axial thrust decreases as POVs size increases (height and length). For a constant speed, the absolute value of back axial thrust decreases with increasing flow rate.

The back axial thrust changes dominate the total thrust changes as the front axial thrust is relatively constant for a fixed speed. For Model 1, 2, 4 and 5, the total thrusts are negative in all the conditions. Model 3 has the largest POVs, and its back thrust absolute value decreases to the extent that the total axial thrust is always positive. Model 2 shows a balanced overall thrust at all the running conditions and displays the smallest absolute value of the total axial thrust compared to the other models at all the working conditions. Thus, the POVs can effectively reduce the axial thrust and provide stable axial thrust control for a wide operating range.

Figure 4-37 shows the pressure contours of Model 2 (left) and Model 1 (right) in the front shroud clearance (a) and in the backface clearance (b). In the front shroud clearance, the casing ribs reduce the flow circumferential velocity and increase the pressure in the clearance. In the backface clearance, the ribs on the impeller work as secondary impeller blades and increase both the circumferential and radial velocity of the flow. The pressure in the backface clearance reduces as the flow velocity increases.

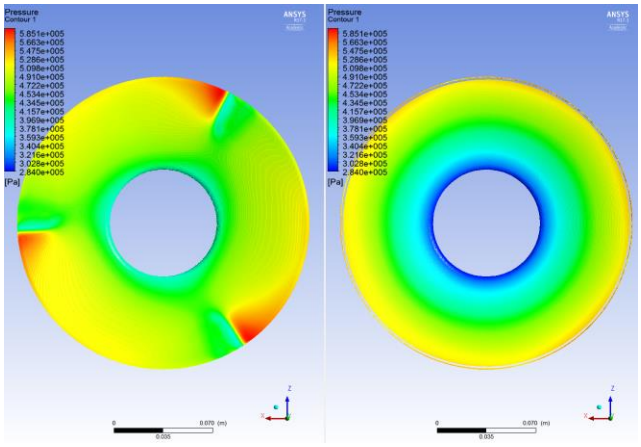

(a)

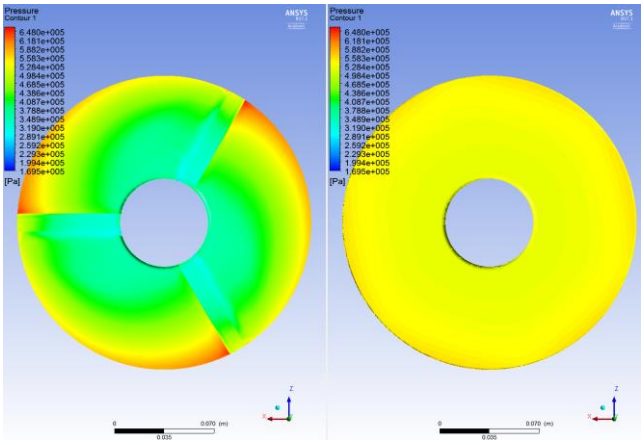

(b)

Figure 4-37 Pressure contour of Model 2 (left) and Model 1 (right) in the front shroud clearance (a) and in the backface clearance (b)

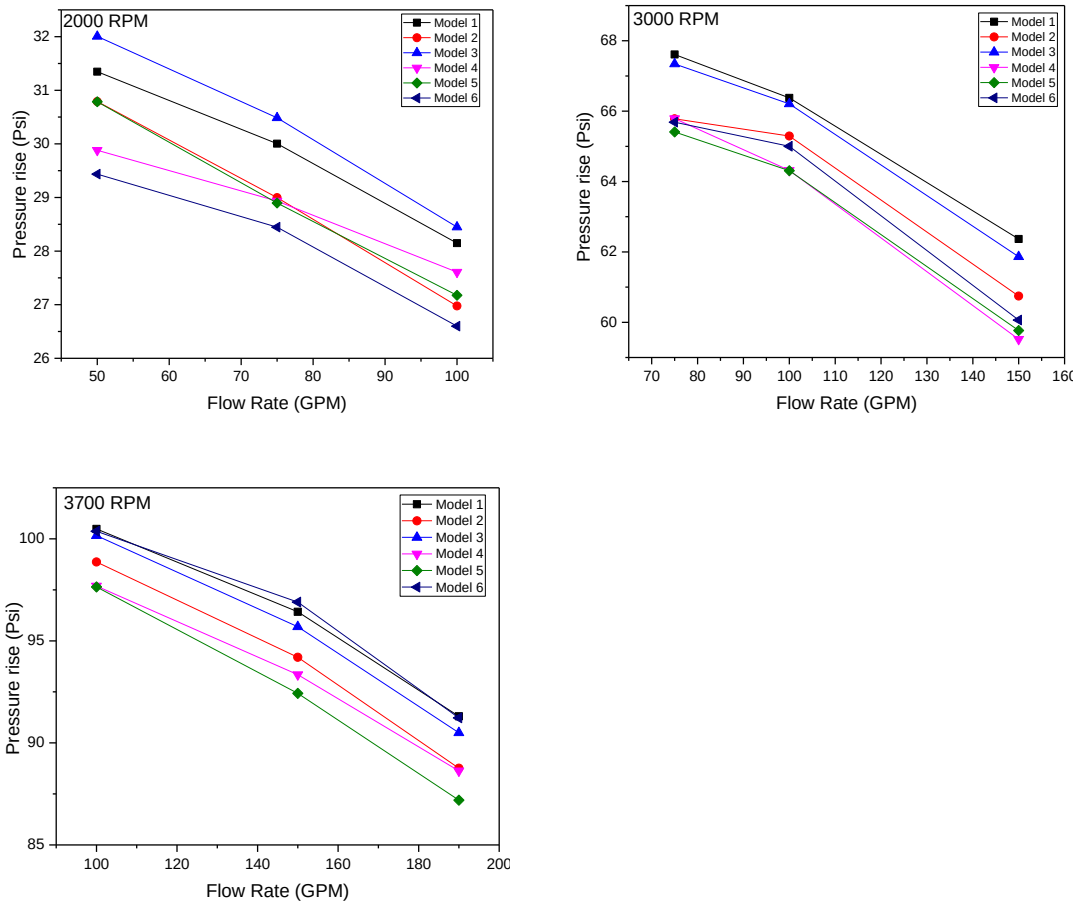

Figure 4-38 Pressure rise of the 6 models at different conditions

Figure 4-38 shows the pressure rise for the six different models at different working conditions. The pressure rise increases with the increasing speed and decreases with increasing flow rate in all the models. The POVs actually work as auxiliary pump vanes installed on the impeller backface pumping liquid from the outlet to main flow channel. While the suction effect of the POVs inrease the inlet zone pressure, its pumping effect tends to increase the outlet zone pressure. The combined effect varies with working conditions.

POVs reduce the overall pump efficiency since they increase the internal leakage flow rate and also generate more turbulence in the backface clearance. POVs pumping effect and power consumption is proportional to their size. Figure 4-39 shows the changes of the efficiencies of the six models at different conditions. The Model 1 always has the highest efficiency at all running speeds and flow rates. The Model 3 with the longest and highest POVs shows the lowest efficiency.

Model 2 has longer but lower POVs compared with Model 6. These have almost the same efficiency at 2000 RPM, but Model 6 shows higher efficiency at 3000 and 3700 RPM. The long POVs generate more pump efficiency loss at high speeds. The comparison of the efficiency between Model 4 and Model 5 yields the same conclusion.

Figure 4-40 shows the power input of the six models at different working conditions. Model 1 with no POVs or casing ribs has the lowest power consumption in all conditions, while Model 3 with the longest and highest POVs has the highest power consumption. Because the power consumption increases with 5th power of the POV outer diameter, the impellers with longer POVs consume much more power at high speed.

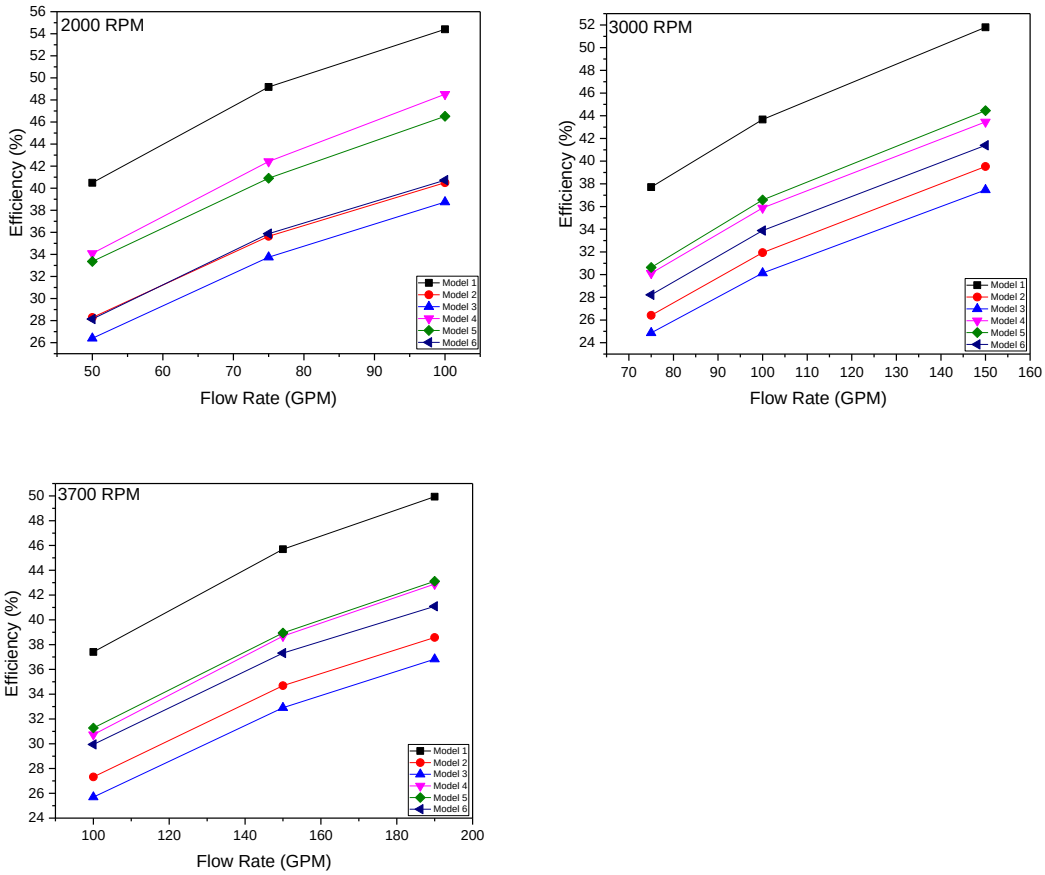

Figure 4-39 Efficiency of the 6 models at different conditions

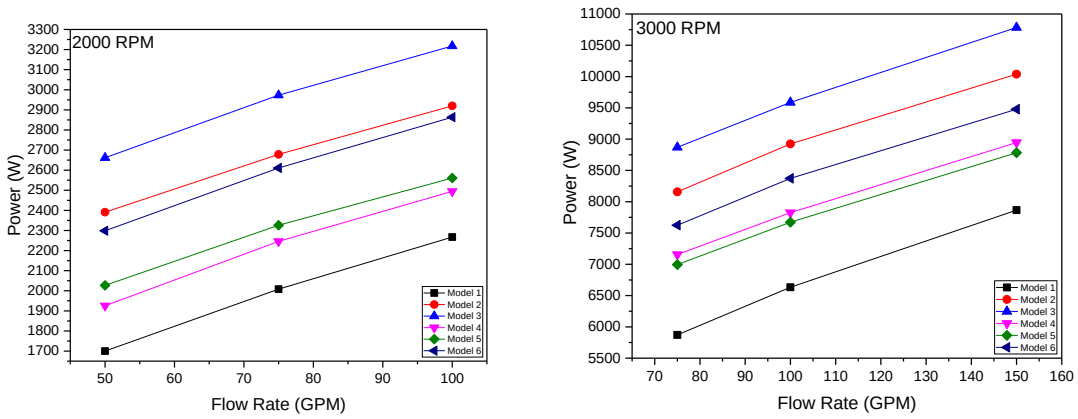

Figure 4-40 Power input of the 6 models at different conditions

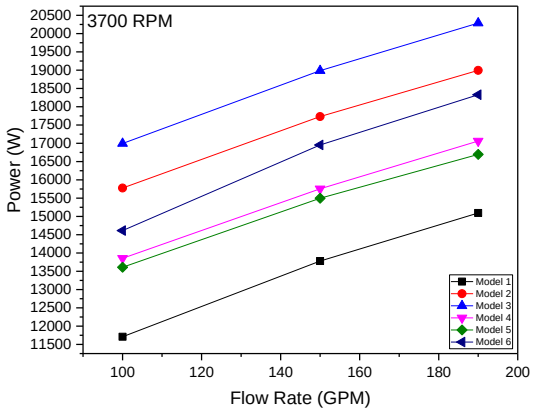

Figure 4-40 Continued

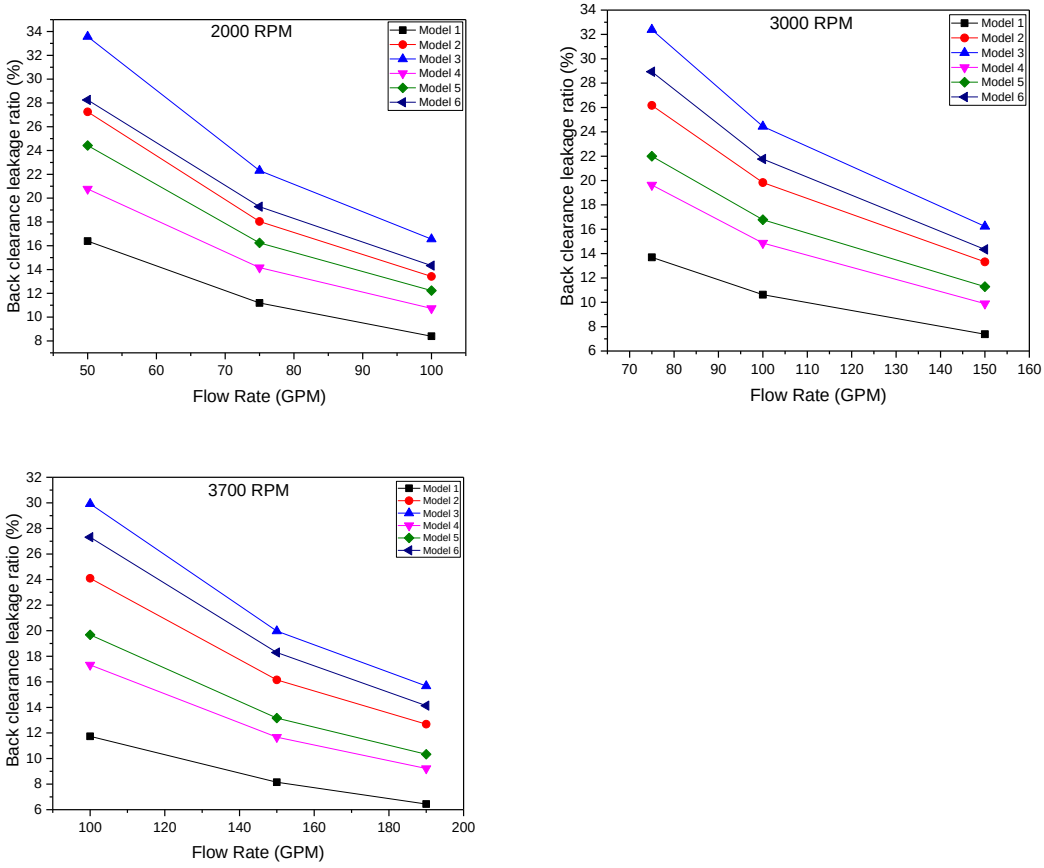

Figure 4-41 Back clearance leakage ratio of the 6 models at different conditions

The leakage flow ratio is the ratio of the leakage flow rate to the inlet flow rate. Figure 4-41 shows the back face clearance leakage flow ratio for the six models at different conditions. Because there is no POV pumping effect in Model 1, it has the lowest back clearance leakage. Model 3 has the highest leakage flow due to the predominant POV pumping effect.

The results indicate that POVs are very effective for axial thrust control at the cost of increased power consumption and reduced efficiency. The POVs can provide stable axial thrust control over a wide working range. To lower the efficiency loss from the POVs, short but high POVs are recommended for high-speed conditions. If the length of the POVs in Model 6 was increased, Model 6 could potential reach similar axial thrust performance as Model 1 with higher efficiency.

5. CONCLUSIONS AND RECOMMENDATIONS

This study details the numerical and experimental investigation of a Canned-Motor-Pump performance operating in single- and two-phase flow conditions.

In experimental test, the CMP worked as predicted with all the parameters within designed limits in both single-phase flow test and the two-phase flow test. The CMP motor temperature were below the limit by a significant margin of 118 ^{o}F. The axial thrust was within the limit value 1000 lbf and it is mainly affected by the pressure distribution within the impeller shroud and backface clearance. The efficiency of the test pump is lower than the normal centrifugal pump due to the original design purpose. It was found that the pump input power and pump inlet flow temperature dominate the motor temperature while the recirculation flow rate and flow properties have minimal effects on the motor temperature.

The CFD study of the recirculation flow channel reveals that the motor stator wall temperature is dominated by the recirculation flow rate. When the GVF changes from 0 to 20%, the maximum peak temperature increase is 16.1 ^{o}F. The CFD results show that the recirculation channel geometry can be optimized to enhance the heat convection and reduce the local wall temperature. The 2D analysis of the motor temperature profile variation reveals that the motor temperature will still be within design limits if the recirculation flow rate decreases by 50%.

The CFD study of the POVs systematically evaluated the effect of POVs on both the pump axial thrust control and the pump overall performance. Long POVs can significantly reduce the pump efficiency and thus shorter but taller POVs are preferred.

The current POVs show good control of the axial thrust but these can be optimized by reducing the length and increasing the height. The study reveals that the POVs can strongly increase the pump power consumption and lower the pump efficiency.

Some suggestions for the current Canned Motor Pump design:

1. The recirculation flow rate can be reduced to improve pump efficiency.
2. The recirculation channel flow channel can be easily modified by optimizing the cavities to improve the flow field and reduce local high wall temperatures.
3. The pump efficiency will improve if implementing shorter but taller POVs.

Future work can be addressed:

1. The casing ribs alone without POVs has the potential to balance the axial thrust with less efficiency loss
2. Whether the centrifugal pump inlet pre-rotation and pre-swirling has positive or negative effect on pump efficiency and how the front shroud leakage flow affects the pre-rotation.

REFERENCES

1. Feldle, G. and Kempf J. *Canned Motor Pumps for the Conveying of Liquefied Gases Gases-Alternative for High Pressure*. Process Worldwide. 2012.

2. Grötsch, J., J.H. Timcke, and C. Winkelmuller, *Inside the canned motor centrifugal pump.* World Pumps, 1999. 1999(396): p. 58-61.

3. Scott, C., *Considerations for a canned motor pump.* World pumps, 2004. 2004(459): p. 22-25.

4. Guardiani, R.F., F.M. Hauck, and S.D. Riesenweber. *Nuclear Waste Transfer Pump-Design, Analysis, Testing, AND Operation*. in *PROCEEDINGS OF THE INTERNATIONAL PUMP USERS SYMPOSIUM*. 2001.

5. Jindal, V., *Canned Motor Pump Failure: A Case History of Canned Motor Pump Failures - Demystifying the Thrust force*. 2011.

6. Bruckner, R.J. and R.A. Manco, *ISS Ammonia Pump Failure, Recovery, and Lesson Learned A Hydrodynamic Bearing Perspective.* 2014.

7. Fairman, K., An *Integral Balance Piston For Centrifugal Pump Pump Impellers.* in Turbomachinery and Pump Symposia. 1991

8. Gülich, J.F., *Centrifugal pumps*. 2008.

9. Guelich, J. *Axial thrust*. 2017 cited 2017; Available from: https://www.ksb.com/centrifugal-pump-lexicon/axial-thrust/191862/.

10. Nelson, W.E., *Maintenance and troubleshooting of single-stage centrifugal pumps*, in *Processing of the first international pump symposium*. 1984. p. 174-84.

11. Girdhar, P. and O. Moniz, *Practical centrifugal pumps*. 2011.

12. Paresh, G. and O. Moniz, *Practical Centrifugal Pumps: Design, Operation and Maintenance*. 2005.

13. Venkataraman, B., et al. *Fundamentals of a motor thermal model and its applications in motor protection*. in *Protective Relay Engineers, 2005 58th Annual Conference for*. 2005.

14. Brancato, E.L., *Estimation of lifetime expectancies of motors.* IEEE Electrical Insulation Magazine, 1992. 8(3): p. 5-13.

15. Cezário, C.A., et al. *Transient thermal analysis of an induction electric motor*. in *18th International Congress of Mechanical Engineering*. 2005.

16. Saari, J., *Thermal analysis of high-speed induction machines*. Helsinki University of Technology. 1998.

17. Reynolds, W.C., R. Lundberg, and P. McCuen, *Heat transfer in annular passages. General formulation of the problem for arbitrarily prescribed wall temperatures or heat fluxes.* International Journal of Heat and Mass Transfer, 1963. 6(6): p. 483-493.

18. Lundberg, R., P. McCuen, and W.C. Reynolds, *Heat transfer in annular passages. Hydrodynamically developed laminar flow with arbitrarily prescribed wall temperatures or heat fluxes.* International Journal of Heat and Mass Transfer, 1963. 6(6): p. 495-529.

19. Lundberg, R.E., W.C. Reynolds, and W.M. Kays, *Heat transfer with laminar flow in concentric annuli with constant and variable wall temperature with [ie and] heat flux*. National Aeronautics and Space Administration. 1961.

20. Childs, P. and C. Long, *A review of forced convective heat transfer in stationary and rotating annuli.* Proceedings of the Institution of Mechanical Engineers, Part C: Journal of Mechanical Engineering Science, 1996. 210(2): p. 123-134.

21. Yan Wood, E., *Heat transfer with turbulent flow in concentric and eccentric annuli with constant and variable heat flux.* 1962.

22. Kays, W. and E. Leung, *Heat transfer in annular passages—hydrodynamically developed turbulent flow with arbitrarily prescribed heat flux.* International Journal of Heat and Mass Transfer, 1963. 6(7): p. 537-557.

23. Davis, E.S., *Heat transfer and pressure drop in annuli.* Trans. Asme, 1943. 65: p. 755.

24. Foust, A. and G. Christian, *Non-boiling heat transfer coefficients in annuli.* Am. Inst. Chem. Eng, 1940. 36(4): p. 541-554.

25. Monrad, C. and J. Pelton, *Heat transfer by convection in annular spaces.* Trans. AIChE, 1942. 38(593): p. 123.

26. McMillan, E. and R. Larson, *Annular heat transfer coefficients for turbulent flow.* Trans Am Inst Chem Eng, 1946. 41: p. 177-25.

27. Stein, R.P. and W. Begell, *Heat transfer to water in turbulent flow in internally heated annuli.* AIChE Journal, 1958. 4(2): p. 127-131.

28. Dirker, J. and J. Meyer, *Convective heat transfer coefficients in concentric annuli.* Heat Transfer Engineering, 2005. 26(2): p. 38-44.

29. McAdams, W.H., *Heat Transimissons, 3rd ed*. 1954.

30. Dittus, F. and L. Boelter, *University of California publications on engineering.* University of California publications in Engineering, 1930. 2: p. 443.

31. McMillen, E.L. and R.E. Larson, *Annular heat transfer coefficients for turbulent flow.* Trans. Am. Inst. Chem. Engrs, 1944. 40: p. 177-202.

32. Briggs, D. and E.H. Young. *Modified Wilson plot techniques for obtaining heat transfer correlations for shell and tube heat exchangers*. in *Chemical Engineering Progress Symposium Series*. 1969.

33. Puchkov, P. and O. Vinogradov. *Heat transfer and hydraulic resistance in annular channels with smooth and rough heat transfer surfaces*. in *Heat and Mass Transfer*. 1967.

34. Fénot, M., et al., *A review of heat transfer between concentric rotating cylinders with or without axial flow.* International journal of thermal sciences, 2011. 50(7): p. 1138-1155.

35. Becker, K.M. and J. Kaye, *Measurement of diabatic flow in an annulus with an inner rotating cylinder*. MIT Research Laboratory of Heat Transfer in Electronics. 1960.

36. Wang, H., *Experimental and numerical study of Taylor-Couette flow.* 2015.

37. Tachibana, F., S. FUKUI, and H. MITSUMURA, *Heat transfer in an annulus with an inner rotating cylinder.* Bulletin of JSME, 1960. 3(9): p. 119-123.

38. Tachibana, F. and S. Fukui, *Convective heat transfer of the rotational and axial flow between two concentric cylinders.* Bulletin of JSME, 1964. 7(26): p. 385-391.

39. Ho, C.Y., J. Nardacci, and A. Nissan, *Heat transfer characteristics of fluids moving in a Taylor system of vortices. Part II. NPr≠I.* AIChE Journal, 1964. 10(2): p. 197-202.

40. Kaye, J. and E.C. Elgar, *Modes of adiabatic and diabatic fluid flow in an annulus with an inner rotating cylinder*. MIT Research Laboratory of Heat Transfer in Electronics. 1957.

41. Shiomi, Y., et al., *Two-phase flow in an annulus with a rotating inner cylinder (flow pattern in bubbly flow region).* Nuclear engineering and design, 1993. 141(1-2): p. 27-34.

42. Shiomi, Y., S. Nakanishi, and H. Kutsuna, *CFD calculation for two-phase flow in concentric annulus with rotating inner cylinder.* Phoenics Journal of Computational Fluid Dynamics and its Applications, 2000. 13(1): p. 029-040.

43. Majji, M.V., J. Morris, and S. Banerjee, *Flow Transition OF Neutrally Buoyant Suspension Between Concentri Cylinders.* ICTAM. 2016

44. Jakoby, R., S. Kim, and S. Wittig, *Correlations of the convective heat transfer in annular channels with rotating inner cylinder.* ASME paper, 1998(98-GT): p. 97.

45. energy, U.d.o. *Premium efficiency motor selection and application guide*. 2017; https://energy.gov/sites/prod/files/2014/04/f15/amo_motors_handbook_web.pdf.

46. Breugelmans, F. and M. Sen. *Prerotation and fluid recirculation in the suction pipe of centrifugal pumps*. in *Proc. 11th Int. Pump Symp., Texas A&M Univ*. 1982.

APPENDIX

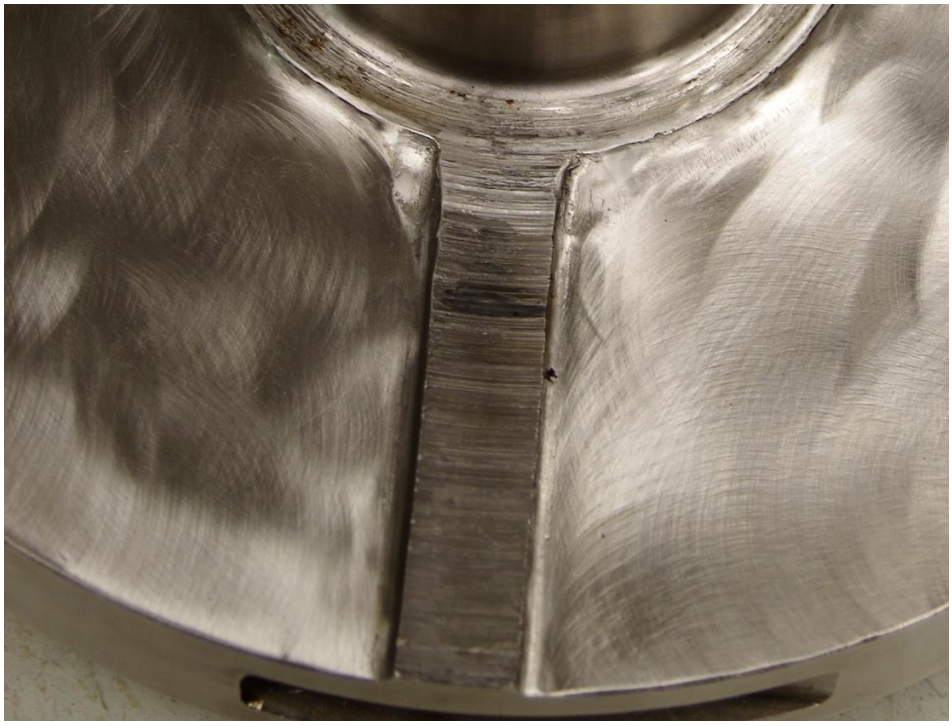

Rubbings on pump casing and impeller POV surfaces because of the shaft movement from uncontrolled axial thrust

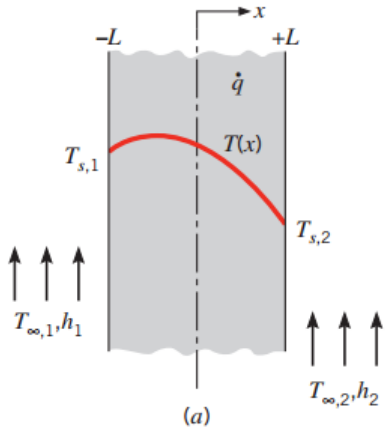

$$T(x) = \frac{\dot{q}L^2}{2k}\left(1 - \frac{x^2}{L^2}\right) + \frac{T_{s,2} - T_{s,1}}{2}\frac{x}{L} + \frac{T_{s,1} + T_{s,2}}{2}$$

$$T'(x) - T(x) = [(T's, 2 - Ts, 2) - (T's, 1 - Ts, 1)]\frac{x}{2L}$$

$$+ \frac{(T's, 1 + T's, 2) - (Ts, 1 + Ts, 2)}{2}$$

1D plane wall heat transfer with internal uniform heat generation. When x=L, the temperature difference is maximum

The thrust cavity and hub plate pressure change with the GVFs and the flow rates. They help to evaluate the effect of stator jacket air injection on the thrust cavity. The following figures show the thrust cavity and hub plate relative pressure change at different flow rates and GVFs.

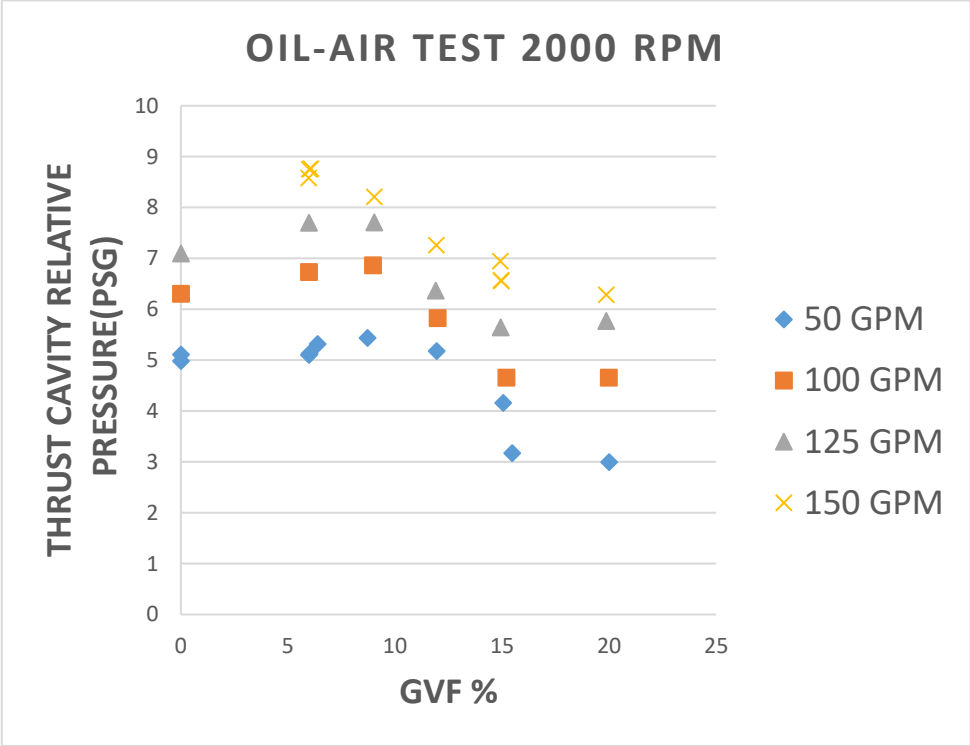

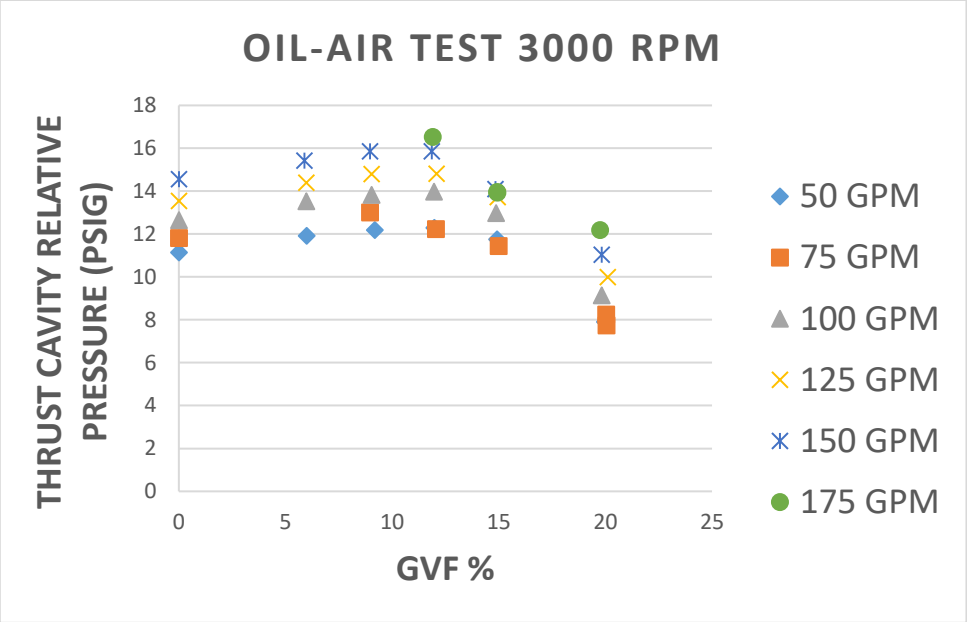
OIL-AIR TEST 3000 RPM
THRUST CAVITY RELATIVE PRESSURE (PSIG)
18
16
14
12
10
8
6
4
2
0
0
5
10
15
20
25
GVF %
50 GPM
75 GPM
100 GPM
125 GPM
150 GPM
175 GPM

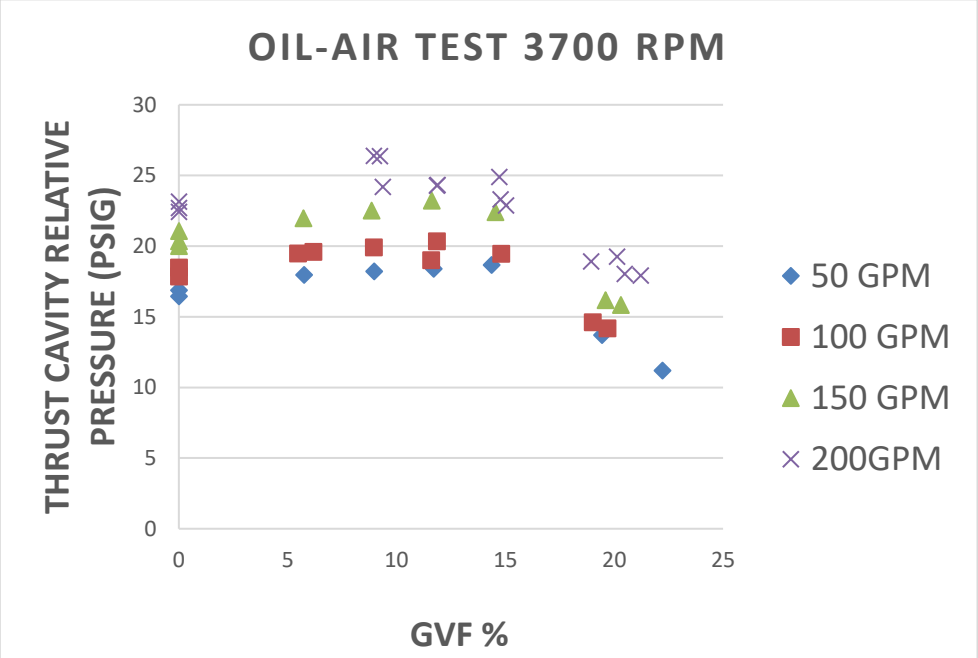
OIL-AIR TEST 3700 RPM
THRUST CAVITY RELATIVE PRESSURE (PSIG)
30
25
20
15
10
5
0
0
5
10
15
20
25
GVF %
50 GPM
100 GPM
150 GPM
200GPM

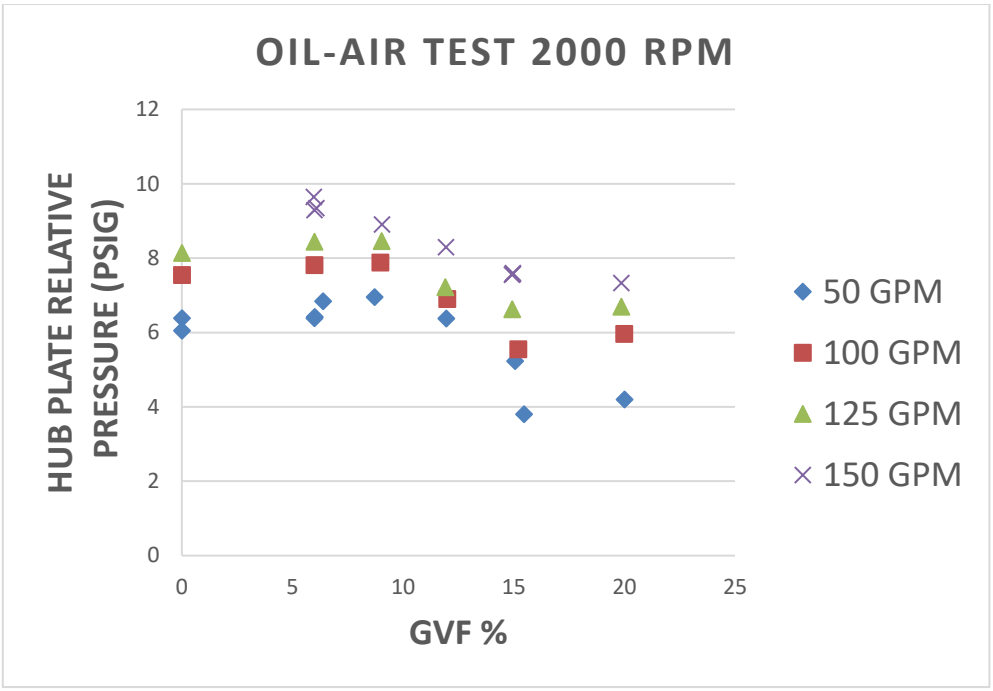
OIL-AIR TEST 2000 RPM
HUB PLATE RELATIVE PRESSURE (PSIG)
12
10
8
6
4
2
0
0
5
10
15
20
25
GVF %
50 GPM
100 GPM
125 GPM
150 GPM

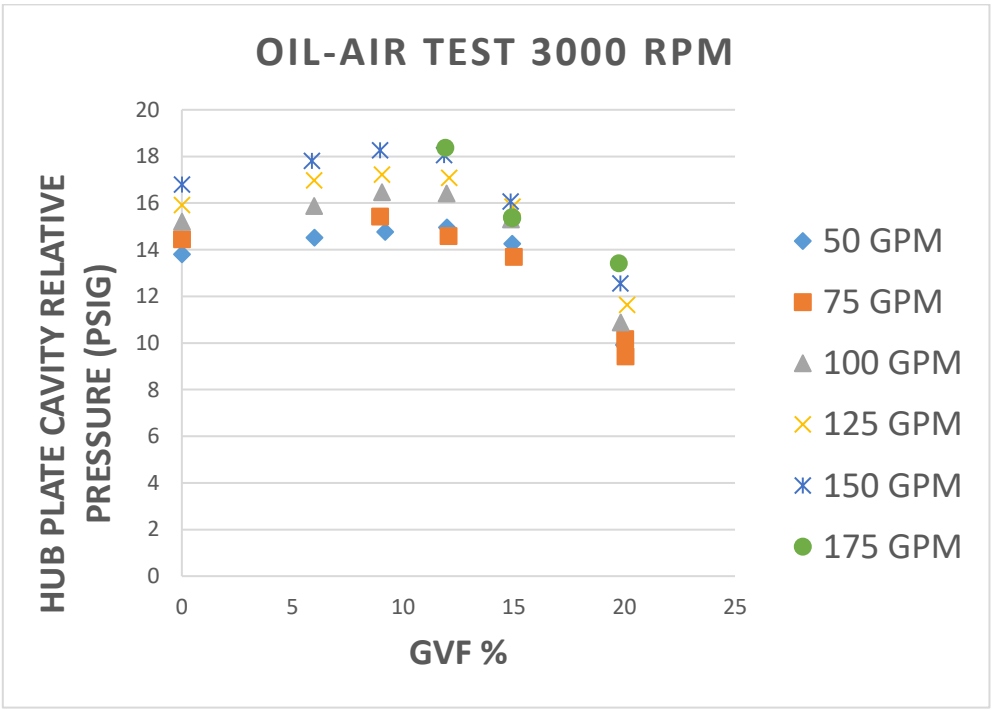
OIL-AIR TEST 3000 RPM
HUB PLATE CAVITY RELATIVE PRESSURE (PSIG)
20
18
16
14
12
10
8
6
4
2
0
0
5
10
15
20
25
GVF %
50 GPM
75 GPM
100 GPM
125 GPM
150 GPM
175 GPM

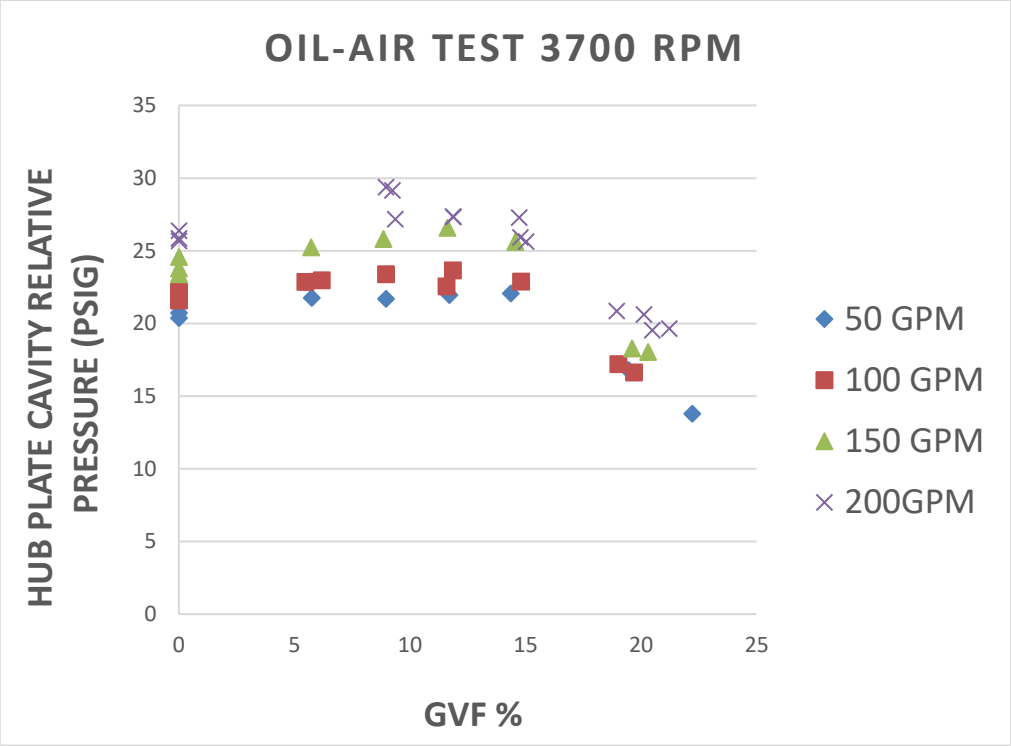
OIL-AIR TEST 3700 RPM
HUB PLATE CAVITY RELATIVE PRESSURE (PSIG)
35
30
25
20
15
10
5
0
0
5
10
15
20
25
GVF %
50 GPM
100 GPM
150 GPM
200GPM

Operating the pump at elevated vibration can lead to components damage and the maximum overall unfiltered vibrations are mostly within the pump operating limit. To monitor the vibration of the pump, two 3-aixes accelerometers were installed at the top and bottom of the pump casing. The following figures show the processed vibration data.

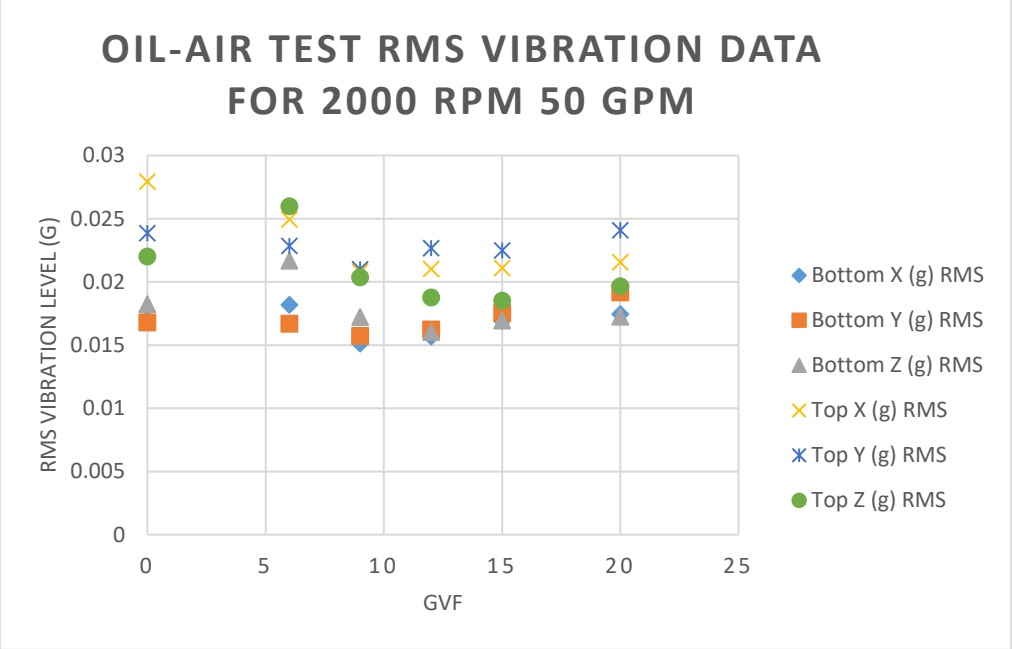

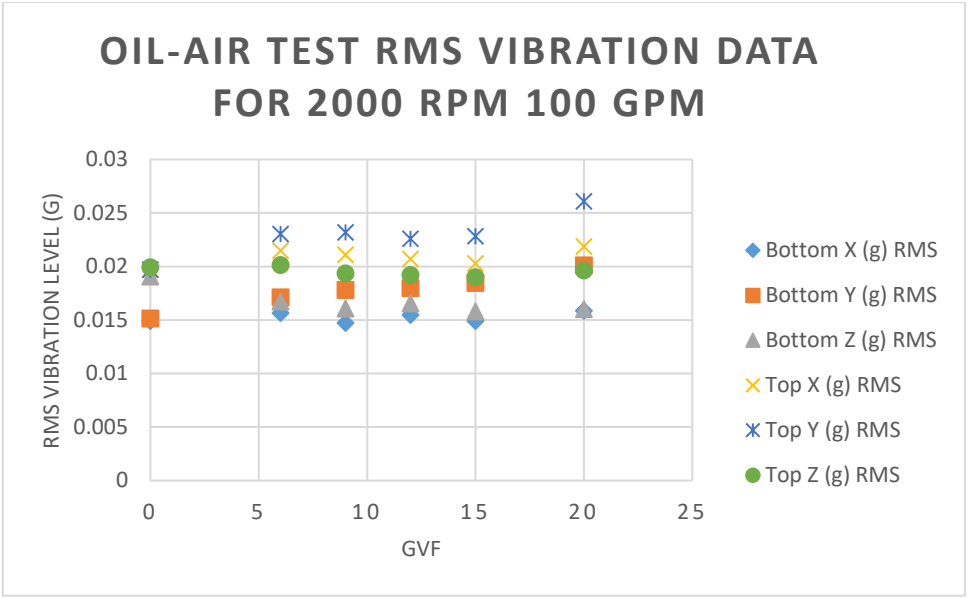
OIL-AIR TEST RMS VIBRATION DATA FOR 2000 RPM 100 GPM
RMS VIBRATION LEVEL (G)
0.03
0.025
0.02
0.015
0.01
0.005
0
0
5
10
15
20
25
GVF
Bottom X (g) RMS
Bottom Y (g) RMS
Bottom Z (g) RMS
Top X (g) RMS
Top Y (g) RMS
Top Z (g) RMS

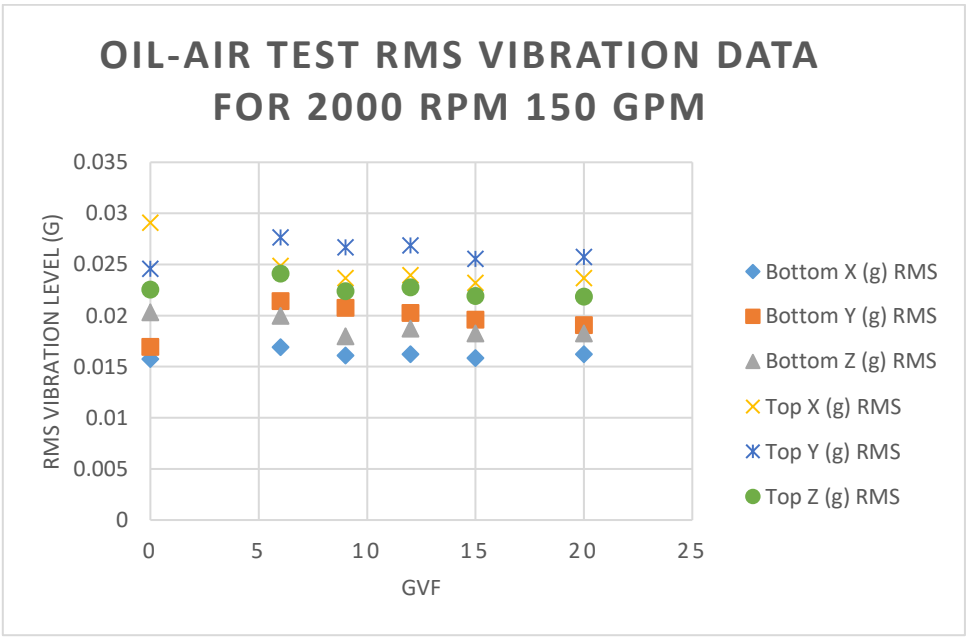
OIL-AIR TEST RMS VIBRATION DATA FOR 2000 RPM 150 GPM
RMS VIBRATION LEVEL (G)
0.035
0.03
0.025
0.02
0.015
0.01
0.005
0
0
5
10
15
20
25
GVF
Bottom X (g) RMS
Bottom Y (g) RMS
Bottom Z (g) RMS
Top X (g) RMS
Top Y (g) RMS
Top Z (g) RMS

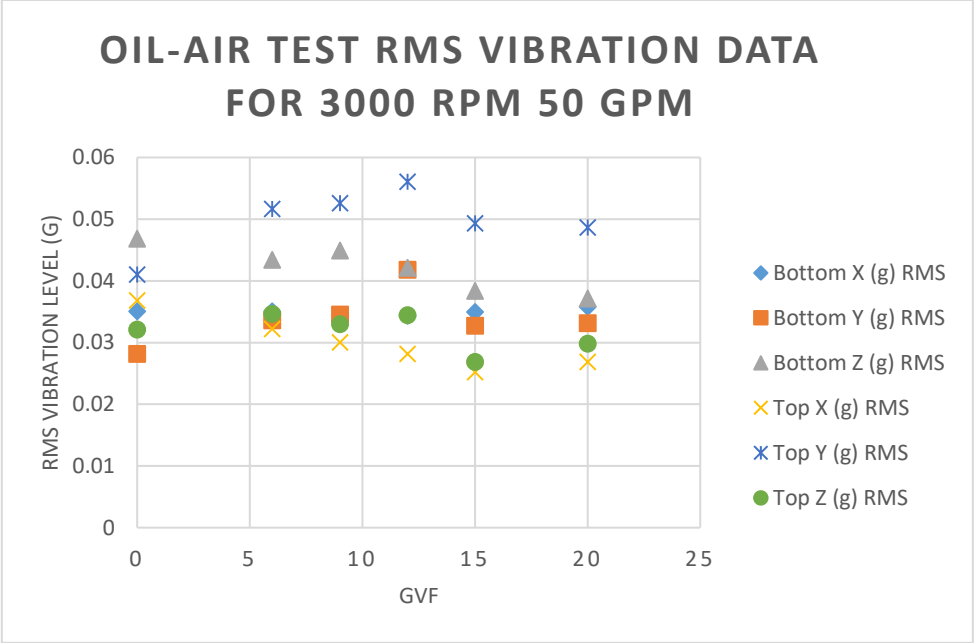
OIL-AIR TEST RMS VIBRATION DATA FOR 3000 RPM 50 GPM
RMS VIBRATION LEVEL (G)
0.06
0.05
0.04
0.03
0.02
0.01
0
0
5
10
15
20
25
GVF
Bottom X (g) RMS
Bottom Y (g) RMS
Bottom Z (g) RMS
Top X (g) RMS
Top Y (g) RMS
Top Z (g) RMS

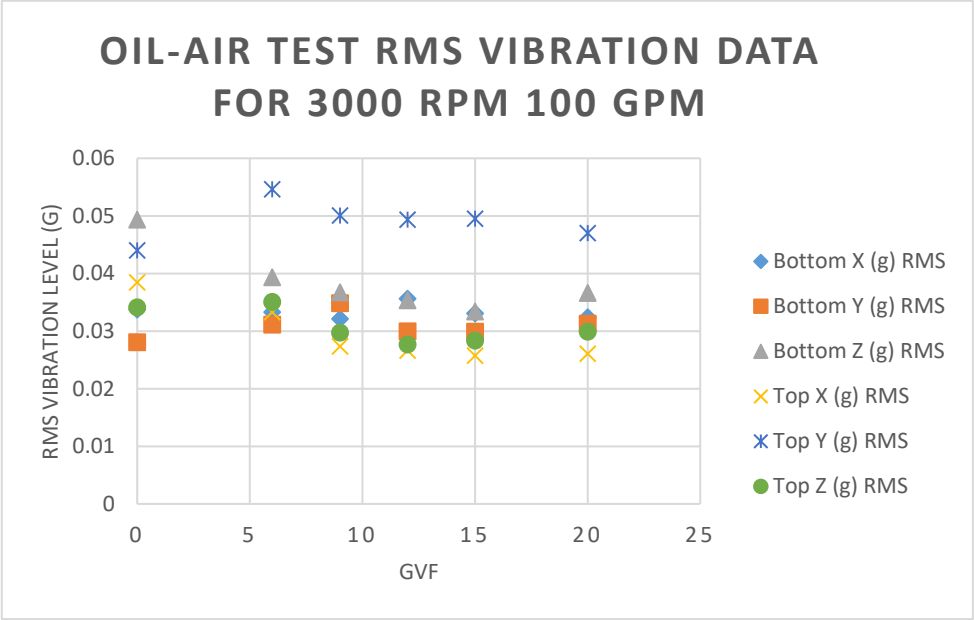
OIL-AIR TEST RMS VIBRATION DATA FOR 3000 RPM 100 GPM
RMS VIBRATION LEVEL (G)
0.06
0.05
0.04
0.03
0.02
0.01
0
0
5
10
15
20
25
GVF
Bottom X (g) RMS
Bottom Y (g) RMS
Bottom Z (g) RMS
Top X (g) RMS
Top Y (g) RMS
Top Z (g) RMS

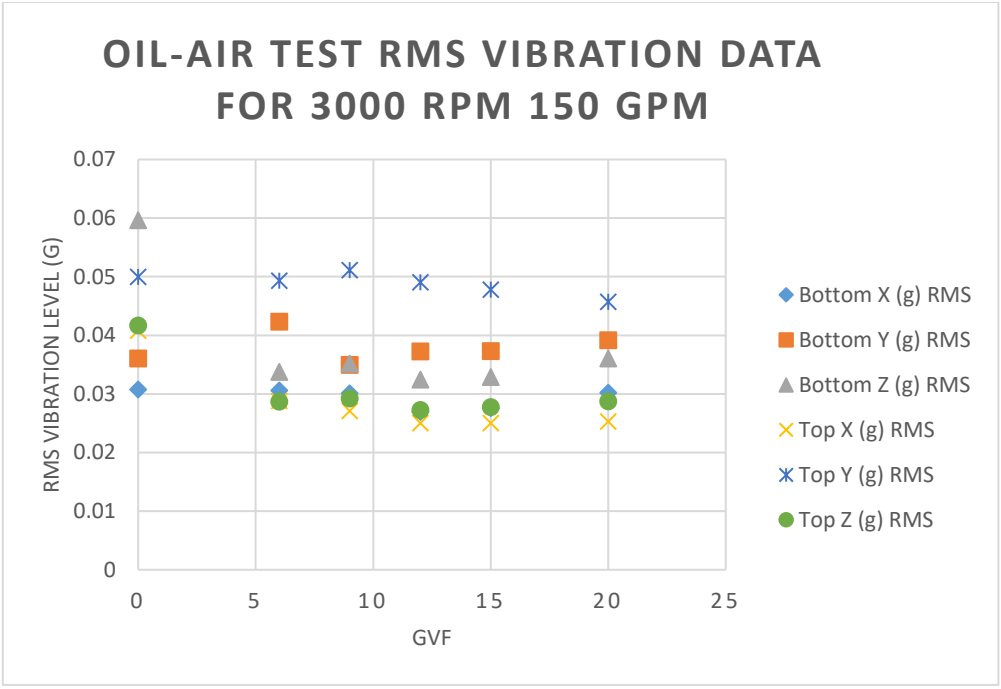
OIL-AIR TEST RMS VIBRATION DATA FOR 3000 RPM 150 GPM
RMS VIBRATION LEVEL (G)
0.07
0.06
0.05
0.04
0.03
0.02
0.01
0
0
5
10
15
20
25
GVF
Bottom X (g) RMS
Bottom Y (g) RMS
Bottom Z (g) RMS
Top X (g) RMS
Top Y (g) RMS
Top Z (g) RMS

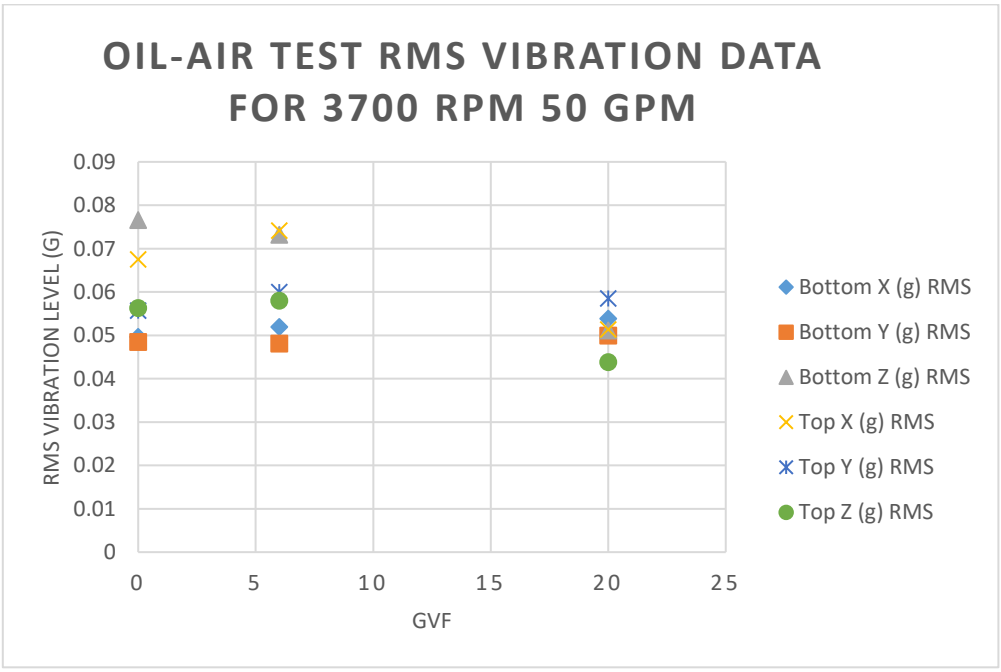
OIL-AIR TEST RMS VIBRATION DATA FOR 3700 RPM 50 GPM
RMS VIBRATION LEVEL (G)
0.09
0.08
0.07
0.06
0.05
0.04
0.03
0.02
0.01
0
0
5
10
15
20
25
GVF
Bottom X (g) RMS
Bottom Y (g) RMS
Bottom Z (g) RMS
Top X (g) RMS
Top Y (g) RMS
Top Z (g) RMS

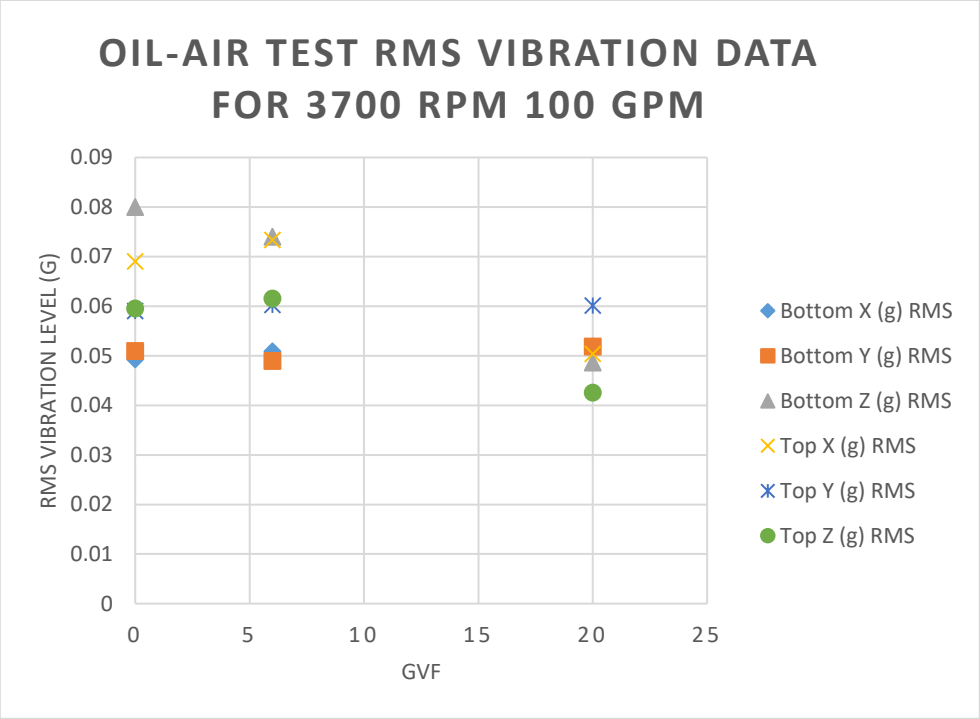
OIL-AIR TEST RMS VIBRATION DATA FOR 3700 RPM 100 GPM
RMS VIBRATION LEVEL (G)
0.09
0.08
0.07
0.06
0.05
0.04
0.03
0.02
0.01
0
0
5
10
15
20
25
GVF
Bottom X (g) RMS
Bottom Y (g) RMS
Bottom Z (g) RMS
Top X (g) RMS
Top Y (g) RMS
Top Z (g) RMS

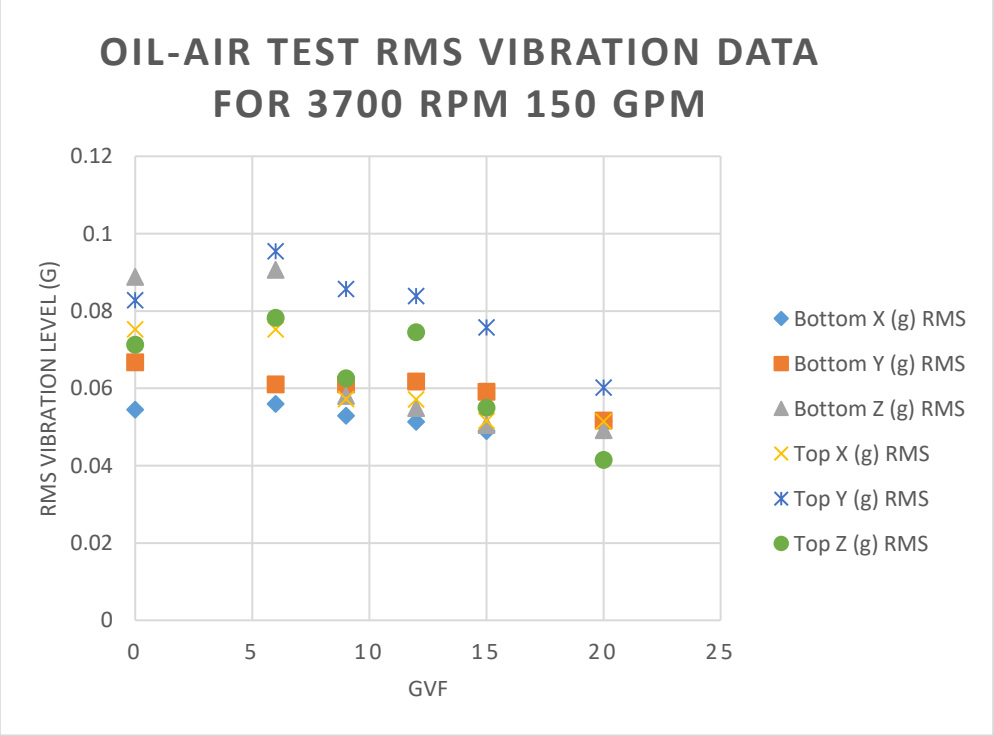
OIL-AIR TEST RMS VIBRATION DATA FOR 3700 RPM 150 GPM
RMS VIBRATION LEVEL (G)
0.12
0.1
0.08
0.06
0.04
0.02
0
0
5
10
15
20
25
GVF
Bottom X (g) RMS
Bottom Y (g) RMS
Bottom Z (g) RMS
Top X (g) RMS
Top Y (g) RMS
Top Z (g) RMS

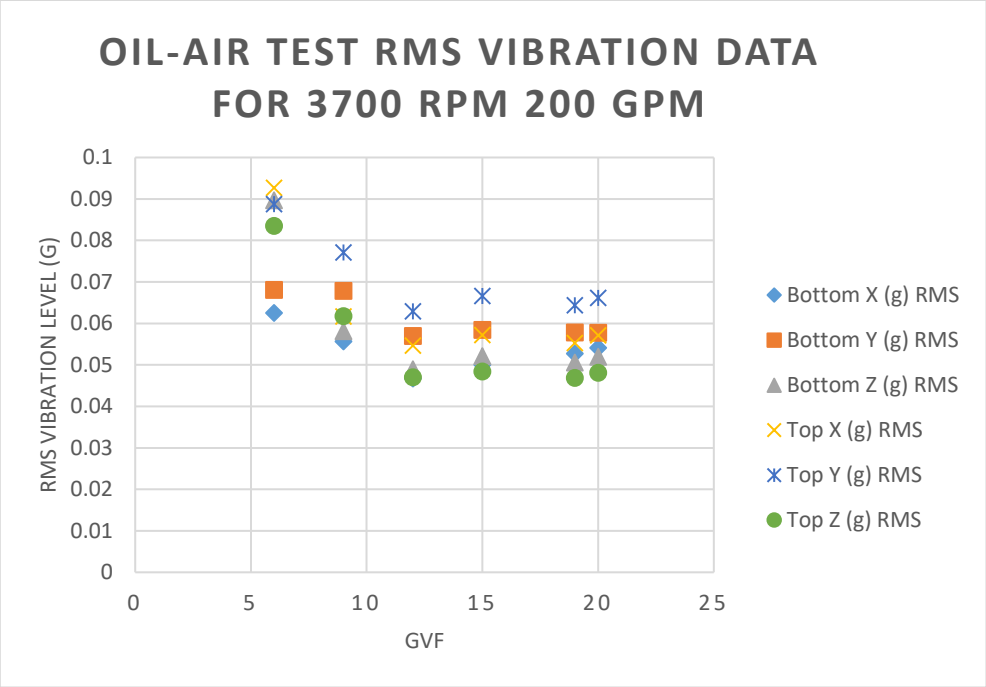
OIL-AIR TEST RMS VIBRATION DATA FOR 3700 RPM 200 GPM
RMS VIBRATION LEVEL (G)
0.1
0.09
0.08
0.07
0.06
0.05
0.04
0.03
0.02
0.01
0
0
5
10
15
20
25
GVF
Bottom X (g) RMS
Bottom Y (g) RMS
Bottom Z (g) RMS
Top X (g) RMS
Top Y (g) RMS
Top Z (g) RMS

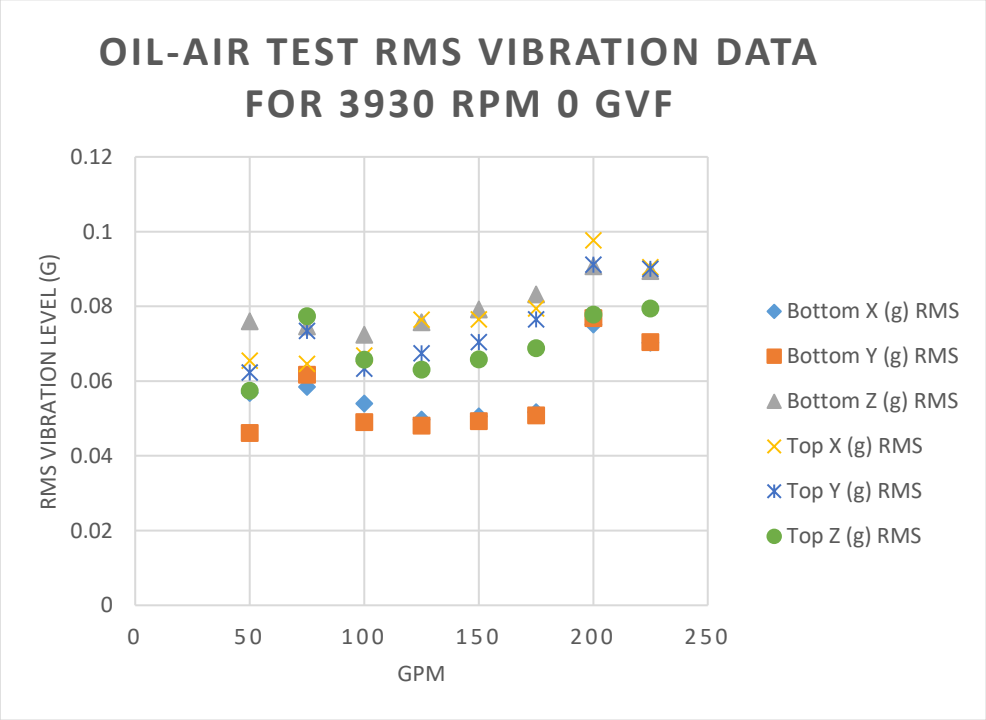
OIL-AIR TEST RMS VIBRATION DATA FOR 3930 RPM 0 GVF
RMS VIBRATION LEVEL (G)
0.12
0.1
0.08
0.06
0.04
0.02
0
0
50
100
150
200
250
GPM
Bottom X (g) RMS
Bottom Y (g) RMS
Bottom Z (g) RMS
Top X (g) RMS
Top Y (g) RMS
Top Z (g) RMS